8-10-2021

Single-Crystalline Graphene by Low-Pressure CVD Method: Nucleation Limited Growth, Transfer, and Characterization

Sajith Madushan Wijayarathna Withanage
Georgia State University

Single-Crystalline Graphene by Low-Pressure CVD Method: Nucleation Limited Growth, Transfer, and Characterization

by

Sajith Madushan Wijayarathna Withanage

Under the Direction of Ramesh Mani, PhD

A Dissertation Submitted in Partial Fulfillment of the Requirements for the Degree of

Doctor of Philosophy

in the College of Arts and Sciences

Georgia State University

2021

ABSTRACT

Graphene has attracted enormous attention due to its unique characteristics. However, the LPCVD graphene grown on copper turns out to be polycrystalline because of the high nucleation density (ND) on the copper foil surface. In order to realize better quality LPCVD graphene, this ND needs to be significantly reduced. Based on the observations from our initial graphene growths on as-received copper, we figured that the uneven Cu surfaces with defects produce large NDs. At a large ND, the graphene flakes nucleated at different sites coalesced to produce polycrystalline graphene. Due to such issues, we have implemented an electropolishing technique to smoothen the native surface of the copper foil. We will discuss the successful implementation of the surface smoothening process to reduce nucleation site formation while limiting the surface defects (which leads to wrinkle formation). The annealing process was also helpful to flatten the surface during the growth process further. We have also observed that graphene grows across Cu grain boundaries and, in the process, produces an additional surface area for graphene growth. That later causes to form wrinkles, which affect graphene properties negatively.

In the next project, the effect of multi-step copper surface oxidization, base pressure vacuum in the middle of the process, and integration of Cu enclosures on suppressing the ND will be discussed. The technique is based on the self-cleaning characteristics of copper oxides and the metal evaporation in a high vacuum at high temperatures. The ND has reduced to ~5 nucleations/cm^2 on average (an improvement compared to the previously reported minimum value, ten nucleations/cm^2 which was obtained using copper enclosures), and the graphene/copper surface has become smoother. The self-aligned graphene island geometry and shape of the flakes have reflected the symmetry and the single crystallinity of graphene.

The final project will discuss the growth of cm-scale graphene flakes on Cu and 3D-multilayered graphene on 3D-Ni foams and used Ni's gettering carbon diffusion effect to make the Cu foil carbon-free. The Ni-foam/Cu enclosure was oxidized in situ to assist with the self-cleaning process of metal oxides. The ND has been reduced to ~0.57 nucleation/cm^2 and obtained cm-scale graphene flakes.

INDEX WORDS: Single-crystal graphene, LPCVD, Enclosures, Nucleation density limitation, Catalyst surface oxidation, Self-Aligned Single-Crystal Graphene flakes, 3D Graphene nickel foam electrodes, 2D Materials.

Single-Crystalline Graphene by Low-Pressure CVD Method: Nucleation Limited Growth, Transfer, and Characterization

by

Sajith Madushan Wijayarathna Withanage

Committee Chair: Ramesh Mani

Committee: Unil Perera

Sidong Lei

Douglas Gies

Electronic Version Approved:

Office of Graduate Services

College of Arts and Sciences

Georgia State University

August 2021

DEDICATION

This work is dedicated to my parents Mr. Wijayarathna Withanage and Mrs. Padmini Jayasinghe, brother Mr. Tharindu, sister-in-law Mrs. Yohani, and my wife, Mrs. Asha.

ACKNOWLEDGEMENTS

I want to thank my academic advisor, Prof. Ramesh G. Mani, for his support during my Ph.D. at Georgia State University. I want to express my deepest gratitude to him for assigning this wonderful research area to me and supporting my conference presentations and publications. I want to pay my tributes to our lab member/postdoctoral researcher Late Dr. Annika Kriisa, for her tremendous support by providing exceptional SEM scans and valuable insights for my research work. When I wanted specific SEM scans for my publications, she worked for longer hours without hesitation to provide me with all SEM scans on time. I want to extend my sincere gratitude to Dr. Sidong Lei for providing access to his lab facilities and Ms. Aisha Okmi for providing me with essential chemicals that I needed to make my research work successful. I would also like to acknowledge my funding sources, the US Department of Energy, the Army Research Office, and the National Science Foundation.

I want to especially thank Prof. A. G. Unil Perera for recommending me for the role of APS student ambassador for Georgia State University. I gained vast experience by representing GSU at the APS leadership meeting held at the Congressional office in Washington DC. Also, I want to thank him for giving advice and encouragement since the first day at the university. I want to thank the physics department and the department chair, Prof. Sebastien Lepine, for providing funding for attending APS March meetings every year. These experiences helped me build my courage & confidence and were helpful to survive in challenging situations during my Ph.D. at GSU.

I want to thank all my committee members, Prof. A. G. Unil Perera, Prof. Sidong Lei, and Prof. Douglas Gies, for their support and very useful insights during my prospectus. I want to thank all of them again for agreeing to join as committee members for my Ph.D. defense despite their

busy schedules. Also, I want to thank the graduate director, Prof. Murad Sarsour, for his directions and advice for keeping me on track during my thesis writing. Furthermore, I want to thank the department chair, Prof. Sebastien Lepine, for arranging meetings to discuss my research work and valuable advice and encouragement.

Many thanks to my former lab mates, Dr. Rasanga Samaraweera, Dr. Zhuo Wang, Dr. Han-chun Liu, Mr. Binuka Gunawardana, Mrs. Rasadi Munasinghe, for their teaching and helping to improve my lab skills. Also, I want to thank all my current lab mates, Mr. Tharanga Nanayakkara, Mr. Kushan Wijewardena, and Mr. Rameshwor Poudel, for their kind help for my daily work. Many thanks to all of my colleagues at the department, especially Mr. Rupesh Ghimire and Mr. Timothy Jordan, for being supportive during all of these years. Finally, I want to thank all staff members at the physics department and all members at the instrument shop, especially Mr. Peter Walker, for their kind support.

TABLE OF CONTENTS

ACKNOWLEDGEMENTS ..... **VI**

LIST OF TABLES ..... **XI**

LIST OF FIGURES ..... **XII**

LIST OF ABBREVIATIONS ..... **XXVIII**

1 INTRODUCTION **1**

1.1 Dissertation Overview **1**

1.2 Background **3**

1.2.1 The Grand Origin ***3***

1.2.2 The Story of Carbon ***4***

1.2.3 Flatland: The Romance of Two Dimensions ***11***

1.3 Motivation **13**

2 GRAPHENE THEORY **16**

2.1 Physics of graphene **16**

2.1.1 Electronic state of monolayer graphene ***16***

2.1.2 Electronic state of bilayer graphene ***27***

3 GRAPHENE SYNTHESIS METHODS **34**

3.1 Overview **34**

3.2 Exfoliation of graphite **35**

3.2.1 Chemical exfoliation ***35***

3.2.2 Mechanical exfoliation of graphite 42

3.3 Epitaxial growth of graphene on substrates 45

3.3.1 Graphene growth on Silicon Carbide (SiC) 45

3.3.2 Chemical vapor deposition (CVD) method 48

4 THE ROLE OF SURFACE MORPHOLOGY ON NUCLEATION DENSITY LIMITATION DURING THE CVD GROWTH OF GRAPHENE AND THE FACTORS INFLUENCING GRAPHENE WRINKLE FORMATION 60

4.1 Introduction 60

4.2 Experimental Methods 62

4.2.1 Electropolishing and graphene growth 62

4.2.2 Sample preparation and characterization 65

4.3 Results & Discussion 65

4.4 Conclusion 71

5 THE EFFECT OF MULTI-STEP CU SURFACE OXIDIZATION ON THE GROWTH OF SINGLE-CRYSTAL GRAPHENE BY LOW-PRESSURE CHEMICAL VAPOR DEPOSITION (LPCVD) 73

5.1 Introduction 73

5.2 Experimental Methods 74

5.2.1 Copper surface modification and enclosure preparation 74

5.2.2 Gas feed control, annealing, and graphene growth 76

5.2.3 Characterization and Graphene Transfer 80

5.3 Results and Discussion 87

5.4 Conclusion 98

6 HIGH CRYSTALLINE CM-SCALE CVD GRAPHENE FLAKES GROWN ON COPPER USING A NI-FOAM ENCLOSURE (NI/CU/NI SANDWICH) 100

6.1 Introduction 100

6.2 Experimental Methods 101

6.2.1 Cu foil and Ni-foam surface modification and nickel enclosure preparation (Nickel/Cu/Nickel sandwich) 101

6.2.2 2-D & 3-D graphene growth on Cu foil strip and Ni-foam enclosure 103

6.2.3 Characterization 105

6.3 Results and Discussion 105

6.4 Conclusion 111

REFERENCES 113

LIST OF TABLES

Table 4.1 AFM - Roughness data for as-received (unpolished) and polished Cu foils taken at different regions. 69

LIST OF FIGURES

Figure 1.1 Illustrates the phase transitions that the quark-gluon plasma underwent in the early universe, which produces hadrons. These hadrons are the building blocks of all matter in the universe, made of up and down quarks. [4] 3

Figure 1.2 The triple-alpha process (Helium fusion), [7] a series of nuclear fusion reactions that create carbon (^{12}C) from three alpha particles (helium-4 or ^{4}He)..... 4

Figure 1.3 The first reproducible and verifiable synthetic diamonds. [10] (a) 1 mm diamond photographed with a phonograph needle. (b) 0.2-0.5 mm octahedral diamonds..... 6

Figure 1.4 Schematic representation of the Eight allotropes of carbon: (a) diamond, (b) graphite, (c) lonsdaleite, (d) C_{60} buckminsterfullerene, (e) C_{540} fullerite, (f) C_{70} fullerene, (g) amorphous carbon, and (h) single-walled carbon nanotube. (Image Source: Wikimedia Commons)..... 7

Figure 1.5 Schematic representation of the hybridizations for the carbon atom: (a) hybridization sp, (b) hybridization $sp^{2,}$ and (c) hybridization sp^3. [22, 23] 8

Figure 1.6 Carbon hybridization. (a) The ground state of carbon. The 1s electron clouds are not shown here since those are small and tightly linked to the nucleus, so they do not form bonds. Two paired spherical 2s electrons (orange sphere) are symbolized with up and down arrows [↑↓]. Additionally, it contains two unpaired $2p_x$ and $2p_y$, p-orbital electrons aligned on the x-y axes. When an atom comes closer to a carbon atom, one of the 2s-orbital electrons gets pulled into a high-energy orbital which is $2p_{z,}$ as shown in Figure 1.6b. (b) The excited state of carbon. The orange-dotted arrow represents the transition of an electron from 2s-orbital to 2pz high energy orbital. The orange sphere is still present because there is one electron in the 2s-orbital. (c) Hybridized state of carbon. Four electrons

in the 2s, $2p_x$, $2p_y$, and $2p_z$ blend together to form sp^3 hybridized orbitals, which have the same shape as shown in Figure 1.6c (the left image). Since there are one "s" orbital and three "p" orbitals in the configuration, it is called sp^3. [26] 10

Figure 1.7 A SEM image (taken at 12,000X magnification) of a carbon nano-foam produced by the Pulsed laser deposition (PLD) method. [30] 11

Figure 1.8 Metal–graphene–metal (MGM) photodetector. Top left: 3-D schematic of the device. Bottom right: scanning electron micrograph of the same device. The device structure is similar to typical metal–semiconductor–metal (MSM) detectors, but they have replaced the semiconductor layer with an exfoliated bi-layer graphene, which acts as the device's active layer. (Scale bar, 5 mm). [51] 12

Figure 2.1 (a) Honeycomb structure of graphene in real space. The a_1 & a_2 vectors and two non-equivalent carbon atoms (A and B atoms), which are contained in a rhombus-shaped unit cell, define the Bravais network. (b) Graphene's first Brillouin Zone (FBZ) (shaded area) in the reciprocal lattice formed from the two atom Bravais lattice. Γ is the center of the FBZ, and the K and K' are on the corners while M represents the middle point between K and K.' The Dirac cones meet at the K and K' points. [128] 16

Figure 2.2 (a) Bonding arrangement between two carbon atoms in graphene. The sp^2 hybridized orbitals form the σ-bonds, which are strong and contribute to the hexagonal shape of graphene, resulting in a super-strong material. This bond lies on the plane of sp^2-orbitals. The p_z electrons contribute to form weak and delocalized π-bonds, responsible for the conduction of graphene and other carbon allotropes. (b) honeycomb-like structure, the building block of all carbon allotropes which contains delocalized π-electrons. [129, 130] 17

Figure 2.3 (a) The π and π* bands linearly intersect at the edge of the Brillouin zone (K, K' points in Figure 2.1b). [133] Fermi energy is located precisely at this intersection which is known as Dirac point where E=0. (b) Conical, linear dispersion (Dirac cone) near the K and K' points (Fermi level). [138] 22

Figure 2.4 The band structure of single-layer graphene, which is related to Figure 2.1 and Figure 2.3 (a) an illustration of six valleys of non-equivalent types of K and K', known as Dirac cones. (b) Top view of the K and K' points/valleys (Dirac cone), which represent the pseudo-spin up ($\sigma +$) and down ($\sigma -$) for electrons and holes. The pseudo-spin and the direction of motion are related to each other (c) Schematic of pseudo-spin at K and K' points in the k-space. There are two configurations as follows, (i) indicates the orientation of the pseudo-spin σ in the conduction band (for $s > 0$), which is $\sigma +$(red) parallel to the wave vector ($\boldsymbol{k}$). (ii) Indicates the orientation of the pseudo-spin σ in the valence band (for $s < 0$), which is $\sigma -$(blue) anti-parallel to the wave vector ($\boldsymbol{k}$). [146-149] 26

Figure 2.5 AB Crystal structure of the bi-layer graphene. (a) top/plan view of the crystal structure. On the top layer, $A2$ and $B2$ atoms are represented by black and gray dots, respectively. On the bottom layer, $A1$ and $B1$ atoms are represented by white and black dots. Electron orbitals of $A2$ and $B1$ atoms are more strongly linked than the interactions between other layers (called "dimer" atoms) because the $B1$ atom is located directly below the $A2$ atom (represented by the top-left black dot labeled as $A2B1$. Contrarily, Electron orbitals of $A1$ and $B2$ atoms are relatively weakly connected (called "non-dimer" atoms) because there are no atoms directly above or below $A1$ and $B2$ atoms (represented by the top-right white and grey dots, which are labeled as $A1$ and $B2$ within the diamond shaped shaded area). (b) side view of the crystal structure. $\gamma 0$ is the in-plane nearest-neighbor hopping

parameter. Here, three interlayer parameters are represented as $\gamma 1$, $\gamma 3$ and $\gamma 4$. The unit cell can be taken as the diamond shown in (a) and contains the upper $B2$ and lower $A1$ atoms. [132, 133, 138] 28

Figure 2.6 Low-energy bands and the dispersion relation for graphene bi-layers (AB stack) arising from 2pz orbitals. It has been plotted in the reciprocal space along the kx direction. 30

Figure 2.7 (a) Bottom-left: Low-energy band structure near the K-point in bilayer graphene. The parabola, which represents the E with an effective mass m, is tangent at E=0. (b) Same bilayer graphene sample under the influence of an external electric field/bias voltage $vb = \triangle$. The band gap is opened by two times the applied field, $\triangle g = 2 \triangle$ than the non-biased state, [153] when a perpendicular electrical displacement field is applied to bi-layer graphene, and this $\triangle g$is tunable. [154-156] 32

Figure 3.1 Flow chart of available graphene fabrication techniques. [157] 34

Figure 3.2 Schematic representation of (a) bottom-up and (b) top-down process of graphene synthesis. [158] 35

Figure 3.3 The TEM images of high crystalline graphene flakes prepared by water/surfactant method. (a) a monolayer graphene flake with square-shaped debris on the left, which contains fewer defects compared to the other exfoliation methods. (b) a bilayer graphene flake. The scale bar is 500 nm. [160] 36

Figure 3.4 A step-by-step illustration of staging in GICs. Here, purple balls (Potassium) represent the intercalant layers, and gray hexagonal networks represent the graphene layers. [164] 37

Figure 3.5 Schematic illustration of the procedure known as “graphene liquid-phase exfoliation.” Here, the top-right shows the process involving an ultra-sonication and a solvent such as

N-methyl-2-pyrrolidinone (NMP). The bottom-right represents the method that involves surfactants/intercalants, as discussed in the previous section. [184] 39

Figure 3.6 Schematic of chemically converted reduced graphene oxide (rGO) preparation method by the exfoliation of graphite oxide. [192] 40

Figure 3.7 Mechanical exfoliation of HOPG using scotch tape in order to make graphene flakes thinnest as possible. [212]..... 44

Figure 3.8 Illustrations of crucial stages of the few-layer and multi-layer graphene growth by thermal decomposition of SiC. (a) before (left) and after the growth of graphene on SiC and few-layer graphene (blue lines) and the buffer (blue dashed line) layers are visible. The 3D model on the right-hand side represents the structural model of double-layer graphene. (b) crystal structure of SiC and graphene on Silicon-terminated surface and Carbon-terminated surface. Red balls correspond to the silicon atoms, and the blue balls represent the carbon atoms. (c) 3D diagram of a graphene field-effect transistor (GFET). It has been fabricated using a gate insulator of $Al2O3$ and a Ti/Au gate electrode. [218] 46

Figure 3.9 Schematic of a typical CVD system with a quartz tube furnace. Mass flow controllers (MFCs) regulate the gas flows and then feed into the quartz chamber known as the reactor. The reactor is heated using a heater/heating element, and the pressure control valve regulates the reactor pressure. The vacuum pump on the right-hand side uses to remove exhausted gases. [252-254]..... 48

Figure 3.10 Schematic of the precursor decomposition during the CVD growth of graphene at a catalytic surface and the boundary layer above the catalyst surface. (a) a step-by-step precursor decomposition process. (b) The boundary layer is thicker when the substrate is

parallel to the direction of the flow. (c) The boundary layer is thinner than (b), and the substrate is tilted against the main flow direction. [252-254]..... 49

Figure 3.11 A schematic of carbon segregation at Ni-catalyst surface and a representation of graphene growth on Ni (nickel) with different cooling rates (extremely fast, fast/medium, slow). [258]..... 51

Figure 3.12 Illustrations of the graphene synthesis process on Ni. (a) Growth on a monocrystalline Ni (111) surface gives monolayer graphene. (b) Growth on a polycrystalline nickel surface that contains defects and grain boundaries. This gives multilayer and monolayer graphene. (c) Optical microscopy image of a graphene/monocrystalline-nickel which related to (a) and the inset shows a 3D diagram of monolayer graphene on Ni (111). (d) Optical microscopy image of a graphene/ polycrystalline-nickel, which corresponds to (b). The inset represents a 3D representation of monolayer and multilayer graphene on the polycrystalline-nickel surface. [259] 52

Figure 3.13 Illustration of the significant differences and the growth kinetics during the graphene synthesis via (a) precipitation on nickel and (b) by surface-mediated growth on copper. [260]..... 54

Figure 3.14 Schematic diagram of the physicochemical stages of the CVD synthesis (1) precursor transport from the bulk gas region into the reactor (2) evaporation of reactant gases (3) reactant gases chemically reacts to form immediate reactants and also produces the gaseous by-products (4) Diffusion of reactant gases from the bulk gas region to the catalyst surface through the boundary layer (5) Adsorption of the reactants on the deposition surface of the substrate (6) Surface diffusion of reactant gases to growth sites, where nucleation happens and formation of graphene islands at the surface (7) Desorption of volatile by-products

from the deposition surface to the bulk gas region (8) Gaseous by-products move away from the reactor. [261] 54

Figure 3.15 Schematic illustrations of all possible distribution of carbon isotopes. It is based on various growth procedures and kinetics discussed in this section (a) a layer of graphene formed on a catalyst surface by carbon isotopes mixed randomly. First, the precursors went through a dissolution step, and graphene was formed via surface segregation and precipitation. (b) Graphene formed with separated isotopes. It forms via two separate surface adsorption steps. (c) Combined growth by precipitation and surface adsorption. [262] 56

Figure 4.1 A cm x 5 cm, 25 μm thick industrial Cu foil is dipped in a 10% Acetic Acid solution (CH3COOH) for 1 min, rinsed with distilled water, dried with a flow of $N2$, and oxidized by heating up to $350\ 0C$ in open-air for 40 min. The foil is folded into Cu-Enclosure, with side A closed and B, C pressed. 62

Figure 4.2 a) A schematic of the CVD tube furnace growth system. b) The graphene growth curve. The system base pressure was 22 mTorr, and the total pressure during growth was ~1 Torr. 64

Figure 4.3 (a) An AFM image of an as-received industrial Cu foil. Here, the square and the circle indicate a valley & a pit, respectively, and the parallel dashed lines indicate cold-rolling striations (also for a-g). (b, c) An optical microscope (OM) image of as-received industrial Cu foil after graphene growth. Here, the white dashed curves (also for b, c & f) mark grain boundaries while the rectangles (also for b-d, f & g) cover the valleys which survived through the growth process. (d) OM image of Graphene/SiO2/p-Si (with graphene is grown on received industrial-Cu) after the wet transfer process. (e) AFM image of an

electropolished Cu foil. (f) Optical microscope image of graphene on electropolished copper. Notice the star-shaped graphene crystallites. (g) Optical microscope image of Graphene/SiO2/p-Si, where the graphene was grown on electropolished copper. Compare with Figure 4.3d. (h) An illustration of how wrinkles are formed due to an extra graphene area. 67

Figure 4.4 (a) An SEM image of a Cu grain boundary. The square shows fissures/cracks formed due to different thermal expansion coefficients. Arrows represent wrinkle formation due to Cu grain boundaries. (b-c) SEM images of Nano-scale wrinkles formed due to different thermal expansion coefficients of Cu and graphene. (d) An AFM image of a Cu grain boundary (before the graphene growth but after the annealing step) and valleys. (e) An AFM image of graphene (on Cu) wrinkle at a grain boundary. (f-g) OM images of graphene flakes ("f" represents a sample that used an electropolished Cu substrate & "g" for a non-electropolished Cu) with cracks and grain boundaries. Arrows show the cracks, and the rectangle shows the grain boundaries. (h) An AFM image of inset in Figure 4.4g. The arrow shows a crack, and this has been scanned using the AFM. 70

Figure 5.1 The LPCVD furnace. (a) The exterior of the furnace with the temperature controller and the thermocouple. (b) The inside of the furnace during the slow cooling phase. 77

Figure 5.2 The modified LPCVD system. (a) The setup consists of four gas feeds controlled and monitored by two flow meters, few needle valves, and the LPCVD PC. The LPCVD system receives data from four digital multimeters (B), and the flow meters are controlled by a four-channel MKS digital readout (A). Here, $V1$, $V2$, $V3$, and $V4$ indicate four vacuum pumps. The pressure values are monitored by a multimeter-digital thermocouple vacuum

gauge pair and analog pressure gauges (C). (b) The gas control panel. (c) The needle valve consists of a barrel-thimble micro-gauge. It was crucial to fine-tune the $CH4$ gas flow. 78

Figure 5.3 A schematic illustration of the LPCVD system. Four gas inlets feed $O2$, $N2$, $H2(10\%)/Ar(90\%)$, $CH4$ into the CVD tube furnace chamber at different stages of the LPCVD process. The inner diameter of the quartz tube was around 3cm, and the sample was placed in the middle of the heating element (isothermal zone) to ensure a uniform temperature along with the Cu pocket. Moreover, the enclosure was positioned carefully inside the quartz tube by considering the enclosure geometry and gas-phase dynamics to achieve a uniform reactant concentration and temperature. It helps to control the near-surface conditions so that the deposition becomes more homogenous and controllable. The maximum growth temperature of the reactor was $10600C$ and achieved a base pressure value of ~30 mTorr. 79

Figure 5.4 A graphical representation of the temperature (left-axis), pressure (right-axis), and the overall growth profile of the LPCVD process. The temperature (black curve) was ramped up to $9000C$ from $300C$ and then gradually brought to $10600C$, as shown on the left axis. The red curve and the right axis represent how the pressure values changed during the entire growth process. This growth profile consists of seven stages, including two annealing and growth steps. In addition to the pre-oxidization step, the enclosure was oxidized twice during the LPCVD process by providing a controlled flow of $O2$ before each growth cycle. It increases the concentration of oxygen atoms which helps to reduce graphene nucleation. At the end of the growth, the temperature set value was immediately adjusted to $300C$ and let the system cool down slowly while keeping the gas flow rates

unchanged. The presence of oxygen atoms and the stability of $Cu2O$ below $10000C$, discourage further growth of graphene during the cooling cycle. 80

Figure 5.5 (a) An image of the OLYMPUS BH2-MJL Optical Microscope (OM) and this microscope can magnify images up to X100. The raw image is captured by a digital microscope camera (DM) that feeds it into an image viewer software. (b) A picture of the dry transfer system contains an optical microscope, a digital microscope camera, a micromanipulator, a glass slide holder, a heating element, a Si chip holder, and a vacuum pump. The Gold/$SiO2$/Si chip holder was heated to $45 \pm 50C$ to favor the van der Waals force between graphene and gold/$SiO2$/Si chip as well as to weaken relatively strong adhesion forces between graphene and PDMS. The OM/DM system was used to capture the live image, and then adjustments were made to coincide the graphene sample and the contact pattern. The micromanipulator was used to move the graphene/PDMS/glass slide vertically and horizontally so that the graphene flake and the gold contact pattern touch each other. 82

Figure 5.6 Optical images of individual graphene flakes on PDMS at X50 magnification (a & b) flakes with diagonal lengths around $45 \pm 5\ \mu m$ (c & d) relatively larger graphene flakes with diagonal lengths over $75\ \mu m$. All of those flakes were clean, and the black dots were air bubbles trapped between glass and PDMS that do not affect the graphene transfer. These films were air-dried and free of water. The existing wet and dry transfer methods introduce polymer residue and impurities such as ions and water, affecting graphene quality negatively. More importantly, when using the PMMA wet transfer method, some water molecules were trapped between graphene and $SiO2/Si$ chip. That considered one of the significant drawbacks of wet transfer methods. However, in this method, the possibility of

having such impurities and residue is very minimum. All flakes have a square shape, and green dashed lines mark the edges of graphene flakes. 83

Figure 5.7 A schematic illustration of the hybrid transfer of graphene (2-D materials) onto a specific location on a flat and smooth substrate (here, a $Si/SiO2$ chip with a golden contact pattern). It is crucial to pick a graphene flake that fits between the + signs of the gold contact pattern to prevent short-circuiting the device. First, the Cu/Graphene sample was cleaned with a quick blow of $N2$ gas to remove any dust particles on the surface. Then a dust-free PDMS piece and the Graphene/Cu foil were firmly pressed such that no air bubbles (blisters) were left between the surfaces. It was let to float on a $FeCl3$ solution to etch away the metallic copper. The PDMS/graphene stack was left to float on deionized water to dissolve the remaining $FeCl3$ without making any disturbances so that water will not leak between two layers. Then it was placed on a glass slide (by forming a glass/PDMS/graphene stack) to dry and removed the excess PDMS. After that, it was placed on a micromanipulator such that the graphene side faces down. A cylindrical Cu block was used as the stage to hold the Si chip with a gold contact pattern, and the graphene flake was transferred onto it by using the micromanipulator. A heating element was used to heat ($45 \pm 50C$) the Si chip to favor an easy transfer. This novel hybrid transfer method combines wet and dry transfer techniques. It was developed by taking advantage of weak van der Waals forces and relatively strong adhesion forces between graphene/PDMS interface..... 85

Figure 5.8 Optical microscopy images of the graphene flakes during different stages of the hybrid transfer process. (a) This is the same graphene flake shown in Figure 5.7. Here, the flake is on a PDMS piece/glass slide, and the pinkish purple color of the background came from

the $SiO2/Si$ chip underneath. The surface has a minimal amount of residues which is negligible. Despite the low contrast between transparent graphene and PDMS, the flake is still visible that is enclosed by a dashed line (green). (b) The chip with a gold contact pattern, graphene flake, PDMS, and glass slide are touched together during the transfer of graphene flake from PDMS to Si chip. The bluish color without any bubbles confirms a good contact between the chip and the flake. (c) The graphene/gold/$SiO2/Si$ chip after the successful transfer of graphene without any residue taken after the PDMS liftoff. 86

Figure 5.9 A schematic representation of the graphene growth mechanism inside and outside the Cu enclosure during the growth cycle-I. (a) Side view of the copper enclosure that is made of ~25 μm thick pre-oxidized Cu foil. The main gas flow includes $N2$ and $H2/Ar$. The tightly folded edges are welded together during the heating phase due to the high temperature ($10600C$) closer to the meting point of Cu. It seals the interior of the pocket from the outside and forms a static equilibrium inside the pocket. (b) The evaporation and diffusion mechanisms of carbon atoms in bulk and on the surface of copper foil before the oxidation step-I. The inner oxide layer is decomposed and formed a thin $Cu2O$ layer. (c) The oxidation step-I of copper and oxygen diffusion into the copper foil. (d) The oxygen evaporation on the outer layer and the oxide formation of a relatively oxygen-rich pocket interior. (e) Growth cycle-I. The mass transport, gas diffusion, surface adsorption, dehydrogenation/decomposition, surface migration & nucleation, growth of graphene islands, bulk diffusion of carbon into the Cu foil, and oxygen diffusion from the interior to the exterior. (f) Monolayer flakes are formed inside the pocket and prevent the formation of bi-layers by acting as a diffusion barrier for carbon. The mechanism of bi-layer graphene

formation on the exterior of the enclosure results from free radical deposition on the existing graphene flakes from the exterior gas environment. 90

Figure 5.10 A schematic representation of the full vacuum phase and oxidation phase-II before the growth cycle-II. (a) The full vacuum step. After shutting down the gas supplies, the system pressure starts to drop rapidly, and the rate of surface evaporation on the exterior is increased. It causes to decrease in the carbon atom percentage on the outer surface of the Cu foil. The interior is in static equilibrium, which encourages the diffusion of carbon and oxygen towards the exterior. It removes the additional nucleation sites and carbon on the inside surface and helps to suppress the nucleation density as a result. (b) Oxidation phase-II. At the end of the vacuum step, the carbon-free Cu surfaces oxidized by following the same steps as previous. This step is similar to part (c) of Figure 5.9 despite the graphene layers formed during the growth cycle-I. After this, the growth process is identical to the growth cycle-I (see Figure 5.9c-f). 93

Figure 5.11 The optical microscopy images of graphene flakes grown on Cu. This figure includes images that were taken from two samples. Figure 5.12a-b shows another sample grown under the same conditions. All samples showed similar characteristics. The first sample was scanned under different magnifications to study the surface conditions of graphene and Cu. (a-c) OM images of sample 1, taken under different magnifications (a) ×5 (b) ×10 (c) ×50 (d-f) OM images of sample 2, taken under ×5 magnification at different locations on the interior surface. All sample surfaces were clean of residue and smooth, which was uncommon under different growth methods. More importantly, all samples have a very low nucleation density. The chartreuse & blue lines shows the alignment between flakes, and

it will be discussed in Figure 5.12. Such features prove the higher quality of the graphene samples..... 95

Figure 5.12 (a & b) Optical microscopy images of graphene flakes and the surrounding area of sample 3. The images were taken under ×5 magnification and had a cleaner surface with a highly suppressed nucleation density. (c & d) Surface scans of two adjacent locations on sample 1 (see Figure 5.11a-c). These were also taken under ×5 magnification as Figure 5.11a. Both (c) and (d) show smooth surfaces and low nucleation densities, as shown in Figure 5.11a-c. Additionally, the flakes grown under this method are square-shaped and followed a vertical and horizontal alignment. It also follows this alignment when combining flakes and then creates a big square-shaped graphene flake. The chartreuse & blue lines show such alignments, representing the high crystallinity of the foil, which consists of Cu (100). 96

Figure 6.1 The images of Ni-foam and graphene/Cu samples at different stages of the growth process. (a) The oxidized Ni foam enclosure (Ni/Cu/Ni sandwich) just before the growth. (b) The 3D graphene/Ni-foam and the graphene/Cu strip after the growth. (c) The flatten graphene/Ni-foam. This by-product is reusable for another graphene growth cycle. More importantly, this 3D graphene on Ni-foam can be used as a 3-D high-performance electrode. 102

Figure 6.2 A graphical representation of the temperature (left-axis), pressure (right-axis), and the overall growth profile of the LPCVD process. The temperature (black curve) was ramped up to $8500C$ from $300C$ and then gradually brought to $10000C$, as shown on the left axis. The red curve and the right axis represent how the pressure values changed during the entire growth process. The enclosure was oxidized (pre-oxidization) during the LPCVD

process by providing a controlled flow of $O2$ before the growth cycle for 15 min. At the end of the growth, the temperature set value was immediately adjusted to $300C$ and let the system cool down slowly while keeping the gas flow rates unchanged. 103

Figure 6.3 A schematic illustration of the LPCVD system. Four gas inlets feed $O2$, $N2$, $H2(10\%)/Ar(90\%)$, $CH4$ into the CVD tube furnace chamber at different stages of the LPCVD process. The inner diameter of the quartz tube was around 3cm. The Ni-foam enclosure was placed in the middle of the heating element (isothermal zone) to ensure a uniform temperature along the enclosure. Moreover, the enclosure was positioned carefully inside the quartz tube by considering the enclosure geometry and gas-phase dynamics to achieve a uniform reactant concentration and temperature. The maximum growth temperature of the reactor was $10000C$ and achieved a base pressure value of ~33 mTorr. 104

Figure 6.4 The Cu/graphene foil after post-oxidation (optical visual enhancement). (a) The foil contains a cm-scale graphene flake on the right. Red arrows mark the sides which touched the nickel pocket edges. Side D is the main point of interest. The small graphene regions given by B-F can be avoided by preventing those sides from touching the enclosure edges. The blue arrow represents the possible growth directions of the hexagonal graphene flake. (b) The inset of (a) with a measuring scale. The diameter of the flake is larger than 1.3 cm. 107

Figure 6.5 A schematic representation of the 3D-graphene growth mechanism on nickel foam and single-crystalline graphene growth on the Cu strip. (a) Phase-I: Self-cleaning process and the initial stage of graphene growth. Here, the green and brown colors are used to represent the nickel and copper oxides, respectively. The carbon atoms are given by black dots. (b)

Phase-II: Carbon saturation process. Here the yellow color represents the carbon-free Cu strip. (c) Phase-III: 3-D and 2-D graphene growth process. The thick blue arrows on each side represent the 3-D graphene growth direction on Ni-foam. The thin blue lines represent the saturated carbon flow direction on nickel foam edges and the graphene flake growth direction on the Cu strip..... 109

LIST OF ABBREVIATIONS

Abbreviation	Meaning
LPCVD	Low-pressure chemical vapor deposition
TEM	Transmission electron microscopy
CMG	Chemically modified graphene
GIC	Graphite intercalation compounds
NMP	N-methyl-2-pyrrolidinone
GO	Graphene oxide
HOPG	Highly oriented pyrolytic graphite
AFM	Atomic force microscope
STM	Scanning tunneling microscope
SEM	Scanning electron microscope
GFET	Graphene field-effect transistor
QHE	Quantum hall effect
MFC	Mass flow controller
ND	Nucleation density
PMMA	Poly (methyl methacrylate)
OM	Optical microscope
DM	Digital microscope
ND	Nucleation density
BP	Base pressure
TP	Total pressure

PDMS	Polydimethylsiloxane
PPC	Polypropylene carbonate
PVA	Polyvinyl alcohol
APCVD	Atmospheric Pressure CVD
BLG	Bilayer graphene

1 INTRODUCTION

1.1 Dissertation Overview

This dissertation consists of six chapters. Chapter 1: The introduction contains three sections: the dissertation overview, background, and motivation. In the background section, I will briefly discuss the origin of carbon, the discovery of carbon allotropes, the hybridization of Carbon, and the importance of 2D materials.

Chapter 2 includes the theory and properties of graphene. I will discuss the crystal structure of monolayer graphene, the derivation of wave function using the tight-binding model, and effective mass approximation. In addition, I will derive the wave function of two-layer graphene and discuss the peculiar tunneling effect of graphene.

Chapter 3 introduces graphene synthesis methods and the quality of graphene produced by those methods. Such methods include the chemical & mechanical exfoliation of graphite, and the epitaxial growth, including chemical vapor deposition (CVD). The CVD section, which is 3.3.2, includes vital information about the CVD graphene growth on Cu and Ni catalysts. It will be helpful to understand clearly the concepts given in chapters 4, 5, and 6.

Chapter 4 is an expanded version of an article, which was published in MRS Advances, a peer-reviewed journal in 2019 [1] based on my research work. It is focused on the role of surface morphology on nucleation density limitation during the LPCVD growth. Moreover, I will discuss the factors influencing graphene wrinkle formation.

In chapter 5, my research work on the effect of multi-step Cu surface oxidization on the growth of single-crystal graphene by LPCVD will be discussed. Here, I have used the “self-cleaning’ properties of copper oxides, forming a static equilibrium inside the enclosure, and the

partial surface evaporation in a vacuum at high temperature to develop the growth method. The initial findings of this research project were presented at the APS March Meeting in 2019. [2] Moreover, I have introduced a wet-dry-transfer technique to transfer residue and a wrinkle-free transfer method. The initial observations were submitted to the APS March Meeting (virtual) in 2020 (the Bulletin of the American Physical Society). [3]

Chapter 6 presents a study of high crystalline cm-scale CVD graphene growth on copper using a Ni-foam enclosure and has obtained cm-scale graphene flakes. Furthermore, this method also produces 3D-graphene-Ni-foam as a byproduct, and that considers a high efficient 3D electrode in the battery and supercapacitor industry.

My primary purpose in this research is to develop high-quality single-crystalline graphene (SLG) growth methods as a materials grower. Hence, chapters 4, 5, and 6 are interconnected. In other words, some of the methods discussed in chapter 4 are also used to develop the growth methods discussed in chapters 5 and 6. Also, some of the methods/findings introduced in chapter 5 have been used to develop the methods discussed in Chapter 6. More importantly, instead of repeating some of the sample preparation methods and descriptions, I have given proper cross-references to chapters 4 and 5 while writing chapters 5 and 6. Furthermore, each chapter (4, 5, and 6) includes a separate conclusion section that summarizes the findings of the corresponding chapter.

1.2 Background

1.2.1 The Grand Origin

The widely accepted scientific description of the universe is the idea of an evolving hierarchical cosmos expanding from the initial hot big bang for more than 13.7 billion years. The formation of all the atoms in the universe was made possible after this grand moment, and very shortly after the Big Bang, during the period of so-called cosmic inflation, the universe, which was filled with highly homogeneous energy, began to increase its volume exponentially, thus reducing its energy density.

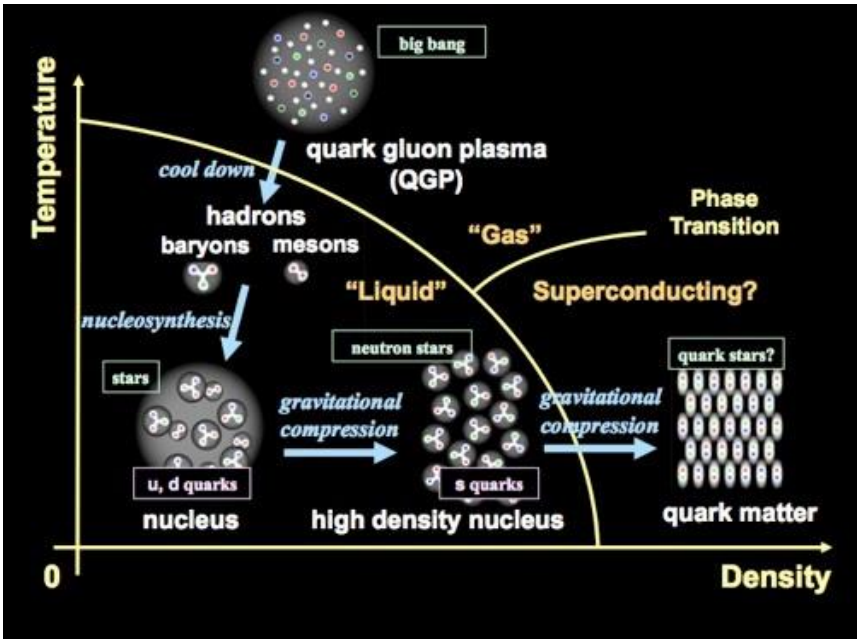

Figure 1.1 Illustrates the phase transitions that the quark-gluon plasma underwent in the early universe, which produces hadrons. These hadrons are the building blocks of all matter in the universe, made of up and down quarks. [4]

The universe's temperature decreased many times during this time, and very fast-moving solid particles were formed simultaneously. After the end of inflation, the acceleration of the universe's growth slowed down, but its expansion never ended. Then quarks, leptons, and gluons formed a very dense plasma (as shown in Figure 1.1), which prevented chemical bonds. Due to

the gradual expansion and cooling of the universe, quarks and gluons bound to hadrons, [5] and a few minutes after the Big Bang, the universe was filled with 75% hydrogen and 25% helium. The universe expanded for about 100 million years and atoms, then clustered under gravity to form objects similar to today's stars but were much larger and made entirely of hydrogen and helium. [6] Nuclear fusion of hydrogen in the stars also formed helium, the concentration of which decreased towards the center of the stars. The high temperature and pressure inside the stars have allowed nuclear fusion to continue, thus creating new elements, including carbon, as shown in Figure 1.2, which is currently the fourth most abundant element in the universe after hydrogen, helium and oxygen.

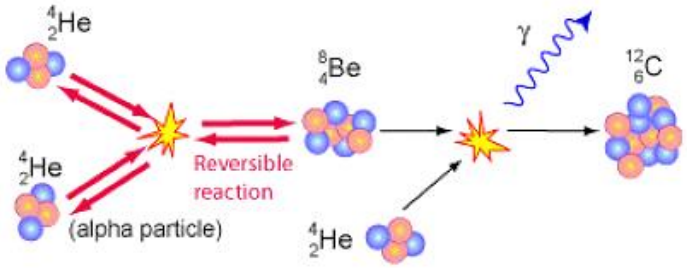

Figure 1.2 The triple-alpha process (Helium fusion), [7] a series of nuclear fusion reactions that create carbon (^{12}C) from three alpha particles (helium-4 or ^4He).

1.2.2 The Story of Carbon

1.2.2.1 Discovery and allotropes of carbon

Carbon is a non-metallic and non-magnetic material that is widely distributed by nature, so that it is one of the most basic elements of all organic compounds and thus essential for the origin of life on Earth. This fact is strongly related to how carbon combines with other chemical elements to form complex molecules. We can see this versatility by comparing it with other chemical elements: while oxygen can bond to only two atoms and hydrogen with only one, carbon has the possibility of forming up to four bonds with other elements. This fact allows carbon to form a wide

variety of complex molecules of different sizes and shapes. Another possibility that the carbon element offers is combining with itself differently through different types of chemical bonds. This ability to make different chemical bonds and generate complex structures is associated with the different forms of hybridization that the carbon atom can take on.

Materials consisting only of carbon atoms can exist in different structural forms with very different physical properties. Diamond, graphite, and amorphous carbon in the form of charcoal have been known for thousands of years, but by the end of the 18th century, it was clear that they were different forms of the same substance. In 1772, an experiment was carried out by the French chemist A. Lavoisier, in which the same amount of precisely weighed diamond and charcoal was placed in closed vessels. These samples were then melted by concentrated sunlight. It was observed that in both cases, the same amount of carbon dioxide was produced in the absence of water vapor, from which A. Lavoisier concluded that they were materials of the same substance.

A similar experiment in 1779 by C. W. Scheele and in 1886 by C. L. Berthollet proved that the combustion of graphite also produces carbon dioxide. However, during this process, a small amount of iron was formed simultaneously, [8] considered a necessary part of the graphite structure. The name Carbo (brand C) was introduced for the form of carbon formed during the combustion of graphite, which from the Latin translation means charcoal. In 1789, in his treatise on the *"Elements of chemistry,"* [9] A. Lavoisier included carbon as an element and is thus considered its discoverer. It was not until 1855 that B. Brodie proved that graphite was only an iron-free carbon material by burning graphite. One hundred years later, in 1955, the conversion of graphite to diamond (as shown in Figure 1.3) was achieved at high temperatures and pressures.

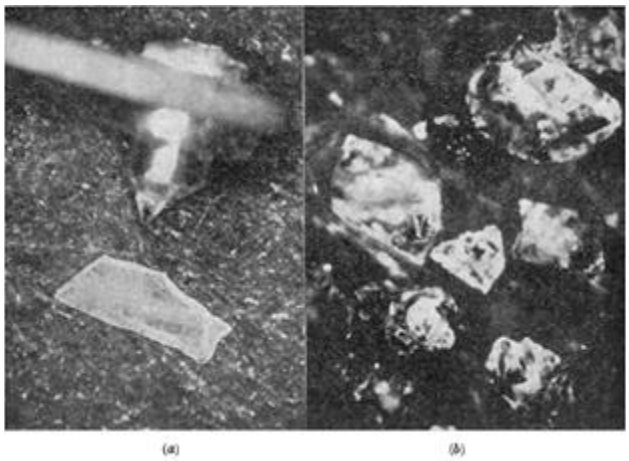

Figure 1.3 The first reproducible and verifiable synthetic diamonds. [10] (a) 1 mm diamond photographed with a phonograph needle. (b) 0.2-0.5 mm octahedral diamonds.

The properties of all materials change significantly as their thickness decreases. Therefore, a large amount of research focused on creating the thinnest possible layers. However, since 1935, theories have emerged [11-14] that any two-dimensional crystal cannot be thermodynamically stable because the thermal oscillations of its crystal lattice would be greater than the interatomic distances. This consensus initially surfaced due to the views summed up in the book named "*Statistical Physics"* by Landau and Lifshitz [12] under the sections that describe the stability of 2D crystals. It was later defined as the Mermin-Wagner theorem [15] with the idea that the long-ranged thermal displacement fluctuations are favored by the system for their entropy increase and are formed (in 2D crystals) with a bit of energy cost. What emphasizes that graphene crystals are unstable and should melt due to the displacement of carbon atoms into the 3rd dimension by exceeding the bond length between carbon atoms.

Subsequent experiments have also shown that the melting point of thin films decreases significantly, and their thickness is rearranged at the thickness of several tens of layers of atoms. In thin graphite layers, the carbon atoms were to be rearranged into an island or the structure of amorphous carbon. In 1952, a new stable carbon structure was discovered, carbon nanotubes, [16]

in which carbon atoms are arranged in a planar structure of hexagons and rolled into a cylinder with a diameter of 1-100 nm, schematically shown in Figure 1.4h. Their properties, i.e., low weight, high strength, and conductivity, are suitable for producing light composite materials, fabrics, and single-electron transistors. Another modification of carbon is fullerenes, which were discovered in 1985. [17] In this case, the carbon atoms are arranged in pentagons and hexagons on the surface of an imaginary sphere or ellipsoid.

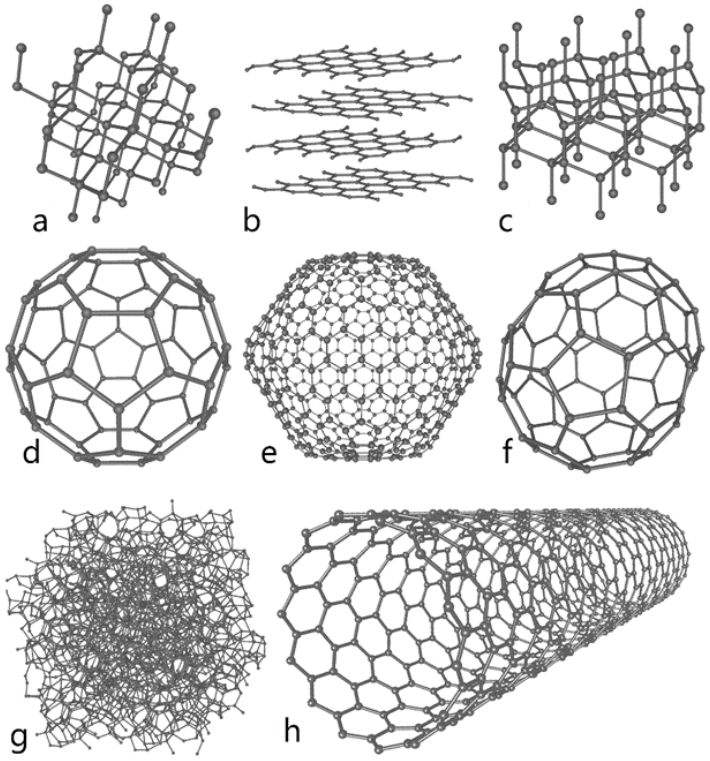

Figure 1.4 Schematic representation of the Eight allotropes of carbon: (a) diamond, (b) graphite, (c) lonsdaleite, (d) C_{60} buckminsterfullerene, (e) C_{540} fullerite, (f) C_{70} fullerene, (g) amorphous carbon, and (h) single-walled carbon nanotube. (Image Source: Wikimedia Commons)

The most stable and common fullerene is the C_{60} molecule (buckminsterfullerene) shown in Figure 1.4d, formed by a series of chemical structures with 44 to 90 carbon atoms, while those with 60 carbon atoms appearing in greater concentration. The first fullerene was discovered by bombarding laser beams on a graphite target at a temperature of 104 ^{0}C. [17] When fullerenes

enclose an atom or molecule, their properties are strongly affected. In general, however, they are very stable and resistant to external influences. At present, research in the field of fullerenes has focused mainly on their use in medicine. [18-20] For their discovery, R. Curl, H. Kroto, and R. Smalley received the 1996 Nobel Prize in Chemistry.

1.2.2.2 Hybridization of Carbon

It is known that this element is in column IV of the periodic table and has six electrons that can occupy the 1s, 2s, and 2p orbitals as shown in Figure 1.6 (ground-state electron configuration of carbon is $1s^2\ 2s^2\ 2p^2$), two of which are strongly linked to the nucleus ($1s^2$) and are considered core electrons. The rest are considered valence electrons, generally responsible for forming chemical bonds according to the valence bond theory. [21]

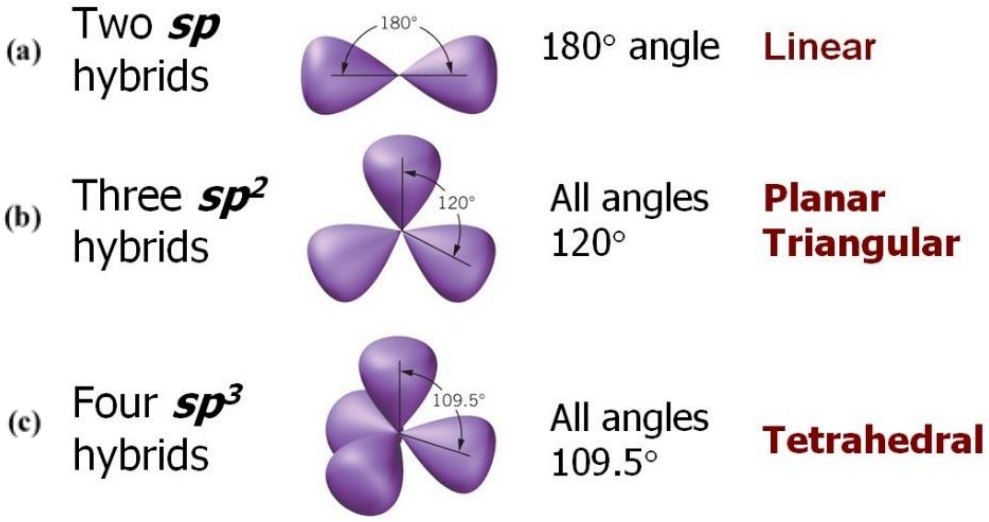

Figure 1.5 Schematic representation of the hybridizations for the carbon atom: (a) hybridization sp, (b) hybridization sp^2, and (c) hybridization sp^3. [22, 23]

Figure 1.5 shows the three hybridizations that the carbon atom can take: sp, sp^2, and sp^3. The "sp" hybridization involves mixing an "s" orbital with a "p," forming two new hybrid orbitals that are arranged at an angle of 180^0 as shown in Figure 1.5a. When carbon is hybridized in the

sp^2 form, an "s" orbital is combined with two other "p" orbitals, forming three orbitals oriented in the same geometric plane with an angle of 120^0 to each other, as shown in Figure 1.5b. The third type of hybridization made by carbon is called sp^3 (Figure 1.6 contains a complete description about carbon hybridization), the result of mixing an "s" orbital with three "p" orbitals, generating four sp^3 hybrid orbitals. These hybrid orbitals are oriented in a tetragonal way and with an angle of 109.5^0 to each other, as shown in Figure 1.5c. [23] These three hybridizations are responsible for the different allotropic forms of carbon found in nature, as shown in Figure 1.4. The difference in properties between such forms is related to how the atoms are arranged.

The most well-known allotropic forms of carbon are graphite, diamond, fullerene, nanotube, and graphene (Figure 1.4). Under normal conditions of pressure and temperature, carbon takes the form of graphite, whose crystalline structure can be understood as a stack of sheets in which each atom is joined to the other three in a network of hexagonal cells (Figure 1.4b). In this state, three electrons are found in hybrid sp^2 orbitals and the fourth in a "p" orbital. Due to the delocalization of electrons along with the interaction between "p" orbitals, graphite considers an excellent electrical conductor. In addition, as the different layers of this material are united by relatively weak forces (Van der Waals interaction), the ability of one layer to slide over the other is observed, a property that makes graphite a good lubricant. [24] Under high pressures, the carbon takes the form of a diamond, where each atom is joined to four others in the directions of a regular tetrahedron through sp^3 orbitals, as shown in Figure 1.4a. The diamond has the same face-centered cubic structure found in silicon and germanium and, due to the resistance of the carbon-carbon chemical bond, it is together with cubic boron nitride, the hardest substance known in nature. [25] Fullerene structures can be thought of as cages or regular polyhedra formed by the combination of carbon atoms arranged in pentagons and hexagons through sp^2 hybridization (Figure 1.4d).

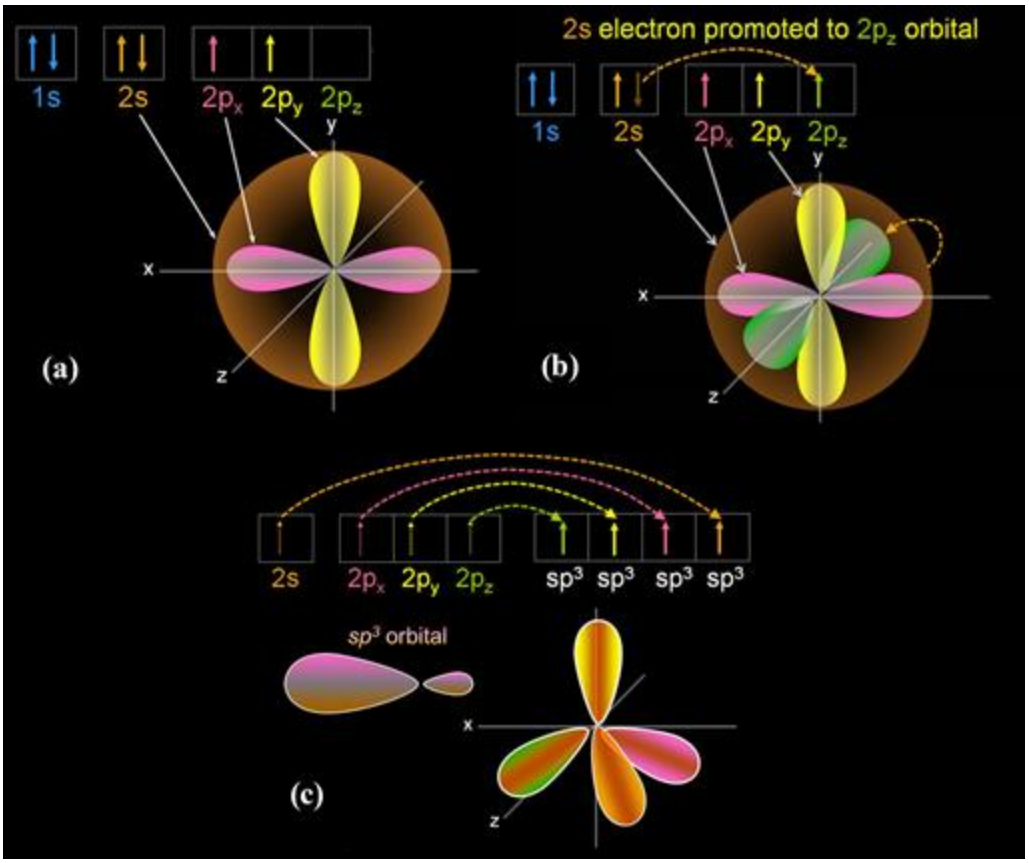

Figure 1.6 Carbon hybridization. (a) The ground state of carbon. The 1s electron clouds are not shown here since those are small and tightly linked to the nucleus, so they do not form bonds. Two paired spherical 2s electrons (orange sphere) are symbolized with up and down arrows [↑↓]. Additionally, it contains two unpaired $2p_x$ and $2p_y$, p-orbital electrons aligned on the x-y axes. When an atom comes closer to a carbon atom, one of the 2s-orbital electrons gets pulled into a high-energy orbital which is $2p_z$, as shown in Figure 1.6b. (b) The excited state of carbon. The orange-dotted arrow represents the transition of an electron from 2s-orbital to 2pz high energy orbital. The orange sphere is still present because there is one electron in the 2s-orbital. (c) Hybridized state of carbon. Four electrons in the 2s, $2p_x$, $2p_y$, and $2p_z$ blend together to form sp^3 hybridized orbitals, which have the same shape as shown in Figure 1.6c (the left image). Since there are one "s" orbital and three "p" orbitals in the configuration, it is called sp^3. [26]

Graphene corresponds to a single sheet of graphite, and its structure is composed of sp^2 hybridized carbon atoms connected and arranged in a two-dimensional lattice. Carbon nano-foams (Figure 1.7) are currently considered the sixth allotropic form of carbon. They were discovered in 2004 by a team of physicists [27] from Greece, Australia, and Russia led by Andrei V. Rode. This allotrope consists of clusters of carbon interconnected at random with average diameters between 6 and 9

nanometers, arranged in a web-shaped structure. In addition to having the least density ever reported for a solid, it was observed that this new material could exhibit ferromagnetic and strong paramagnetic properties at room temperature. [27-29]

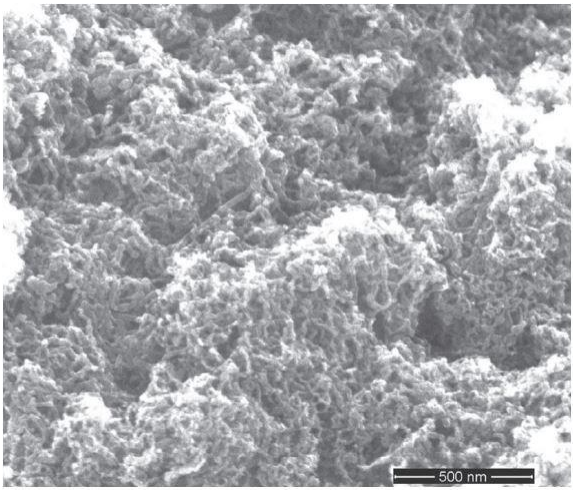

Figure 1.7 A SEM image (taken at 12,000X magnification) of a carbon nano-foam produced by the Pulsed laser deposition (PLD) method. [30]

1.2.3 Flatland: The Romance of Two Dimensions

The turning point in two-dimensional crystals occurred in 2004 when it was possible to experimentally separate one layer of graphite with scotch tape and apply it to a silicon substrate. [31] Thus, a two-dimensional carbon crystal, graphene, was formed with unique physical properties, which became stable due to the slight undulation of its surface. The theoretical description of the band structure of graphene was created in 1947 by P. R. Wallace in his work focused on the properties of graphite, [32] which later became the basis for the description of the properties of carbon nanotubes and fullerenes. Although graphene was previously considered impossible, atomically thin fragments of reduced graphene oxide, considered graphene monolayers, were produced even before its popular discovery in 2004. [33] However, the exfoliation method failed to produce stable graphite layers less than 20 nm thick before 2004. [34]

The carbon atoms in the graphene layer are arranged in a regular structure of hexagons and bound by a strong covalent bond, which causes its high flexibility and strength. Since then, both experimental and theoretical research has been widely conducted on graphene due to its unique chemical and physical characteristics. Hence, promising a variety of applications in nanophotonics, [35-37] nano-electronics (such as high-frequency electronic devices, gas sensors, stretchable transparent electrodes, and flexible electrochemical capacitors), [38-44] optoelectronics as shown in Figure 1.8, [45, 46] water filtration and desalination. [47-50]

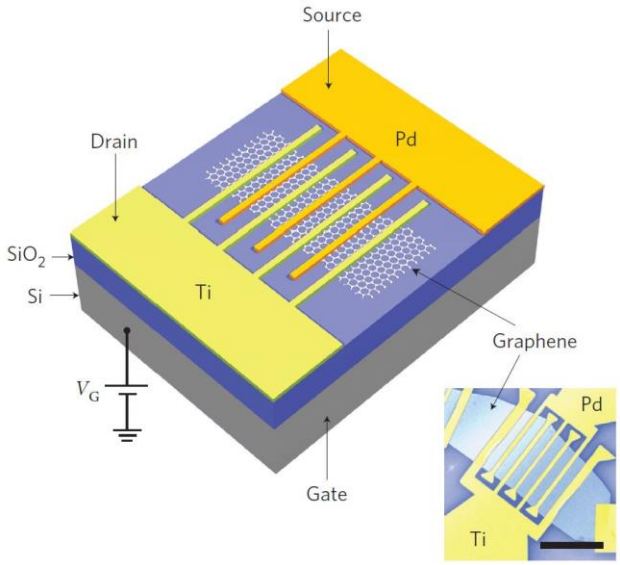

Figure 1.8 Metal–graphene–metal (MGM) photodetector. Top left: 3-D schematic of the device. Bottom right: scanning electron micrograph of the same device. The device structure is similar to typical metal–semiconductor–metal (MSM) detectors, but they have replaced the semiconductor layer with an exfoliated bi-layer graphene, which acts as the device's active layer. (Scale bar, 5 mm). [51]

For such device applications, desirable features of graphene include high optical transparency (97.7%), [52, 53], extraordinarily high carrier mobility (~200,000 $cm^2 V^{-1} s^{-1}$), [54] high surface area (2630 m^2/g), [55] extremely high mechanical strength (~1 TPa), [56] quantum Hall effect (both integer quantum Hall effect-IQHE and fractional quantum Hall effect-FQHE), [57-59] ambipolar electric field effect [31, 41] and high mechanical strength. [60] Additionally,

the high mobility of the graphene charge carriers makes it possible to observe quantum phenomena even at room temperature. It is therefore clear that research into new graphene-based materials and their properties is an integral part of technology development and can very often lead to surprising results. In 2010, the Nobel Prize in Physics was awarded to Andre Geim and Kostya Novoselov “for groundbreaking experiments regarding the 2-D material graphene".

The performance of current modern technologies depends mainly on the number of transistors located in a particular area and their quality. According to the so-called Moore's Law, this number doubles every 18 months while maintaining the same price. [61] Although various influences, such as power consumption, can be included in the definition, the main goal is to reduce the size of the transistors. However, this miniaturization is not possible indefinitely. At distances of a few nanometers, when a current is passed, the quantum effects prevent the proper functioning of the transistors. In the extreme case, the size of the transistor is limited by the size of the atom. Technological demands for the production of small transistors are very high because even minor inaccuracies in production or asymmetry of material have a significant influence on the behavior of manufactured devices in the case of the quantum world. If Moore's Law is to remain in force, then research into the properties of new materials in the field of nanotechnology is essential. Graphene is an ideal object for investigating these properties.

1.3 Motivation

The easiest way to obtain atomically thin monolayer and few-layer graphene is mechanical exfoliation using scotch tape, first demonstrated by A.K. Geim and K. Novoselov in 2004. [31] However, it produces layers with a maximum size of several tens of micrometers which is not suitable for large-scale device applications. Later, various fabrication methods were developed by scientists to produce graphene with specific properties for specific tasks. These includes

exfoliation: {mechanical cleavage/ wedge-based method, [62] graphite oxide reduction, [63, 64] shear exfoliation, [65] liquid-phase exfoliation, [66, 67] sonication-assisted solvent interface trapping, [68] electrochemical exfoliation [69]}, hydrothermal self-assembly, [70] Epitaxy: {metal-catalyzed (Ru, Ir, Ni, Co, Sn and Cu) chemical vapor deposition (CVD), [1, 44, 71-77] epitaxial growth on crystalline surfaces such as silicon carbide (SiC), [78-81] sodium ethoxide pyrolysis [82]}, nanotube slicing, [83, 84] the Langmuir-Blodgett method, [85-87] carbon dioxide reduction, [88] spin coating, [89] supersonic spray, [90] intercalation, [91-93] pulsed laser irradiation, [41, 94] microwave-assisted oxidation [95-98] and ion implantation. [99, 100]

However, the widely used method in laboratories and the industry to mass-produce large-area high-quality graphene is the Cu-catalyzed CVD method. In 2009, Xuesong Li et al. [74] first introduced the well-known Cu-catalyzed conversion of hydrocarbon precursors into large-area graphene films on Cu foils. This method is comparatively advantageous than other available methods because it can synthesize mono-layered, [74, 101-103] large area, [104-107] high crystalline [108-110], and high mobility [111-113] graphene films. Many efforts have been taken to improve this method recently, and it has been led to develop much controllable fabrication methods which allow scientists to control the domain shape and size, [109, 114] domain orientation, [115, 116] growth rate, [117] layer count (monolayer or bilayer), [109, 118] nucleation density, [1, 119, 120], etc.

In order to synthesize high-efficiency devices, it is vital to maintain high crystalline quality in graphene films during the growth process. However, the CVD-grown graphene is generally polycrystalline with many grain boundaries. This disrupts the electron transport [121-123] of the material, and the biggest challenge is to control the early stages of graphene nucleation and ultimately to create a larger area of highly/ monocrystalline graphene. One possible solution is to

let nucleation sites form far away from each other and let the graphene grow under strictly controlled conditions. Hence, the main idea of this work is focused on improving the production of highly/mono-crystalline graphene layers by the method of low-pressure chemical vapor deposition (LPCVD).

2 GRAPHENE THEORY

2.1 Physics of graphene

In this section, the crystal structure of monolayer graphene is first described, and then the derivation of wave function using the tight-binding model and effective mass approximation. Furthermore, since this wave function is a solution of the Dirac equation, it gives rise to a remarkable conduction phenomenon called the Klein-tunneling effect. [124-127] In addition, the wave function of two-layer graphene has been derived from the same consideration, but it also shows a peculiar tunneling effect even if it is not a Dirac electron (Dirac-cone) with zero mass.

2.1.1 Electronic state of monolayer graphene

2.1.1.1 Crystal lattice and electronic energy dispersion relationship of single-layer graphene

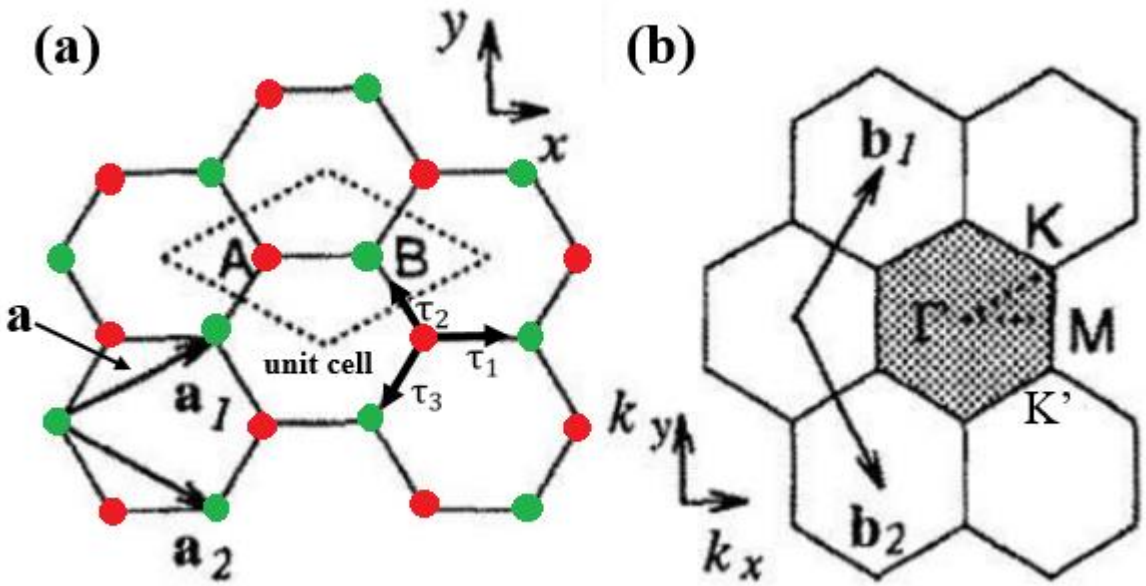

Figure 2.1 (a) Honeycomb structure of graphene in real space. The a_1 & a_2 vectors and two non-equivalent carbon atoms (A and B atoms), which are contained in a rhombus-shaped unit cell, define the Bravais network. (b) Graphene's first Brillouin Zone (FBZ) (shaded area) in the reciprocal lattice formed from the two atom Bravais lattice. Γ is the center of the FBZ, and the K and K' are on the corners while M represents the middle point between K and K.' The Dirac cones meet at the K and K' points. [128]

As shown in Figure 2.1a, graphene is composed of carbon atoms laid on a honeycomb lattice. A carbon atom has a total of four valence electrons, consisting of one 2s orbital and three 2p orbitals ($2p_x$, $2p_y$, and $2p_z$). Three of these orbitals, 2s, $2p_x$, and $2p_y$, constitute the sp^2 hybridized orbitals (Figure 2.2a), each of which forms a bond with a neighboring carbon atom.

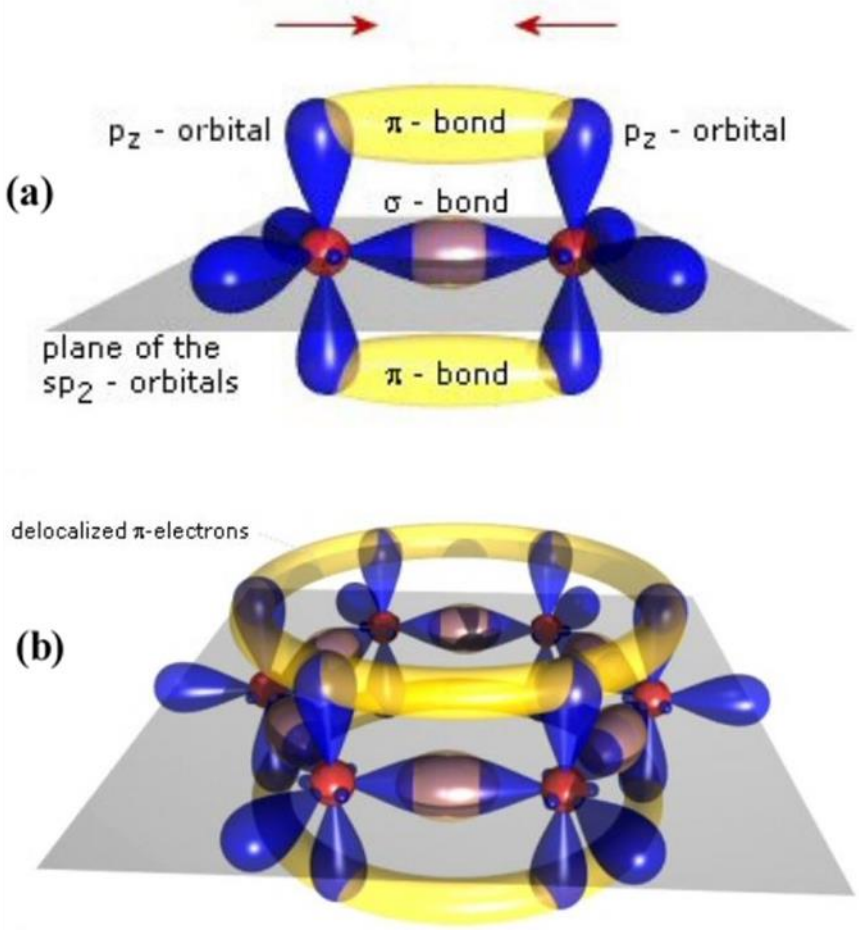

Figure 2.2 (a) Bonding arrangement between two carbon atoms in graphene. The sp^2 hybridized orbitals form the σ-bonds, which are strong and contribute to the hexagonal shape of graphene, resulting in a super-strong material. This bond lies on the plane of sp^2-orbitals. The p_z electrons contribute to form weak and delocalized π-bonds, responsible for the conduction of graphene and other carbon allotropes. (b) honeycomb-like structure, the building block of all carbon allotropes which contains delocalized π-electrons. [129, 130]

They are oriented such that the angles between each other in the plane are 120^0, resulting in a honeycomb-like structure (hexagonal) which is the reason behind these materials' incredible

strength. These orbitals, which contribute to the σ-bond, are strongly localized between energetically deep carbon atoms and do not appear in the vicinity of the Fermi energy. What appears in the vicinity of the Fermi energy is a π-bond, an electronic state created by the coupling of p_z orbitals. Hence, σ-bonds cannot contribute to the electrical conductivity. The π-bonds have formed purely by overlapping p_z orbitals on each carbon atom, as shown in Figure 2.2 since the $2p_z$ orbitals exist perpendicular to the sp^2 plane and have different symmetries in space. This makes π-orbitals spatially delocalized and hence, contributing to the conduction of carbon allotropes. Contrarily, an undoped carbon material (diamond has no π-electrons, sp^3-bonding, and has a large >5eV band gap) shows insulating properties in the absence of a partially filled π-orbital. [129]

As shown in Figure 2.1a, the unit vectors of graphene have two geometrically inequivalent carbon atoms (one of which alone cannot make a Bravais lattice). [131] These atoms are called A (red) & B (green) atoms, and the triangular sub-lattices consisting of each atom are called A and B sub-lattices. The reason why graphene has different properties than other two-dimensional materials can be described as the inclusion of different atoms in the unit cell due to this hexagonal lattice.

Let us define the fundamental/primitive lattice vectors in real space, as shown in Figure 2.1a. [132]

$$a_1 = a\left(\frac{\sqrt{3}}{2}, \frac{1}{2}\right),\ a_2 = a\left(\frac{\sqrt{3}}{2}, -\frac{1}{2}\right) \qquad (2.1)$$

Where "a" is the length of the fundamental lattice vector, a = |a1| = |a2| = 1.42 x $\sqrt{3}$ = 2.46 Å and the distance between the carbon atoms is $a_{C-C} = 1.42$ Å. The unit cell is a rhombus made up of a_1 and a_2.

The corresponding inverse (reciprocal) lattice vector is, [132, 133]

$$b_1 = \frac{2\pi}{a}\left(\frac{1}{\sqrt{3}}, 1\right), b_2 = \frac{2\pi}{a}\left(\frac{1}{\sqrt{3}}, -1\right) \quad (2.2)$$

The Brillouin zone (BZ) is similarly a rhombus formed by b_1 and b_2, but it is taken as a hexagon (Figure 2.1b) to consider the symmetry of the original crystal. The vertices of this Brillouin zone are called K and K', and their wavenumbers are given by,

$$K = \frac{\pi}{a}\left(1, \frac{1}{\sqrt{3}}\right), K' = \frac{\pi}{a}\left(1, -\frac{1}{\sqrt{3}}\right) \quad (2.3)$$

Now, since the electronic state related to the π-bond is $2p_z$ of A and B atoms, respectively, the electronic state in the crystal is the representation of these atoms. [132, 133]

$$\Psi(k, r) = c_A\Phi_A(k, r) + c_B\Phi_B(k, r) \quad (2.4)$$

$$\Phi_i(k, r) = \frac{1}{\sqrt{N}}\sum_{R_i}^{N} e^{ik.R_i}\,\varphi(r - R_i) \quad (2.5)$$

where, φ(r) is the wave function of the $2p_z$ orbital of a carbon atom, [134] $R_i(i = A, B)$ is the position vector of the A and B atoms, and N is the number of unit cells (but since the A and B atoms are not connected by translational operator, they must be treated separately). [135] $\Phi(k, r)$ is a Bloch orbit that satisfies Bloch's theorem. [136] Now, if $|R_i\rangle = \varphi(r - R_i)$ is applied to A or B atom, it can be expressed as,

$$|\Psi_i\rangle = \sum_{R_i} d_i\,(R_i)|R_i\rangle \tag{2.6}$$

$$d_i(R_i) = \frac{1}{\sqrt{N}}\, c_i e^{ik.R_i} \tag{2.7}$$

Where i = A, B.

Multiply the Schrodinger equation by $\langle R_i|$ from the left,

$$\sum_{R_i'} d_i\,(R_i')\langle R_i|H|R_i'\rangle = E \sum_{R_i'} d_i\,(R_i')\langle R_i|R_i'\rangle \tag{2.8}$$

Assume, $\langle R_i|R_i'\rangle = \delta_{R_i,R_i'}$ and there is no overlap integral between different atoms. [137] Furthermore, if the overlap integral (hopping integral) is $t(R_i, R_i') = -\langle R_i|H|R_i'\rangle$, then, the relational expression of the tight binding model can be obtained.

$$-\sum_{R_i} t(R_i, R_i')d_i(R_i') = E d_i(R_i) \tag{2.9}$$

This can be applied to both A and B atoms. Here, if we consider only the nearest hopping integral factor γ_0 (where γ_0 is an experimentally available parameter, $\gamma_0 \sim 3eV$), then

$$-\gamma_0 \sum_{l=1}^{3} d_B(\boldsymbol{R}_A + \boldsymbol{\tau}_l) = E d_B(\boldsymbol{R}_A), -\gamma_0 \sum_{l=1}^{3} d_A(\boldsymbol{R}_B - \boldsymbol{\tau}_l) = E d_A(\boldsymbol{R}_B) \tag{2.10}$$

From equation (2.7), we can write,

$$-\gamma_0 \begin{pmatrix} 0 & f(\boldsymbol{k}) \\ f^*(\boldsymbol{k}) & 0 \end{pmatrix} \begin{pmatrix} c_A \\ c_B \end{pmatrix} = E \begin{pmatrix} c_A \\ c_B \end{pmatrix}, f(k) = \sum_{l=1}^{3} e^{ik.\tau_l} \tag{2.11}$$

The energy eigenvalues are obtained by diagonalizing the matrix shown in the equation (2.11).

$$E(k) = \pm\gamma_0 |f(k)| = \sqrt{1 + 4\cos\frac{\sqrt{3}k_x a}{2}\cos\frac{k_y a}{2} + 4cos^2\frac{k_y a}{2}} \tag{2.12}$$

This is plotted in wavenumber space (k-space), as shown in Figure 2.2a. It can be seen from Figure 2.3b that the top and bottom bands touch each other symmetrically with E = 0 at points K and K' without any gap. This tangent point is called the Dirac point. Furthermore, since each carbon atom has an average of one π-electron, the lower band is wholly packed with electrons in the ground state, while the upper band is empty. Therefore, it can be seen that the Fermi energy is located precisely at the tangent point of this band (E = 0).

Since the experimentally accessible energy region is about 1 eV near the Dirac point, the electronic properties of graphene are almost determined by the electronic structure around the K point. There are also two non-equivalent points (K and K' points) reflecting the two sub-lattices of graphene (these degrees of freedom are called valleys). Hereafter, let the valley index be $\xi = \pm 1$ (K point corresponds to $\xi = 1$ and K' point corresponds to $\xi = -1$) in order to distinguish these two differences.

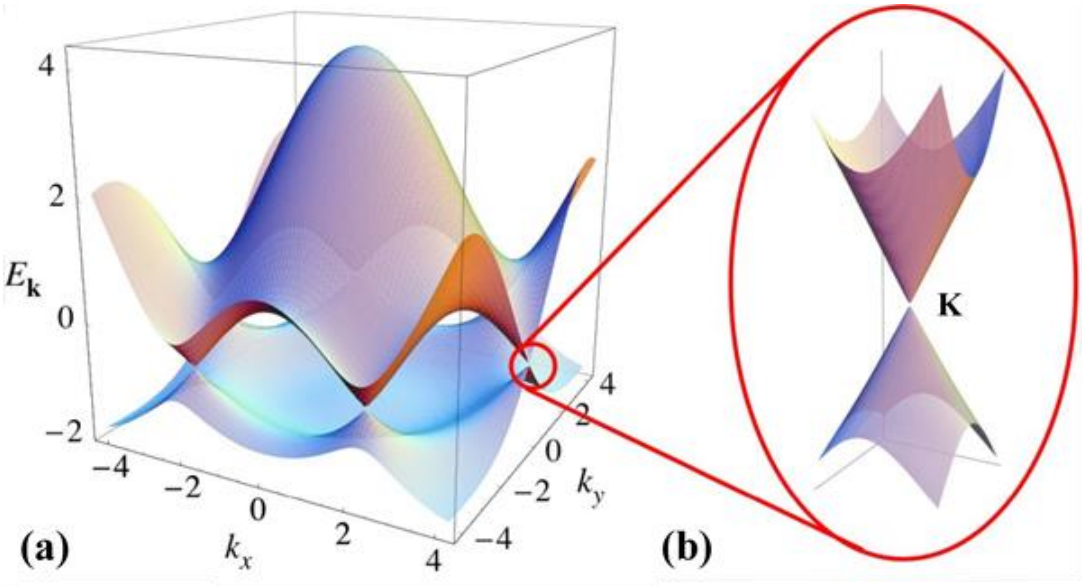

Figure 2.3 (a) The π and π bands linearly intersect at the edge of the Brillouin zone (K, K' points in Figure 2.1b). [133] Fermi energy is located precisely at this intersection which is known as Dirac point where E=0. (b) Conical, linear dispersion (Dirac cone) near the K and K' points (Fermi level). [138]*

Next, let us calculate the electronic state near K. This can be obtained by expanding equation (2.11) around the K point. First, if the momentum measured from the K_ξ point is defined as $p = \hbar k - \hbar K_\xi$, it can be expanded to ${}^{pa}/_{\hbar} \ll 1$ when $f(k)$ is given.

$$f(k) \approx -\frac{\sqrt{3}a}{2\hbar}\left(\xi p_x - i p_y\right) \tag{2.13}$$

Thus, we can write the effective Hamiltonian matrix as,

$$H = \begin{pmatrix} \epsilon_A & v\pi^\dagger \\ v\pi & \epsilon_B \end{pmatrix} \tag{2.14}$$

where $\pi = \xi p_x + i p_y$ and $v = \sqrt{3} a \gamma_0 / 2\hbar$. v is the speed of an electron, which is $v \sim 1 \times 10^6 \, m/s$ regardless of its momentum, and is about 1/300 times the speed of light. It can be seen that when $\epsilon_A = \epsilon_B = 0$, E becomes linear dispersion (Figure 2.3b),

$$E = \pm v|\boldsymbol{p}| \tag{2.15}$$

2.1.1.2 The wave function near K point

Using the tight-binding model, the relationship between the amplitudes of A and B atoms (2.11) has been derived and further expanded near the K point to derive the effective Hamiltonian. However, since the positions $\boldsymbol{R}_A$ and $\boldsymbol{R}_B$ of each carbon atom is discontinuous c_A and c_B and D in equation (2.11) is not inherently continuous quantities. For this reason, it is necessary to evaluate the amplitude around the K point using the effective-mass approximation using an envelope electron wave function. [139, 140]

However, this result shows that the envelope function can be defined as a continuous function by treating $\boldsymbol{p}$ as a differential operator for the effective Hamiltonian near the K point shown in equation (2.11). That is, when $\epsilon_A = \epsilon_B = 0$, the wavefunction near the K point can be obtained by solving,

$$v \begin{pmatrix} 0 & \hat{p}_x - i\hat{p}_y \\ \hat{p}_x + i\hat{p}_y & 0 \end{pmatrix} \begin{pmatrix} F_A^K(\boldsymbol{k}) \\ F_B^K(\boldsymbol{k}) \end{pmatrix} = E \begin{pmatrix} F_A^K(\boldsymbol{k}) \\ F_B^K(\boldsymbol{k}) \end{pmatrix} \tag{2.16}$$

Here, the wave functions of A and B atoms near the K point are replaced with $\boldsymbol{F}(\boldsymbol{r})^{\boldsymbol{K}} = (F_A^K, F_B^K)$.

This effective mass equation can be written as,

$$v\left(\sigma_x \hat{p}_x + \sigma_y \hat{p}_y\right)\boldsymbol{F^K}(\boldsymbol{r}) = E\boldsymbol{F^K}(\boldsymbol{r}) \tag{2.17}$$

using Pauli's spin matrix,

$$\sigma_x = \begin{pmatrix} 0 & 1 \\ 1 & 0 \end{pmatrix}, \sigma_y = \begin{pmatrix} 0 & -i \\ i & 0 \end{pmatrix} \tag{2.18}$$

The electronic state around the K' point can be obtained in the same way by making p_x into $-p_x$ from Equation (2.13).

$$-v\left(\sigma_x \hat{p}_x + \sigma_y \hat{p}_y\right)\boldsymbol{F^{K'}}(\boldsymbol{r}) = E\boldsymbol{F^{K'}}(\boldsymbol{r}) \tag{2.19}$$

Here, it is confirmed that that the electrons of graphene are Dirac electrons, described by the Dirac equation. The Dirac equation incorporates relativistic effects into the Schrödinger equation because the Schrödinger equation only describes particles in the non-relativistic limit. Among those, the Weyl equation effectively describes the massless Dirac fermion with ½-spin in relativistic quantum mechanics, which is denoted by,

$$i\hbar\frac{\partial}{\partial t}\psi_L = c\boldsymbol{\sigma}.\boldsymbol{p}\psi_L \, , i\hbar\frac{\partial}{\partial t}\psi_R = -c\boldsymbol{\sigma}.\boldsymbol{p}\psi_R \tag{2.20}$$

when the four-component wave function is divided into two components as $\psi = (\psi_L, \psi_R)$. [141-145] Here, c corresponds to the speed of light, ψ_L and ψ_R correspond to the left-handed and right-handed states. The energy of the Weyl equation is written as,

$$E = \pm cp \tag{2.21}$$

Comparing this with the electrons of single-layer graphene around the K point, we can see that the speed of light c and the Fermi speed v correspond and are expressed by the same equation. The components of the wave function, in this case, correspond to the spin, but in the case of graphene, they only represent the probability amplitudes of the two components, A and B, and not the true spin of the electron (this is called pseudo-spin). It can also be seen that the relationship between the K point and the K' point corresponds to right- and left-handedness (this is called chirality). Thus, graphene electrons are electrons following the Dirac equation near the Fermi energy, so graphene has peculiar properties. The shape of the wave function will be determined explicitly in the following. The solution to equation (2.16) is obtained by assuming a plane wave $\boldsymbol{F}(\boldsymbol{r}) \propto exp(i\boldsymbol{k}.\boldsymbol{r})$ (the origin of the wave vector at this time is K).

$$\boldsymbol{F^K}(\boldsymbol{r}) = \frac{1}{\sqrt{2}}\begin{pmatrix} 1 \\ se^{i\phi_k} \end{pmatrix} e^{i\boldsymbol{k}.\boldsymbol{r}} \tag{2.22}$$

where $s = \pm 1$ and $\phi_k = \tan^{-1}\left(k_y / k_x\right)$.

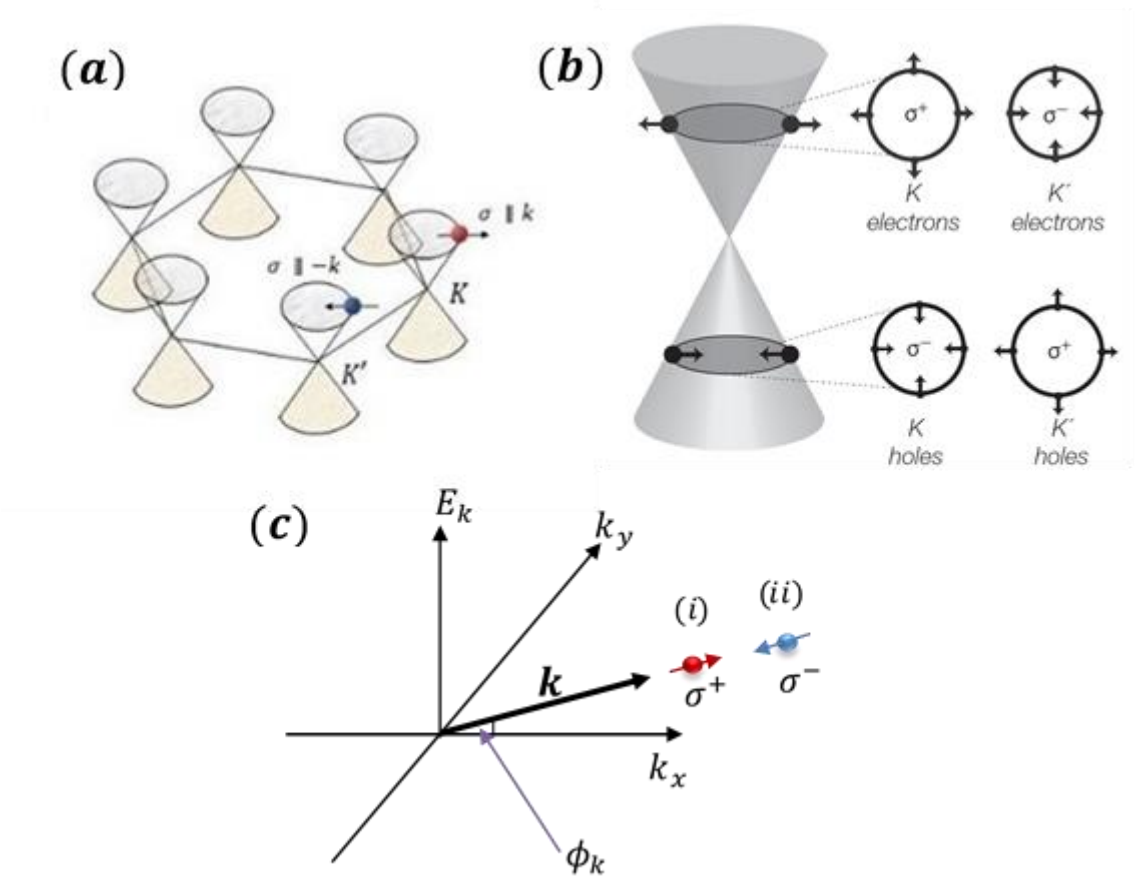

Figure 2.4 The band structure of single-layer graphene, which is related to Figure 2.1 and Figure 2.3 (a) an illustration of six valleys of non-equivalent types of K and K', known as Dirac cones. (b) Top view of the K and K' points/valleys (Dirac cone), which represent the pseudo-spin up (σ^+) and down (σ^-) for electrons and holes. The pseudo-spin and the direction of motion are related to each other (c) Schematic of pseudo-spin at K and K' points in the k-space. There are two configurations as follows, (i) indicates the orientation of the pseudo-spin σ in the conduction band (for $s > 0$), which is σ^+(red) parallel to the wave vector ($\boldsymbol{k}$). (ii) Indicates the orientation of the pseudo-spin σ in the valence band (for $s < 0$), which is σ^-(blue) anti-parallel to the wave vector ($\boldsymbol{k}$). [146-149]

Using this wave function and equation (2.18), the expected value of the pseudo-spin is obtained as,

$$\langle \boldsymbol{\sigma} \rangle = \big(\langle \sigma_x \rangle, \langle \sigma_y \rangle\big) = s(\cos\phi_k\,, \sin\phi_k) \tag{2.23}$$

Moreover, the direction of the pseudo-spin is parallel to the wave vector for the conduction band $s > 0$ and anti-parallel to the wave vector for the valence band $s < 0$, as shown in Figure 2.4.

2.1.2 Electronic state of bilayer graphene

Here, the most stable stacking is considered, the AB layer of graphene. In this stacking, the hexagons are stacked out of alignment, and the crystal structure is such that the B_1 atoms of the lower layer are located directly below the A_2 atoms of the upper layer. The distance between the layers is 3.35 Å. The basic lattice vector is the same as in monolayer graphene, but there are four atoms in the unit cell since A and B atoms are present in the upper and lower layers, respectively. For bilayer graphene, as shown in Figure 2.5, there is one in-plane nearest-neighbor hopping parameter [150] which is denoted by γ_0 and three interlayer parameters γ_1, γ_3 and γ_4. As already mentioned, the B_1 atom is located directly below the A_2 atom, and these electron orbitals are more strongly linked than the interactions between other layers (called "dimer" atoms). [132, 133, 151] For this reason, γ_1 is the most important interaction between the layers. It is known that the value of γ_1 is one order of magnitude smaller than γ_0 (where, $\gamma_0 = 3.033\ eV$) [128, 132, 133] in the plane, and experimentally, it is about $\gamma_1 \sim 0.3\ eV$. [132, 133] On the other hand, since there are no atoms directly above or below the A_1 and B_2 atoms, they are relatively weakly connected (called "non-dimer" atoms).

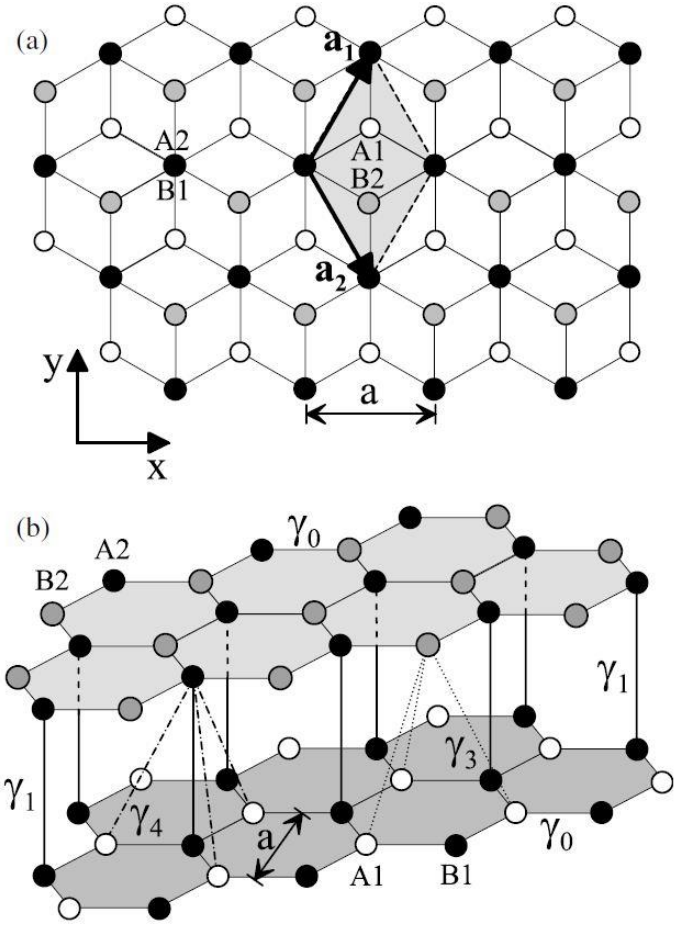

Figure 2.5 AB Crystal structure of the bi-layer graphene. (a) top/plan view of the crystal structure. On the top layer, A_2 and B_2 atoms are represented by black and gray dots, respectively. On the bottom layer, A_1 and B_1 atoms are represented by white and black dots. Electron orbitals of A_2 and B_1 atoms are more strongly linked than the interactions between other layers (called "dimer" atoms) because the B_1 atom is located directly below the A_2 atom (represented by the top-left black dot labeled as A_2B_1 . Contrarily, Electron orbitals of A_1 and B_2 atoms are relatively weakly connected (called "non-dimer" atoms) because there are no atoms directly above or below A_1 and B_2 atoms (represented by the top-right white and grey dots, which are labeled as A_1 and B_2 within the diamond shaped shaded area). (b) side view of the crystal structure. γ_0 is the in-plane nearest-neighbor hopping parameter. Here, three interlayer parameters are represented as γ_1, γ_3 and γ_4. The unit cell can be taken as the diamond shown in (a) and contains the upper B_2 and lower A_1 atoms. [132, 133, 138]

As in monolayer graphene, the Hamiltonian matrix in the tight-binding model is represented for bilayer graphene. Here, the hopping energy is defined as follows. [132, 133, 138]

$$H_b = \begin{pmatrix} \epsilon_{A_1} & -\gamma_0 f(k) & \gamma_4 f(k) & -\gamma_3 f^*(k) \\ -\gamma_0 f^*(k) & \epsilon_{B_1} & \gamma_1 & \gamma_4 f(k) \\ \gamma_4 f^*(k) & \gamma_1 & \epsilon_{A_2} & -\gamma_0 f(k) \\ -\gamma_3 f(k) & \gamma_4 f^*(k) & -\gamma_0 f^*(k) & \epsilon_{B_2} \end{pmatrix} \tag{2.24}$$

Where,

$$\gamma_0 = -\langle \phi_{A_1} | \mathcal{H} | \phi_{B_1} \rangle = -\langle \phi_{A_2} | \mathcal{H} | \phi_{B_2} \rangle \tag{2.25}$$

$$\gamma_1 = \langle \phi_{A_2} | \mathcal{H} | \phi_{B_1} \rangle \tag{2.26}$$

$$\gamma_3 = -\langle \phi_{A_1} | \mathcal{H} | \phi_{B_2} \rangle \tag{2.27}$$

$$\gamma_4 = \langle \phi_{A_1} | \mathcal{H} | \phi_{A_2} \rangle = \langle \phi_{B_1} | \mathcal{H} | \phi_{B_2} \rangle \tag{2.28}$$

The upper left and lower right 2×2 submatrices of H_b in equation (2.24) are in the same layer and correspond to equation (2.11) and equation (2.14). Both γ_3 and γ_4 are hopping with respect to non-dimer atoms, with the difference that γ_3 is hopping between non-dimer atoms and γ_4 is hopping between dimer and non-dimer atoms. As shown in the Figure 2.6, the dispersion relation of bilayer graphene (AB stack) can be obtained by diagonalizing this Hamiltonian H_b. The parameters used in the calculation are $\gamma_0 = 3.16\ eV$, $\gamma_1 = 0.381\ eV$, $\gamma_3 = 0.38\ eV$, $\gamma_4 = 0.14\ eV$, $\epsilon_{B_1} = \epsilon_{A_2} = 0.022\ eV$ and $\epsilon_{A_1} = \epsilon_{B_2} = 0\ eV$. Also, as in the case of monolayer graphene, the effective Hamiltonian around the K point can be derived by expanding the equation (2.24) around the K point. [132, 133] Note that the, $v_3 = \sqrt{3}a\,\gamma_3/2\hbar$ and $v_4 = \sqrt{3}a\,\gamma_4/2\hbar$.

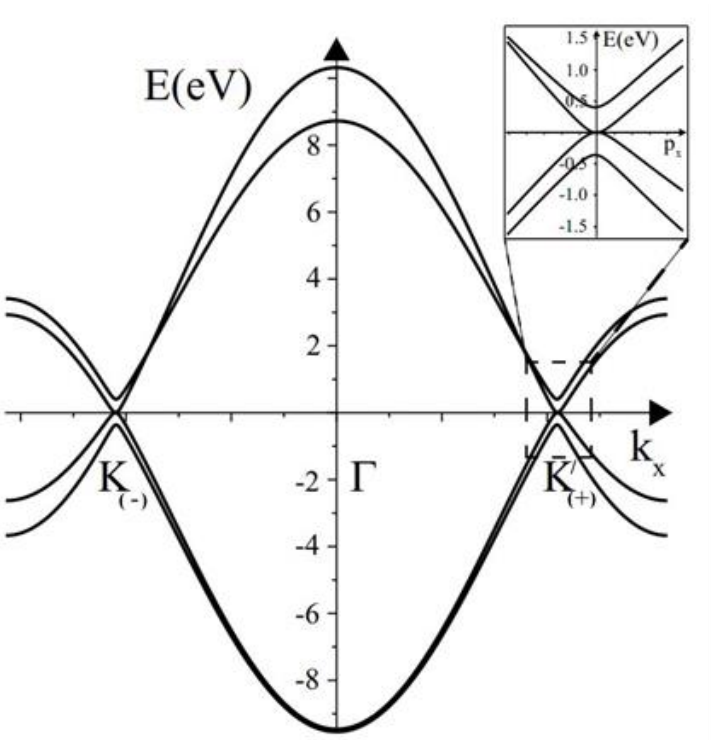

Figure 2.6 Low-energy bands and the dispersion relation for graphene bi-layers (AB stack) arising from 2pz orbitals. It has been plotted in the reciprocal space along the k_x direction. Γ is the center of the Brillouin zone (BZ)). The dispersion is no longer linear near the K point (around one of the inequivalent corners of the Brillouin zone (BZ)), and it turns out to be parabolic. In addition, at low energy, the parabolic band of the non-dimer atom near the Fermi surface is tangent at E= 0 (inset figure). Please note that the, $K_{(+)}$ and $K_{(-)}$ in the image represent K' and K in the text [132]. The plots of the dispersion relation were produced by diagonalizing the Hamiltonian H_b (equation (2.24)). [152]

$$H_b = \begin{pmatrix} \epsilon_{A_1} & v\pi^\dagger & -v_4\pi^\dagger & v_3\pi \\ v\pi & \epsilon_{B_1} & \gamma_1 & -v_4\pi^\dagger \\ -v_4\pi & \gamma_1 & \epsilon_{A_2} & v\pi^\dagger \\ v_3\pi^\dagger & -v_4\pi & v\pi & \epsilon_{B_2} \end{pmatrix} \tag{2.29}$$

So far, an effective Hamiltonian around the K point for bi-layer graphene has been created by considering four atoms contained in the unit cell, but only the non-dimer atoms are related to the low energy near the Fermi surface. Therefore, if the non-dimer atoms are extracted from this Hamiltonian on the basis of the non-dimer atoms and only γ_1 is left as an interlayer interaction, then a low energy two-band effective Hamiltonian (H_0) for bilayer graphene can be made. [132,

133, 138] Since there are four atoms in the unit cell, it contains four bands. As shown in the inset of Figure 2.6, there is a total of four bands since the unit cell contains four atoms. Two of them are parabolic bands that touch at E=0, and the remaining two bands are in the open position about $E \sim \pm \gamma_1$. So, in the vicinity of the Fermi energy of $|E| \ll \gamma_1$, we can use the effective Hamiltonian without the orbit of dimer atom. First, the wave function can be divided into two parts: the non-dimer atom part θ, which corresponds to the low energy, and the part χ, which has the dimer atom as an element.

$$\theta = \begin{pmatrix} \psi_{A_1} \\ \psi_{B_2} \end{pmatrix} \ , \ \chi = \begin{pmatrix} \psi_{A_2} \\ \psi_{B_1} \end{pmatrix} \tag{2.30}$$

The Schrodinger equation near the K point is expressed as,

$$\begin{pmatrix} h_\theta & u \\ u^\dagger & h_\chi \end{pmatrix} \begin{pmatrix} \theta \\ \chi \end{pmatrix} = E \begin{pmatrix} \theta \\ \chi \end{pmatrix} \tag{2.31}$$

By rearranging the equation (2.29). Here, [132, 133, 138]

$$h_\theta = \begin{pmatrix} \epsilon_{A_1} & v_3\pi \\ v_3\pi^\dagger & \epsilon_{B_2} \end{pmatrix}, h_\chi = \begin{pmatrix} \epsilon_{A_2} & \gamma_1 \\ \gamma_1 & \epsilon_{B_1} \end{pmatrix}, \tag{2.32}$$

$$u = \begin{pmatrix} -v_4\pi^\dagger & v\pi^\dagger \\ v\pi & -v_4\pi \end{pmatrix}, u^\dagger = \begin{pmatrix} -v_4\pi & v\pi^\dagger \\ v\pi & -v_4\pi^\dagger \end{pmatrix}$$

By solving two linear equations which resulted from the equation (2.31), we can find H_0. [132, 138])

$$H_0 = -\frac{1}{2m}\begin{pmatrix} 0 & (\pi^\dagger)^2 \\ (\pi)^2 & 0 \end{pmatrix} \tag{2.33}$$

Here, the effective mass $m = \frac{\gamma_1}{2v^2}$ Furthermore, this solution has four eigenstates, a plane wave and an evanescent wave.

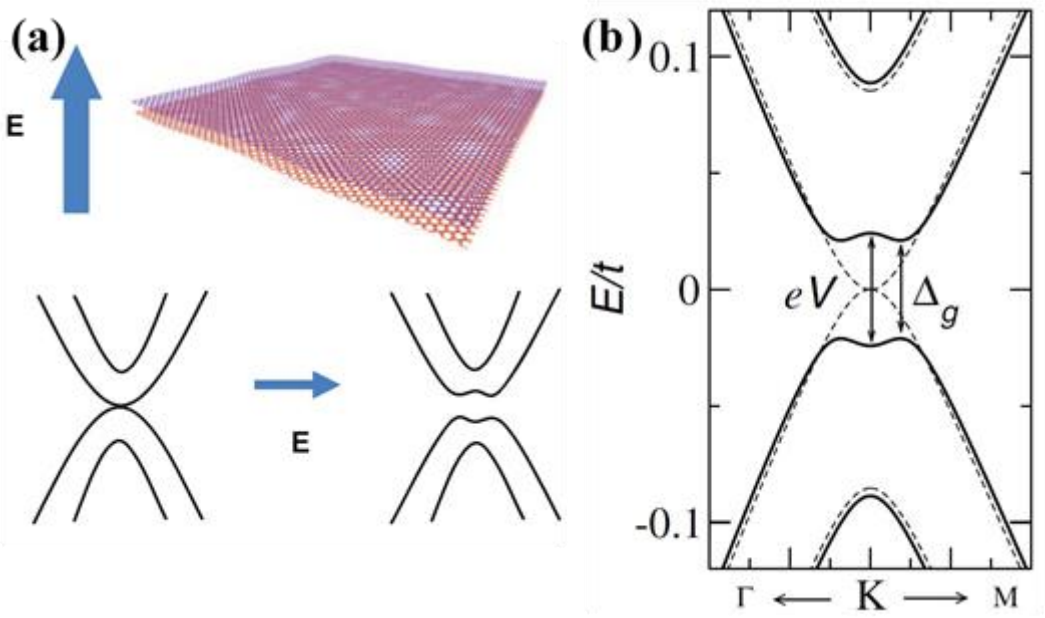

Figure 2.7 (a) Bottom-left: Low-energy band structure near the K-point in bilayer graphene. The parabola, which represents the E with an effective mass m, is tangent at E=0. (b) Same bilayer graphene sample under the influence of an external electric field/bias voltage $v_b = \triangle$. *The band gap is opened by two times the applied field,* $\triangle_g = 2\triangle$ *than the non-biased state, [153] when a perpendicular electrical displacement field is applied to bi-layer graphene, and this* $\triangle_g$ *is tunable. [154-156]*

$$\boldsymbol{F(r)} \propto e^{\pm i\boldsymbol{k}.\boldsymbol{r}}, e^{\pm \boldsymbol{k}.\boldsymbol{r}} \tag{2.34}$$

However, the basis atoms are A_1 and B_2. The energy formula (as shown in Figure 2.7) for bilayer graphene can be written as follows (for single-layer graphene, it was E= $\pm v|\boldsymbol{p}|$),

$$E = \pm \frac{1}{2m} |\boldsymbol{p}|^2 \tag{2.35}$$

Thus, the linear dispersion of monolayer graphene undergoes a significant change due to inter-layer interactions. Another important feature of the two-layered graphene is that it can be easily gapped by adding a vertical/perpendicular external energy change/biasing (Figure 2.7a) to the surface of the bi-layer graphene diagonal term of the Hamiltonian (2.36). This can be achieved by making the two layers non-equivalent. If an electric field $\triangle$ is applied perpendicular to the face of the bilayer graphene, then the Hamiltonian equation would be,

$$H_0 = -\frac{1}{2m} \begin{pmatrix} \triangle & (\pi^{\dagger})^2 \\ (\pi)^2 & -\triangle \end{pmatrix} \tag{2.36}$$

Then the energy equation (2.35) changes to equation (2.37) and opens a gap in size $\triangle_g =\ 2\ \triangle$ as shown in Figure 2.7b. [153]

$$E = \pm \sqrt{\left(\frac{p^2}{2m}\right)^2 + \triangle^2} \tag{2.37}$$

3 GRAPHENE SYNTHESIS METHODS

3.1 Overview

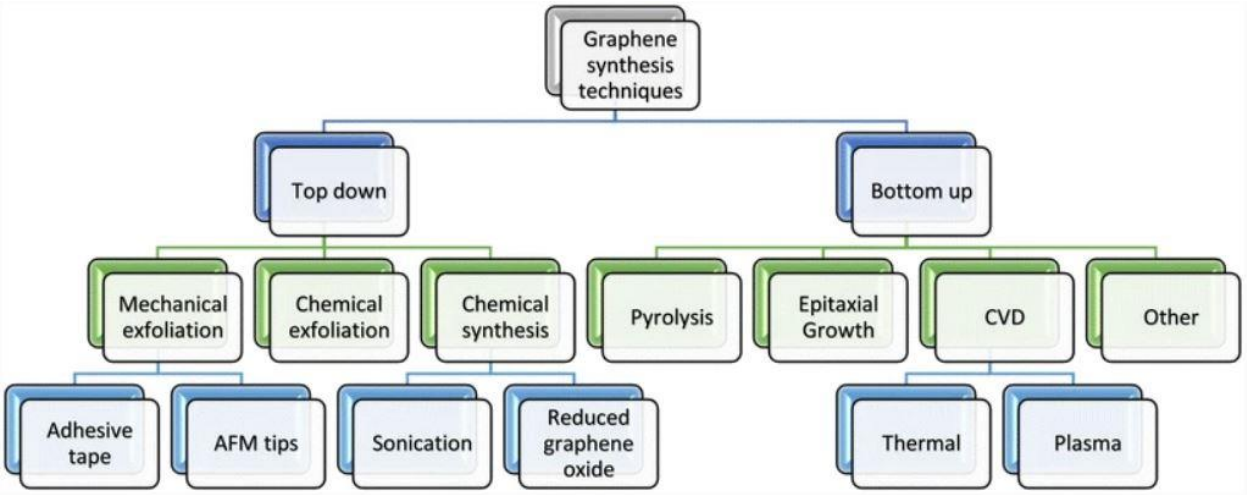

Figure 3.1 Flow chart of available graphene fabrication techniques. [157]

The growth of a 2D material consisting of a layer with atomic thickness is an extremely critical process to control that requires the search for growth methods (Figure 3.1) capable of preserving the structural characteristics and consequently the material's properties as the extension of the films produced increases. The experimental techniques for graphene synthesis can be grouped into two categories: (1) Top-down method (Figure 3.2b), where graphene is obtained from massive carbon-based materials such as graphite or graphite oxide. These methods are more suitable to industry because they allow a better quality, scalability, and reproducibility of the graphene grown. (2) Bottom-up method (Figure 3.2a) where graphene is grown on surfaces from carbon-containing precursor molecules, which decompose into carbon radicals and bind with the catalyst material of the decomposition reaction, which acts as a substrate or exploits the carbon directly present in the growth medium (Ni, Cu, Pt, Co, SiC, etc.). The techniques that we discussed in section 1.3, such as mechanical exfoliation and all chemical exfoliation techniques, including that of graphite oxide, nanotube slicing, etc. fall into the top-down category while the epitaxial

growth of graphene on silicon carbide crystals (SiC) and the CVD method fall into the bottom-up category (Figure 3.2).

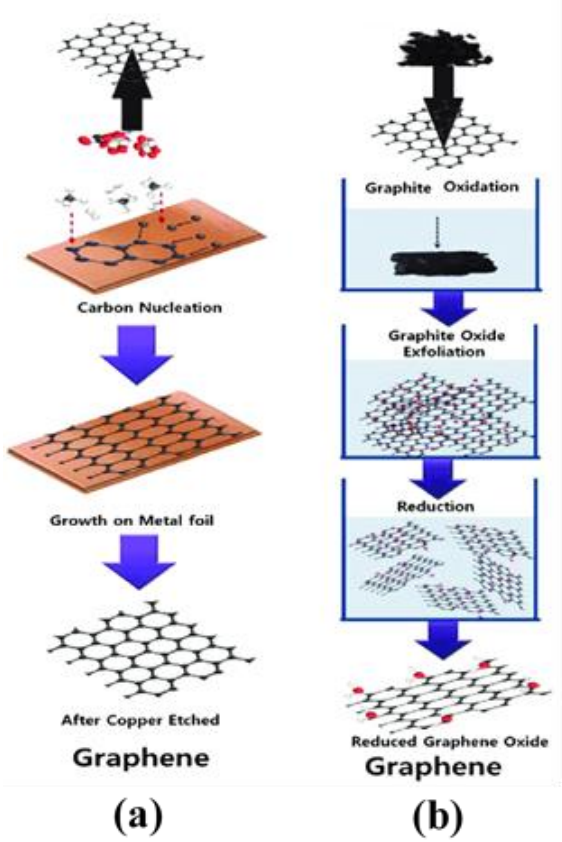

Figure 3.2 Schematic representation of (a) bottom-up and (b) top-down process of graphene synthesis. [158]

3.2 Exfoliation of graphite

3.2.1 Chemical exfoliation

3.2.1.1 Water and surfactant solution-based

The characteristics of a suitable solvent that can be used for the exfoliation of dispersed graphite powder are linked to its surface energy which must be compatible with that of graphene layers. [159] Since the surface energy of the water is higher than that of graphene layers, it is not

suitable for this method; even though water does not have a quite high boiling point and is not a source of toxicity for human beings, it is not a good candidate.

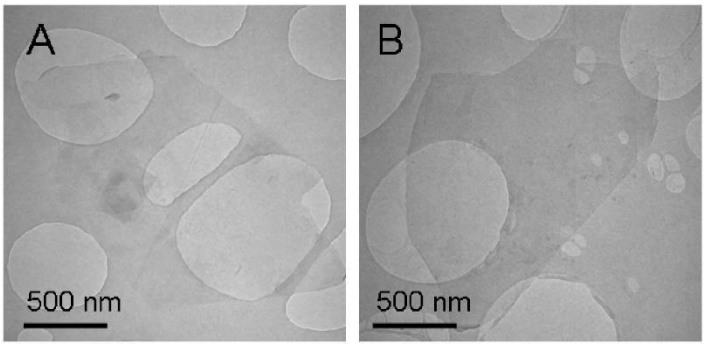

Figure 3.3 The TEM images of high crystalline graphene flakes prepared by water/surfactant method. (a) a monolayer graphene flake with square-shaped debris on the left, which contains fewer defects compared to the other exfoliation methods. (b) a bilayer graphene flake. The scale bar is 500 nm. [160]

A possible solution could be using aqueous solutions composed of surfactants, which lowers the surface tension of the water and makes possible the exfoliation of graphite layers. [160] The quality of the graphene crystals/layers is good, with little presence of defects or oxides, despite the low yield of single-layer graphene compared to the other solvent-based exfoliation methods. [66, 160-162]

3.2.1.2 Intercalation to produce graphite intercalation compounds (GICs)

This type of exfoliation is performed by inserting atomic or molecular species, known as intercalants, at the interface between graphene layers, forming the so-called graphite intercalation compounds due to the interaction between graphene layers and surfactants, as shown in Figure 3.4 and Figure 3.5 (bottom-right). [163, 164]

$$C + mX \rightarrow CX_m \tag{3.1}$$

where C represents carbon atoms, the ions X^{n+}or X^{n-}represent the intercalants that are inserted between graphene layers. [163] These compounds are characterized by a stoichiometric ratio (n) which is carbon atoms to intercalant atoms, and a staging index (m<<1), which corresponds to the number of graphene layers between two layers of intercalant as shown in Figure 3.4 and equation (3.1). [164] The process is shown in equation 3.1, analogous to the mechanism of lithium-ion batteries. GICs can exhibits a wide range of intrinsic electronic, physical and chemical properties, depending on the type of interlayer and its index. [165-171]

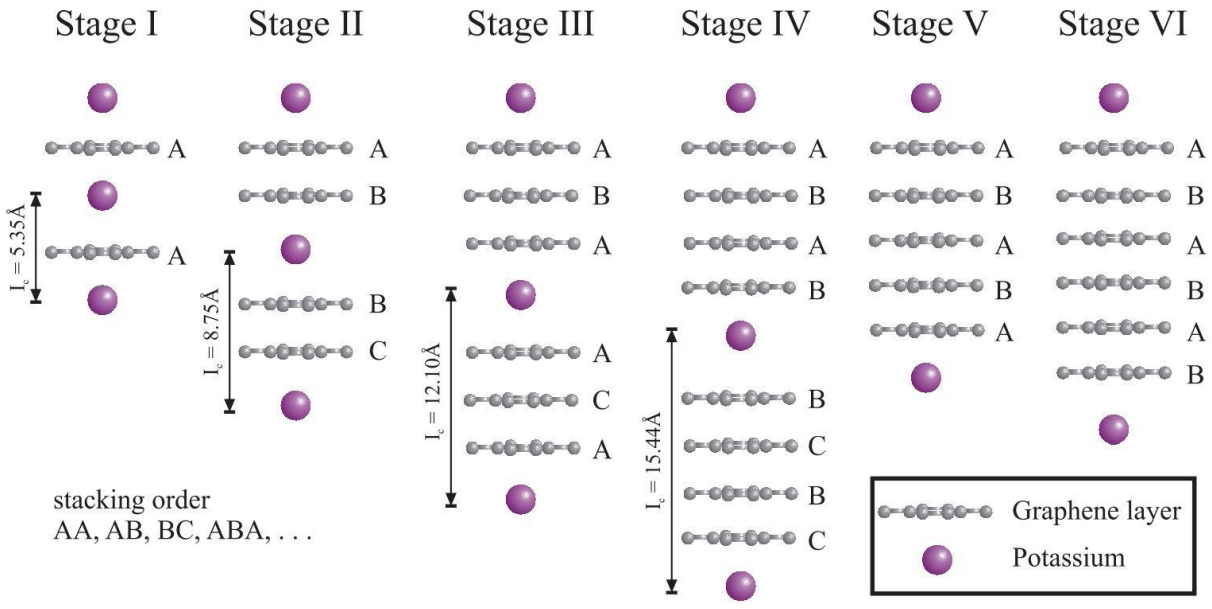

Figure 3.4 A step-by-step illustration of staging in GICs. Here, purple balls (Potassium) represent the intercalant layers, and gray hexagonal networks represent the graphene layers. [164]

The compounds of KC_{24} Potassium graphite is well known for its use as one of the most potent reducing agents, a catalyst in polymerizations, a neutron monochromator, a carbon-based anode in potassium-ion batteries, and a coupling reagent for aryl halides to biphenyls. [172] CaC_6 shows the highest critical temperature $T_c = 15.1\ K$ at 8 GPa among the superconducting GICs. [173] Regarding the synthesis of graphene, it is interesting to note that these intercalants with a low staging index increase the interlayer distance of graphene, weakening the force that holds them together. This implies a lower energy demand to achieve graphene layers' dispersion in the "solution," which occurs even without ultra-sonication by only through mixing processes. [174-178] However, this method, together with the methods discussed in section 353.2, does not prove to be a good candidate for applications for the electronic devices industry because it does not allow effective control of the size of the dispersion graphene sheets, which also have a high amount of structural defects. Their defective nature and structural characteristics do not allow them to be used in the manufacturing process of electronic devices but are very useful for applications such as conductive inks, coatings, composites, energy storage, biomedical applications, and transparent conductive layers. [159, 177, 179-181]

3.2.1.3 Solvent assisted-exfoliation

With this technique, a dispersion of graphene powder is prepared by chemical solvents such as N-methyl-2-pyrrolidinone (NMP), the most used at the moment. Here, the dispersion is subjected to ultra-sonication to promote the detachment of graphene layers, as shown in Figure 3.5 (top-right). [66, 182-184] A grey liquid is formed after the ultra-sonication. It comprises a homogeneous phase and several macroscopic aggregates, which are then removed by low-rpm centrifugation. This giving rise to a dark and homogeneous dispersion. Those that have superficial

energy equal or close to that of the crystal are the solvents that have shown a better result in their application. That means the tension at the graphene/solvent interface is comparable to that present in the graphene/graphene interface. [36, 184, 185]

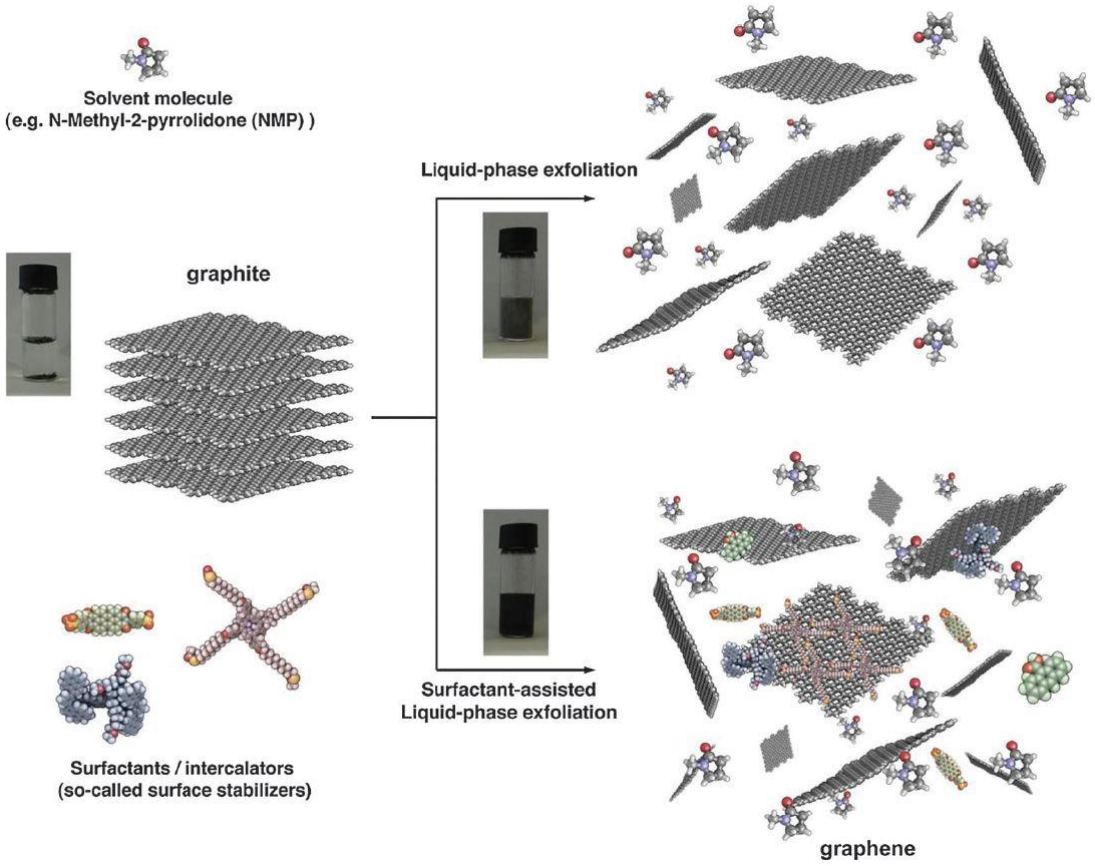

Figure 3.5 Schematic illustration of the procedure known as "graphene liquid-phase exfoliation." Here, the top-right shows the process involving an ultra-sonication and a solvent such as N-methyl-2-pyrrolidinone (NMP). The bottom-right represents the method that involves surfactants/intercalants, as discussed in the previous section. [184]

That means it has two main consequences, the energy cost necessary to separate the graphene layers is minimal, and once the crystals are dispersed, the recombination process in the form of crystals is no longer the preferred one. So, the crystals in suspension tend to remain isolated, and the solution remains stable for a longer time. [36, 159, 162] However, due to their known toxicity

to humans, these solvents require special care when handled. This is one of the reasons why new, more environmentally friendly solvents, such as water, are in demand, as discussed in the previous section 3.2.1.1.

3.2.1.4 Chemical exfoliation of graphite oxide

Graphite oxide is considered as a set of graphene layers, whose carbon atoms are chemically bound to a certain number of oxygen atoms (intercalated oxygen), depending on the level of oxidation suffered by the graphite crystal, resulting as impurities in the sheet or as functional groups such as carbonyl ($C = O$), hydroxyl ($-OH$) and phenol. [186-191]

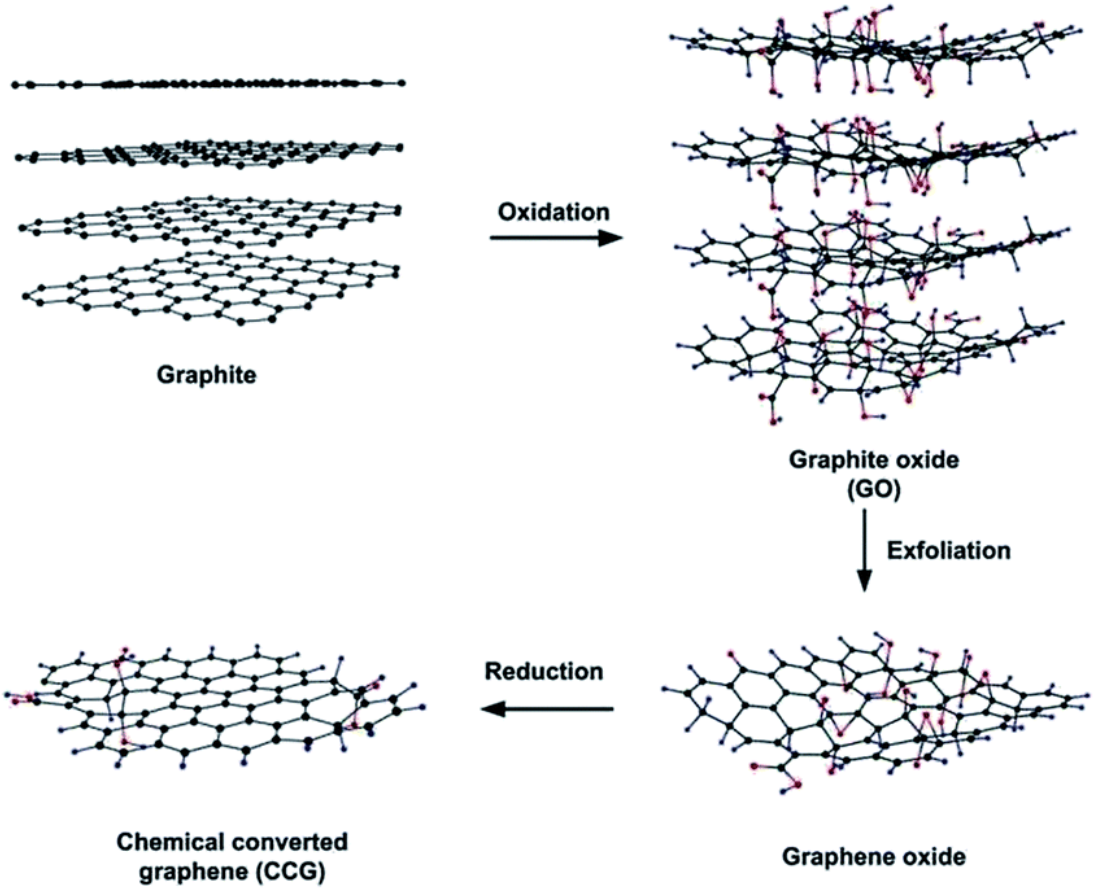

Figure 3.6 Schematic of chemically converted reduced graphene oxide (rGO) preparation method by the exfoliation of graphite oxide. [192]

Graphene oxide (GO) is obtained by exfoliation of the graphite oxide, as shown in Figure 3.6 (bottom-right), and there are many ways to prepare it. The most effective method is the method developed by William S. Hummers Jr. and Richard E. Offeman in 1958, [191] which requires the use of concentrated sulphuric acid (H_2SO_4) and potassium permanganate ($KMnO_4$). These reactions affect the network of sp^2 bonds of graphene sheets, through the introduction of functional groups in the basal plane. [193] The introduction of these impurities has mainly two effects (1) it considerably increases the distance between layers, and (2) it promotes the intrusion of water molecules into the compound as their introduction makes the compound hydrolytic. [193, 194]

Once graphene oxide is obtained, it tends to disperse into distilled water, organic solvents, or aqueous methanol solutions. In order to complete the detachment of the different sheets, the suspension solution is subjected to ultra-sonication processes. [192-194] Graphene oxide has a high resistivity, and therefore an insulator. [195, 196] To obtain a conductive material again, it is necessary to subject it to a reduction process to carry out the partial or total removal of the functional groups that increase resistivity. This way, reduced graphene oxide (rGO) is obtained, as shown in Figure 3.6 (bottom-left). [192] The process is carried out by chemical methods (using hydrazine monohydrate & hydrogen gas or strongly alkaline solutions), by thermal and electrochemical methods. [197-201] As an alternative to the reduction process, chemically modified graphene (CMG) can be produced through a chemical process with different functional groups, which improves some specific properties. In general, the yield of the graphene oxide production process is relatively high, and it comes closest to being industrially scalable. Its characteristics make it suitable for synthesizing enhanced graphene with the addition of other functional groups. The outputs are known as Chemically Modified Graphene-CMG or

Functionalized Graphene-FG and individual layers of pure graphene. The perspectives of these materials are mainly in the pharmacological and medical fields, such as bio-sensor construction, drug delivery systems, or tissue engineering. Nevertheless, they are not suitable for all applications that require a graphene quality as close to pure as possible. [202-205]

3.2.2 Mechanical exfoliation of graphite

3.2.2.1 The method which worth a Nobel price: Scotch-tape method

This method corresponds to the simplest and most basic way to obtain graphene. As mentioned in section 1.2.3, it is the one which the two researchers, Konstantin Novoselov and Andre Geim, were able to isolate micrometric flakes of this material, in the laboratories of the University of Manchester, in 2004. [31, 36] The exfoliation technique consists of separating graphite into individual layers, which is discussed well later within this section. Graphite is easily "exfoliated" by its nature because the graphene layers that compose it are superimposed on each other and are held together by weak Van der Waals forces. This weak attractive force creates cohesive energy of only $2\ eV/nm^2$ between the atomic planes that can be overcome with the application of a force of $300\ nN/\mu m^2$, [206] parameters that allowed the execution of this method using only scotch tapes. Although it is better known as the “Scotch Tape Method," the mechanical exfoliation of graphite has already been explored in other ways for an extended period. Due to the failures that occurred by the chemical exfoliation method, the researchers chose to interact with the graphite mechanically by scraping and rubbing the material on surfaces to obtain progressively thinner graphite wafers. The technique, known as the micro-mechanical exfoliation, worked surprisingly well despite its rusticity.

Scientists were able to produce graphite thin films which have thicknesses of less than 100 atomic planes. [207] The novel discovery of carbon nanotubes and fullerenes provided new inspiration to search for efficient separating graphite layers during the 1990s. In 1999, Rodney S Ruoff and collaborators [208-210] used the atomic force microscope (AFM) probe to exfoliate columns of highly oriented pyrolytic graphite (HOPG) which is a type of graphite synthesized in the laboratory. This could have been the Nobel Prize-winning discovery if they have used proper equipment and a correct angle of approach. According to Dr. Ruoff, they have used a scanning tunneling microscope (STM), an atomic force microscope (AFM), and a scanning electron microscope (SEM) for characterization, which did not allow them to prove or disprove that the flakes consist single layers. [210, 211] Dr. Philip Kim and collaborators at Columbia University followed a similar approach by creating a nano pencil/AFM probe by adding the columns of graphite to the probe and promoting its exfoliation by the contact of the probe with the substrate. Flakes with a thickness of about 5 nm, corresponding to approximately ten layers, were obtained. [210] Therefore, writing with a pencil could be considered as an immediate example of graphite exfoliation. As mentioned at the beginning of section 3.2.2.1, to isolate the graphene flakes, K. Novoselov and A. Geim used scotch tape applied to some fragments of HOPG in order to separate the crystalline grains. In the mechanical exfoliation process, HOPG is exfoliated in several steps, repeating the operation several times with scotch tape to make graphene layers as thin as possible as shown in Figure 3.7.

According to Geim, to obtain samples of a thin sheet of graphene with the high crystallinity disclosed, it is necessary to work in a clean environment where the oxidized silicon substrates, scotch tapes, tweezers, and graphite flakes are kept clean. This method has been implemented and improved by many research groups, and now the method is well known. So, in the first step, the

surface impurities and any oxidized layers of the material are removed using scotch tape, and in the second step, the second strip of scotch tape was used to the mineral layers continue to be removed. Generally speaking, the graphite flakes should be deposited with tweezers on a piece of scotch tape which should be folded at 45^0 angle and only then pressed on the flake.

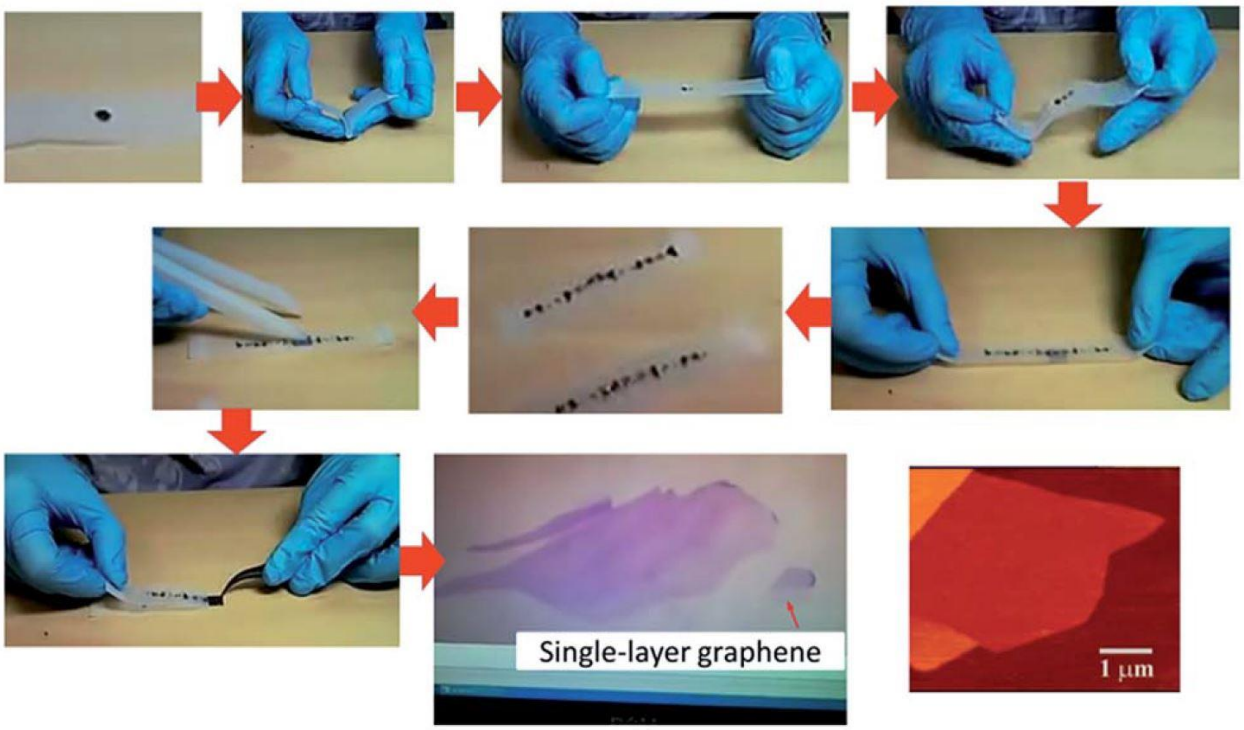

Figure 3.7 Mechanical exfoliation of HOPG using scotch tape in order to make graphene flakes thinnest as possible. [212]

Note that the tape should be pulled carefully in order to achieve a successful exfoliation of the graphite. A series of exfoliations (10-20 times) have been implemented by repeating the process until a thin layer of graphite is obtained, which would be invisible without the aid of an optical microscope and rigid support of silicon oxide of suitable thickness.

It is possible to observe the individual graphene flakes despite their monoatomic thickness, under an optical microscope, as shown in Figure 3.7, within certain wavelengths of the incident

light and for certain thicknesses of silicon oxide. Geim and Novoselov were able to observe some graphene flakes under an optical microscope because they used 300 nm thick SiO_2 substrates, a "magic" thickness for which the monoatomic sheets are capable of giving optical contrast. On this SiO_2/Si support, in addition to graphene flakes, graphite and glue residues are also observed, then the sample is washed in a solution of acetone ($(CH_3)_2CO$) and then with isopropyl alcohol ($CH_3CHOHCH_3$). To remove any residual solvents used in the washing phase, the SiO_2/Si substrate is heated and subsequent observations under an optical microscope allow a better estimate of the size of the graphene flakes. The graphene produced by this method has perfect crystallinity, which is responsible for its exceptional properties since it is derived from graphite and does not pass through any equipment or intrusive procedure. However, the flakes produced reach only 100 μm and are obtained in isolated pieces or mixed with multi-layered graphene, which does not allow their application on a large scale. Thus, the graphene synthesized by mechanical exfoliation is suitable only for basic research and for device demonstration. [31, 36]

3.3 Epitaxial growth of graphene on substrates

3.3.1 Graphene growth on Silicon Carbide (SiC)

Silicon Carbide (SiC) is one of the most common materials used for "power electronics," known as high power semiconductor electronics. [213-216] Epitaxial thermal growth on silicon carbide (SiC) is one of the most praised highly crystalline graphene growth techniques. The term "epitaxy" is related to the Greek roots where the prefix epi means "upon" or "over," and taxis means "arrangement" or "order." [217] The process is called epitaxial growth, where an epitaxial monocrystalline film is deposited on a mono-crystal substrate. Two main epitaxial growth processes depend on the growth substrate, “homoepitaxial” and “heteroepitaxial” growth. If the

substrate and the film applied to it are the same material, the film is called the homo-epitaxial layer. When those are different, it is called the hetero-epitaxial layer. [157, 217]

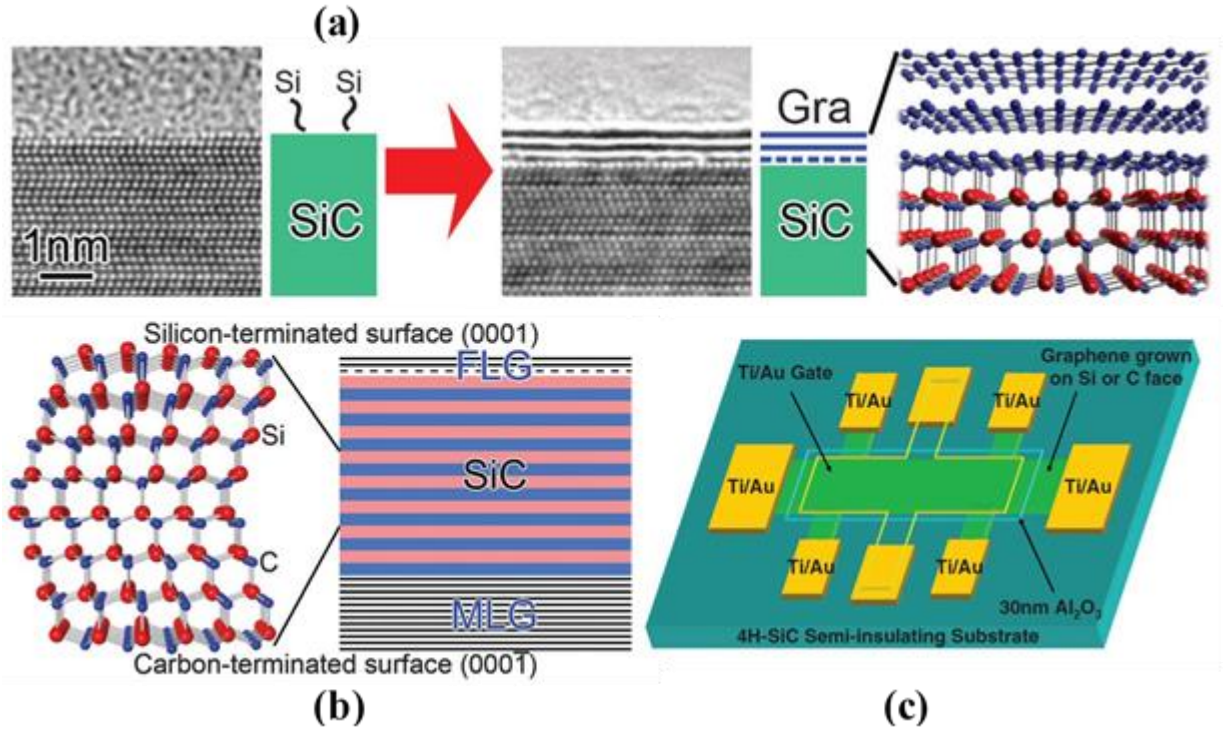

Figure 3.8 Illustrations of crucial stages of the few-layer and multi-layer graphene growth by thermal decomposition of SiC. (a) before (left) and after the growth of graphene on SiC and few-layer graphene (blue lines) and the buffer (blue dashed line) layers are visible. The 3D model on the right-hand side represents the structural model of double-layer graphene. (b) crystal structure of SiC and graphene on Silicon-terminated surface and Carbon-terminated surface. Red balls correspond to the silicon atoms, and the blue balls represent the carbon atoms. (c) 3D diagram of a graphene field-effect transistor (GFET). It has been fabricated using a gate insulator of Al_2O_3 and a Ti/Au gate electrode. [218]

Forbeaux, Themlin, and Debever, in 1998, described the formation of graphite layers on the surface of the SiC wafer during the sublimation of Si atoms. [219] Berger et al. (2004) first reported the works on obtaining graphene in the thermal decomposition of the SiC substrate surface. They observed the formation of polycrystalline layers of graphene, oriented randomly. [220] Later, many works that describe the processes of controlling the number and orientation of formed graphene layers have been introduced. [221-225] When the SiC substrate is annealed at

high temperatures, such as from 1200^0C to 1700^0C, in a high vacuum atmosphere, Si atoms selectively evaporate from the surface, and then the remaining C atoms form graphene layers. [226-229] The characteristics and morphological properties of epitaxial graphene depend on the edge/surface of the SiC plate on which it is grown (Figure 3.8b). Films growing on the C-face (Carbon-terminated surface) are several layers thick (bottom layer shown in Figure 3.8b), disoriented from each other, and look like separate scales. [218, 230-232] Additionally, films grown on the Si-face (Silicon-terminated surface) have a homogeneous appearance, and they often consist of single or double-layer graphene (top layer shown in Figure 3.8b). [233-237] The epitaxial growth of graphene on SiC is presented as a very promising method for large-scale production and application in electronics. Device applications based on SiC-graphene such as high-frequency electronics, bio-electronics, light-emitting devices, high-profile transistors, and solid-state radios have been developed (Figure 3.8c). [238-244] High-frequency transistors with a cut-off frequency of 100-280 GHz were also created, which is higher than in modern Si-transistors with the same shutter length. [42, 245] Moreover, graphene on SiC has been used to study the quantum Hall effect (QHE). [31, 246-251] The quality of graphene obtained in this way can be very high, with crystallite sizes reaching hundreds of micrometers. Nevertheless, the main disadvantages of this method are the high cost of SiC wafers (over $500 per 6-inch diameter wafers) and the use of high temperatures (above 1200°C), which are not directly compatible with silicon electronics technology. Therefore, this method is not suitable for industrial production.

3.3.2 Chemical vapor deposition (CVD) method

(Please note that section 3.3.2 is based on the figures and ideas given in Miao et al. 2011 [252] from the book titled, "*Physics and Applications of Graphene: Experiments*," authored by Sergey Mikhailov (2011) [253] and the book titled, "*Handbook of chemical vapor deposition: principles, technology, and applications*," authored by Hugh O. Pierson (1999). [254]

The mainly used method to synthesize large-area graphene on catalyst substrates is the Chemical Vapor Deposition (CVD) method. The ability to synthesize graphene thin films with good uniformity and that can be transferred to other substrates, combined with the relatively inexpensive, fast, and simplicity of the process, has made it the most promising method for large scale graphene production, as mentioned in Chapter 1. [225, 255-257]

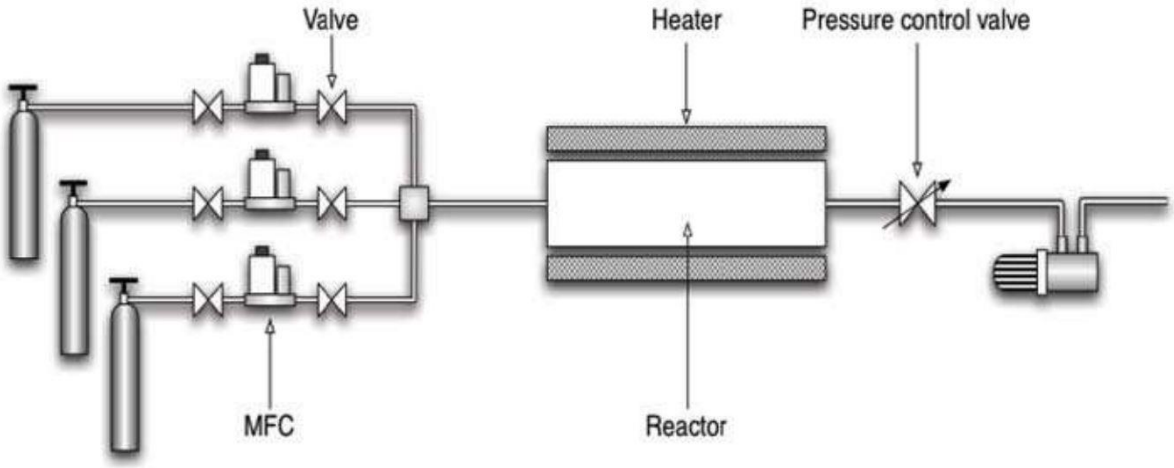

Figure 3.9 Schematic of a typical CVD system with a quartz tube furnace. Mass flow controllers (MFCs) regulate the gas flows and then feed into the quartz chamber known as the reactor. The reactor is heated using a heater/heating element, and the pressure control valve regulates the reactor pressure. The vacuum pump on the right-hand side uses to remove exhausted gases. [252-254]

A schematic of a typical CVD system for graphene production is shown in Figure 3.9. The system can be divided into three main parts such as the inlet part (Figure 3.9-left), the reactor

(Figure 3.9-middle), and the outlet part (Figure 3.9-right). The inlet part is used to regulate the amount of gases entering the reactor using special valves controlled by a computer known as a Mass Flow Controller (MFC). Chemical reactions inside the reactor at high temperatures cause the desired material to settle on the substrate. High temperatures (up to 1200^0) in the reactor are very often achieved by a heating element. The outlet part is used to regulate the pressure in the reactor.

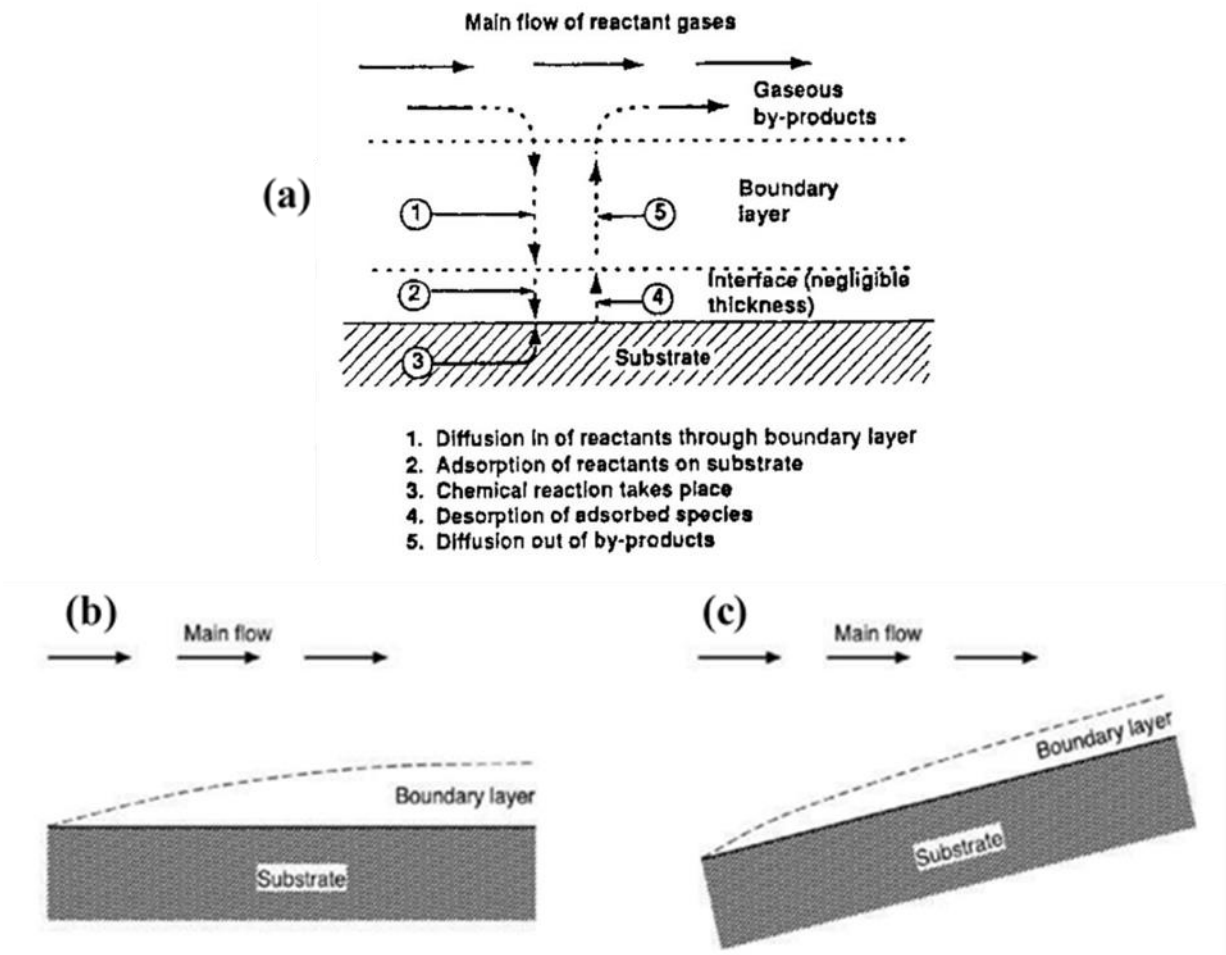

Figure 3.10 Schematic of the precursor decomposition during the CVD growth of graphene at a catalytic surface and the boundary layer above the catalyst surface. (a) a step-by-step precursor decomposition process. (b) The boundary layer is thicker when the substrate is parallel to the direction of the flow. (c) The boundary layer is thinner than (b), and the substrate is tilted against the main flow direction. [252-254]

The ability to control and maintain the pressure in the reactor is crucial for the correct execution of the chemical reaction. One or more vacuum pumps are used to pump the gases such as $Ar/H_2, CH_4, O_2, N_2, etc$. Pressure regulation is performed employing a special throttle valve. The experimental setup of a CVD furnace may not seem too complicated, but the CVD process can be pretty complicated and very sensitive to control parameters. In addition to the basic characteristics of the process, such as temperature, reactor pressure, gas flow, annealing, and deposition time, other influences must also be taken into account. Those are the gas purity, possible furnace leaks, reactor cross-section and volume, geometric arrangement, and many other parameters. As a result, even small changes in the arrangement can significantly affect the entire deposition, and it is therefore very complicated to optimize production processes in general.

There are also problems with the limited flow of gases in the reactor in CVD processes, and diffusion also becomes dominant in various parts of the reactor, as shown in Figure 3.10a. Another problem is that chemical reactions involve many intermediate steps, and for some, the exact mechanism of the reaction is unknown. The diffusion of atoms from or to the surface of the substrate can also be complicated. Because, according to the fluid dynamics, the upper layer of the substrate is formed into a layer of an uneven thickness (Figure 3.10 b and c). The diffusion rate depends on the thickness of the surface layer, so it must be as flat as possible. Graphene deposition can be divided into two parts (1) the pyrolytic decomposition of the precursor (e.g. CH_4) to carbon and residual gas such as H_2 (2) the formation of a graphene structure from carbon atoms. Decomposition of the precursor should take place only on the surface of the substrate. Because if the precursor decomposes in other parts of the reactor, a black carbon layer will form, which not only settles on the walls of the reactor but also degrades the graphene being prepared. Although

these black carbon layers are formed only from carbon, their amorphous structure prevents high-quality graphene.

In order to achieve a homogeneous decomposition of the precursor on the surface, various catalysts such as transition metals are used as substrates. The purpose of the catalyst is to speed up the reaction by reducing the activation energy and, thus, reducing the reactor temperature. Because temperatures higher than 2500^0C are required to form graphene/graphitic structures without a catalyst. The high activation energy also makes the reaction process very sensitive to temperature changes.

3.3.2.1 Graphene growth on a nickel (Ni)

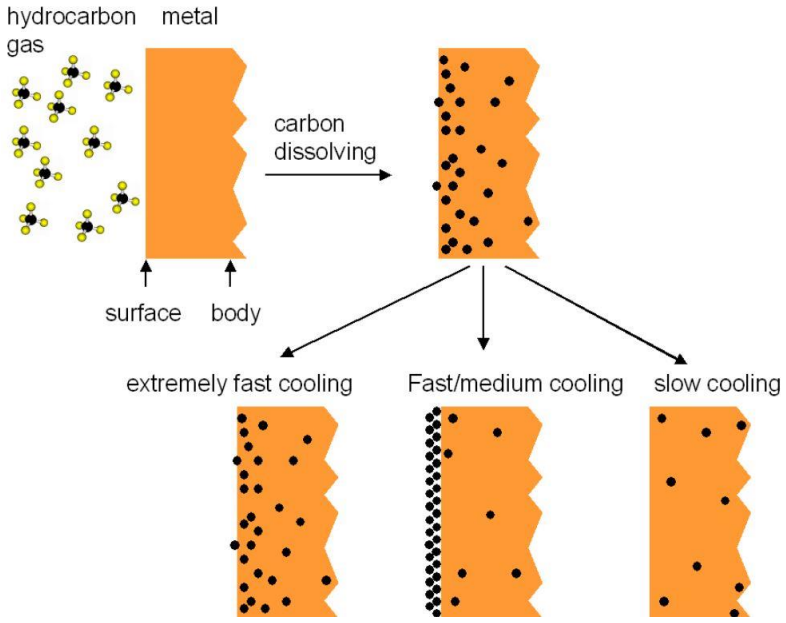

Figure 3.11 A schematic of carbon segregation at Ni-catalyst surface and a representation of graphene growth on Ni (nickel) with different cooling rates (extremely fast, fast/medium, slow). [258]

The quality of graphene is determined by the kinetics of the reactions, and it is, therefore, difficult to form high-quality graphene layers with a high activation energy of the reaction. Such high temperatures require a unique deposition system, substrate, and a large amount of energy,

making it economically not viable. As mentioned, catalysts used in the synthesis of graphene by the CVD method are mainly transition metals that carbon can diffuse. During the growth of graphene at elevated temperatures, carbon atoms deposited on the surface of the catalyst, such as nickel, then penetrate deep into the layers of the bulk catalyst (Figure 3.11-top).

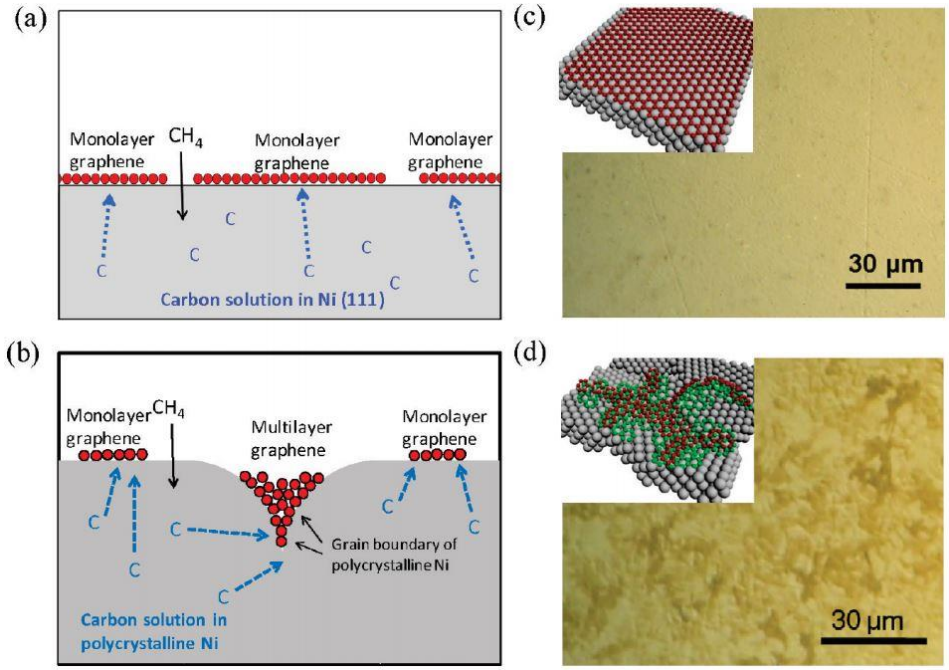

Figure 3.12 Illustrations of the graphene synthesis process on Ni. (a) Growth on a monocrystalline Ni (111) surface gives monolayer graphene. (b) Growth on a polycrystalline nickel surface that contains defects and grain boundaries. This gives multilayer and monolayer graphene. (c) Optical microscopy image of a graphene/monocrystalline-nickel which related to (a) and the inset shows a 3D diagram of monolayer graphene on Ni (111). (d) Optical microscopy image of a graphene/ polycrystalline-nickel, which corresponds to (b). The inset represents a 3D representation of monolayer and multilayer graphene on the polycrystalline-nickel surface. [259]

Furthermore, the cooling rate is an important parameter that can affect the number of graphene layers, as shown in Figure 3.11-bottom. Because, at an improperly selected cooling rate, these atoms can return to the surface and thus grow on the opposite side, which is an undesirable result to have. So, with a very rapid cooling rate, the carbon atoms do not have enough time to

return to the surface and remain inside the nickel. Therefore, as shown in Figure 3.11-bottom-left, only a tiny part of the carbon atoms remains on the surface. At average cooling rates, quality graphene is formed (Figure 3.11-bottom-middle), while at slow cooling rates, the carbon atoms diffuse deep into the nickel, and almost nothing remains on the surface (Figure 3.11-bottom-right).

The roughness, mainly because of the grain size and the grain boundary, is an important property of the catalyst influencing the quality of graphene. The deposited carbon atoms, or atoms diffusing from the bulk back to the surface, more favorably settle at places with higher surface energy, grain boundaries, and surface defects. These defects and grain boundaries have multiple binding sites at which carbon atoms can more easily settle. The resulting graphene layers are then unevenly distributed over the surface, such that the thicker layers around grain boundaries and thin/single-layers of graphene in other places, as shown in Figure 3.12. Therefore, annealing the catalyst is used before graphene growth to increase grain size and eliminate defects.

3.3.2.2 CVD growth of Graphene on Copper (Cu)

When nickel is used as a catalyst (via precipitation of carbon as shown in Figure 3.13a), problems arise at high temperatures with the diffusion of carbon atoms into the inner layers of nickel and the undesirable growth of graphene multilayers at an inappropriately chosen cooling rate. For this reason, a copper catalyst (via surface mediated growth, as shown in Figure 3.13b) is more suitable for the production of graphene, into which carbon atoms can hardly diffuse at all, even at a temperature of 1000^0C. The graphene layer is formed on the surface directly during the decomposition of the hydrocarbon (e.g. CH_4). There is no undesired precipitation/diffusion of carbon from the bulk of copper during the cooling stage. Furthermore, graphene production on copper foil requires lower pressure and lower temperature than the use of nickel as a catalyst. Due

to those reasons, the production process is greatly simplified. At a given pressure and reaction temperature, it is not hard to determine the amount of precursor for forming one layer of graphene.

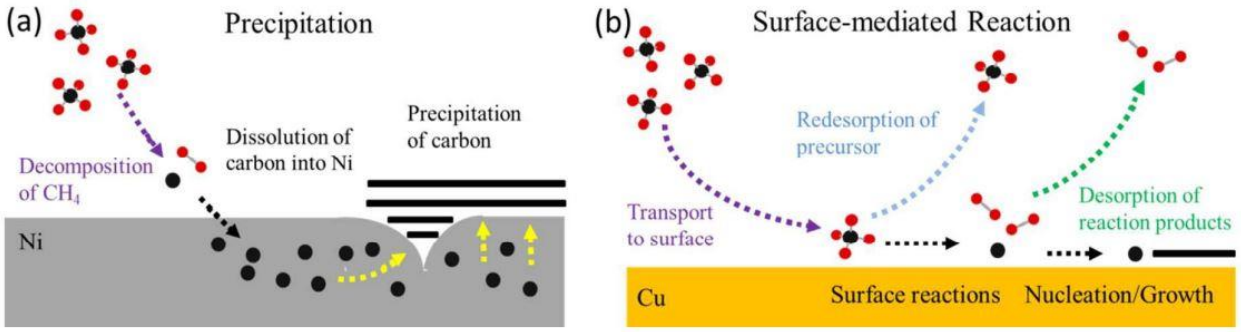

Figure 3.13 Illustration of the significant differences and the growth kinetics during the graphene synthesis via (a) precipitation on nickel and (b) by surface-mediated growth on copper. [260]

3.3.2.2.1 Step-by-step process of graphene synthesis

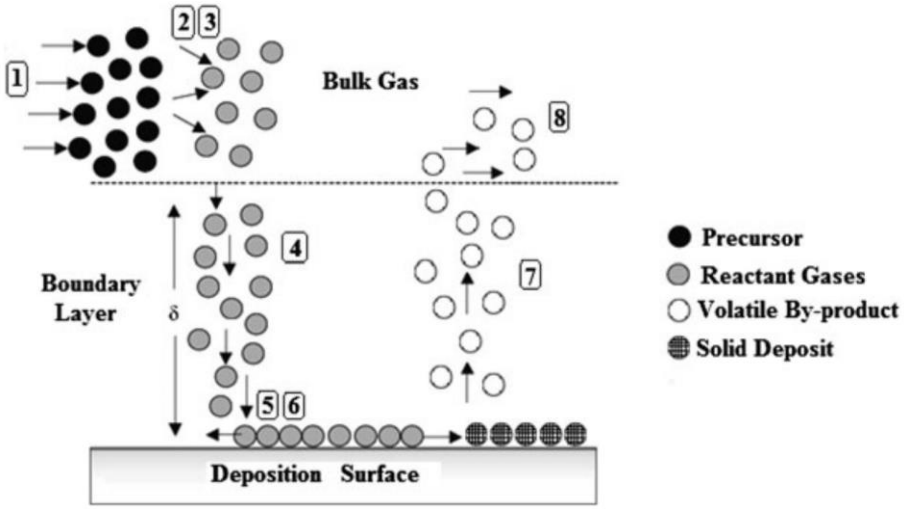

Figure 3.14 Schematic diagram of the physicochemical stages of the CVD synthesis (1) precursor transport from the bulk gas region into the reactor (2) evaporation of reactant gases (3) reactant gases chemically reacts to form immediate reactants and also produces the gaseous by-products (4) Diffusion of reactant gases from the bulk gas region to the catalyst surface through the boundary layer (5) Adsorption of the reactants on the deposition surface of the substrate (6) Surface diffusion of reactant gases to growth sites, where nucleation happens and formation of graphene islands at the surface (7) Desorption of volatile by-products from the deposition surface to the bulk gas region (8) Gaseous by-products move away from the reactor. [261]

Generally, there are few simple and critical steps of the chemical vapor deposition (CVD) of graphene, (1) Heating, (2) Annealing, (3) Growth, (4) Cooling, and (5) Reactor pressurization. At the first step, the catalyst substrate and the reactor are heated at a constant rate under a controlled atmosphere to annealing the temperate. Next, regulate the annealing temperature and gas atmosphere in which the catalyst surface is reduced/smoothed and modified, as mentioned before. The morphology features of the substrate include surface roughness, crystalline orientation, and grain size of the metal catalyst. Additionally, metal evaporation should be avoided as much as possible, discussed in a later chapter. The growth step involves the injection of the carbon-containing precursor such as CH_4 and growth of graphene on the Cu catalyst substrate (Figure 3.14 contains the complete growth mechanism of graphene on Cu). Many parameters can change the output, such as a single layer or multilayer graphene. So, during the growth step, such parameters as pressure, the ratio of a gas mixture, annealing time, growth time, temperature, gas consumption, etc., can be changed.

It is important to take into account that depending on the nature of the gas mixture, etching of graphene is possible not in the growth phase but in the subsequent stage during cooling (e.g., in higher H_2 concentrations and absence of a carbon precursor, graphene can be etched at high temperatures during the initial cooling down steps. See the equation (3.10)). In the cooling phase, the reactor undergoes a cooling step in an environment similar to the annealing or growth phase (this environment could be varied under exceptional circumstances) until the reactor temperature drops below 200^0C to prevent oxidation of the catalyst surface not coated with graphene and prevent oxygen-containing groups of directly coated graphene from functionalizing. As mentioned in the previous section, when using substrates with high solubility, the dynamics of the cooling stage are crucial for controlled growth. Finally, the reactor should be pressurized to atmospheric

pressure by filling inert gases or simply opening the pressure control valve, as shown in Figure 3.9.

3.3.2.3 Growth kinetics of graphene synthesis: a summary

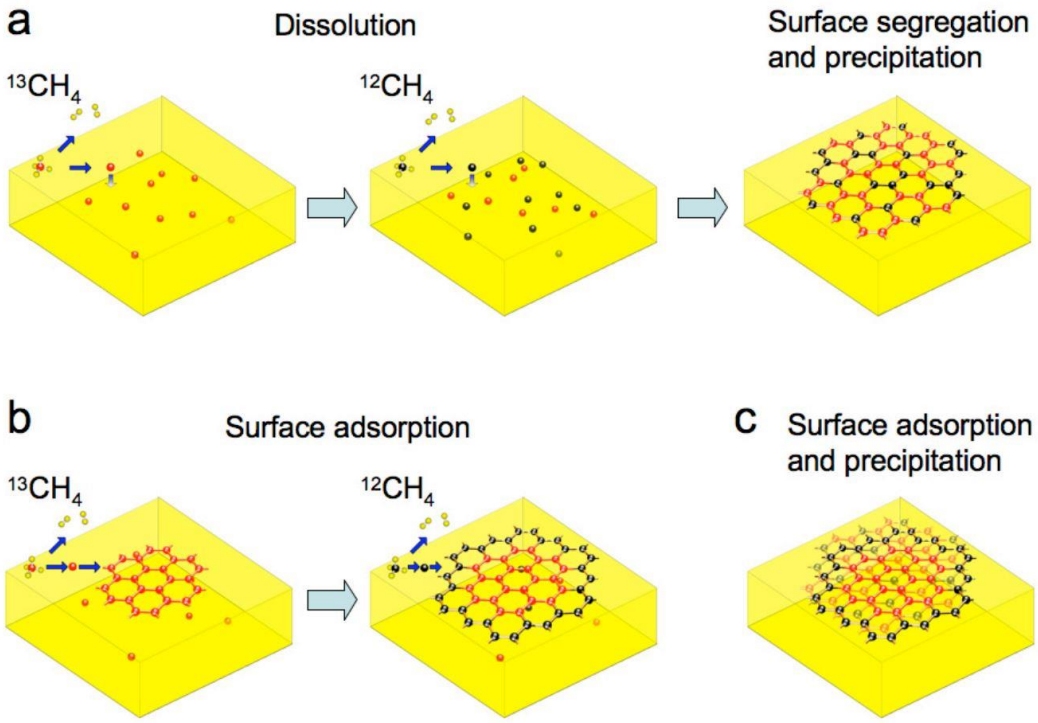

Figure 3.15 Schematic illustrations of all possible distribution of carbon isotopes. It is based on various growth procedures and kinetics discussed in this section (a) a layer of graphene formed on a catalyst surface by carbon isotopes mixed randomly. First, the precursors went through a dissolution step, and graphene was formed via surface segregation and precipitation. (b) Graphene formed with separated isotopes. It forms via two separate surface adsorption steps. (c) Combined growth by precipitation and surface adsorption. [262]

Hydrocarbon precursors such as methane (CH_4), acetylene (C_2H_2), ethylene (C_2H_4), etc. are usually used as a carbon source. Among them, the most widely used one is methane (CH_4). Due to the strong $C-H$ bonds ($+415.5\,kJmol^{-1}$) in the CH_4 molecule, [263] its thermal decomposition occurs at very high temperatures (more than 1200^0C as mentioned previously). In

order to reduce the decomposition temperature of CH_4, various transition metal catalysts such as Cu, Ni, Co, Fe, etc., are widely used. When CVD-synthesis of graphene is performed on metals at temperatures less than 900^0C, the catalytic effect is observed to a lesser extent. The growth kinetics mainly depends on the properties of the catalyst, particularly the solubility of carbon at high temperatures in the metal. [264-268] In the case of synthesis on copper substrates, carbon does not dissolve in the metal of the substrate; the main processes that determine the growth are the dissociation of gas molecules on the copper surface, including at the boundaries of already formed graphite-like structures, and surface diffusion of carbon into the formation region of graphene structures as shown in Figure 3.15.

The following set of equations represents the chemical reactions at the transition metal surface that promotes graphene growth. The overall reaction process can be summarized into a decomposition of CH_4 in to carbon and H_2Which leads to graphene growth at the Cu catalyst surface. [269]

$$CH_{4(g)} + S_{(Cu)} \rightleftharpoons CH_{4(a)} \tag{3.2}$$

$$CH_{4(a)} + S_{(Cu)} \rightleftharpoons CH_{3(a)} + H_{(a)} \tag{3.3}$$

$$CH_{3(a)} + S_{(Cu)} \rightleftharpoons CH_{2(a)} + H_{(a)} \tag{3.4}$$

$$CH_{2(a)} + S_{(Cu)} \rightleftharpoons CH_{(a)} + H_{(a)} \tag{3.5}$$

$$CH_{(a)} + S_{(Cu)} \rightleftharpoons C_{(a)} + H_{(a)} \tag{3.6}$$

This can be summarized as follows,

Dissociative adsorption of methane

$$CH_{4(g)} + 5S_{(Cu)} \rightleftharpoons C_{(a)} + 4H_{(a)} \quad (3.7)$$

Hydrogen Desorption

$$4H_{(a)} \rightleftharpoons 2H_{2(g)} + 4S_{(Cu)} \quad (3.8)$$

Graphene Formation from adsorbed carbon

$$C_{(a)} \rightleftharpoons Graphene_{(a)} \quad (3.9)$$

The reversible reaction of graphene formation by the CH_4 decomposition at the Cu surface.

$$CH_{4(g)} + 5S_{(Cu)} \rightleftharpoons Graphene_{(a)} + 2H_{2(g)} \quad (3.10)$$

Where (a) represents the atomic states such as $C_{(a)}$ and $H_{(a)}$ (those two are known as adsorbates). Moreover, (g) represents the gaseous states such as $CH_{4(g)}$ or $H_{2(g)}$ and $S_{(Cu)}$ represents Cu surface sites where the above reactions are possible. [269]

Since the graphene growth process on a transition metal substrate is a heterogeneous catalytic chemical reaction, [270-272] the metal acts as a substrate and a catalyst. A carbon film grown on the surface of a metal substrate reduces its catalytic activity, which is known as catalyst poisoning. [271, 272] Hence, the formation of a graphene film should lead to a termination of the reaction. If the entire process is carried out on the surface (adsorption, decomposition, and diffusion of molecules), then a predominantly monolayer graphene should be formed (Figure

3.15). This effect is known as "self-limiting," which has been observed only on Cu under certain growth conditions. Note that in the case of Cu, single-layer graphene is not always formed, and multilayer graphene may also form. When a copper surface is completely covered with graphene, with the formation of small regions of multilayer graphene, an effect of a significant growth slowdown was observed by Xuesong Li et al. (2010) [114] and also by Wei Liu et al. (2011). [118] The change in the growth rate is that the growth of the first layer is caused by surface adsorption of carbon atoms from the gas phase on the copper surface and surface diffusion of atoms into the graphene film formation area. In contrast, the growth of the subsequent layers is possible only along the boundaries of the forming planes, which can be germinated by defects of the previous layer. The deposition process is far more complex at higher temperatures above 1200^0C. In this case, the decomposition reaction starts to develop in the gas phase and must be considered along with the catalytic decomposition.

4 THE ROLE OF SURFACE MORPHOLOGY ON NUCLEATION DENSITY LIMITATION DURING THE CVD GROWTH OF GRAPHENE AND THE FACTORS INFLUENCING GRAPHENE WRINKLE FORMATION

CVD graphene growth typically uses commercially available cold-rolled copper foils, including a rich topography with scratches, dents, pits, and peaks. Even after annealing the foil, the graphene grown on this topography tends to include and reflect these topographic features. Further, the transfer of such CVD graphene to a flat substrate using a polymer transfer method also introduces wrinkles. Here, we examine an electropolishing technique for reducing native foil defects, characterize the resulting foil surface, grow single-crystal graphene on the electro-polished foil, and examine the quality of the graphene for such defects.

4.1 Introduction

Since the first preparation of tiny flakes of exfoliated graphene from graphite, this 2-D material has attracted enormous attention due to its unique electrical, chemical, and physical characteristics, promising various applications in nano-photonics nano-electronics, and optoelectronics. [35, 38, 54, 56, 220, 244, 273-281] For such applications, the desirable features of graphene include high mechanical strength, chemical stability, high optical transparency, and gate-controllable electrical transport characteristics. [244, 276, 277, 281] It turns out that large-area graphene can be fabricated by chemical vapor deposition (CVD) techniques on thin metallic catalyst surfaces like copper (Cu) or nickel (Ni). Thus, the CVD process has become an attractive means for producing large-area graphene due to its simplicity and relatively low cost. [74, 104, 282] However, one of the significant drawbacks of CVD graphene is grain boundaries, defects,

and wrinkles in the polycrystalline graphene, which adversely affects electrical transport and structural properties.

CVD graphene grown on copper turns out to be polycrystalline because of the high nucleation density on the copper foil surface, which is typically ~106 sites/cm^2. [109] In order to realize better quality LPCVD graphene, this nucleation density needs to be reduced to ~1-2 sites/cm^2 so that single crystals can grow to a much larger cm-scale size before coalescing with neighboring graphene flakes. Previous studies have demonstrated that substrate pre-treatments [109, 283-285] and control of the gaseous precursors [114, 286-289] can be used to limit the nucleation density to a great extent. These studies also have demonstrated that the presence of oxygen on the surface of the metal catalyst is a crucial ingredient for synthesizing large-scale mono-layer single-crystal graphene. [109, 119, 286, 287, 290-293] For example, heating and the Cu foil at 800 mbar under Ar environment and then annealing in an Ar/O_2 environment (800 mbar, 1050 ^{0}C, ~100 ppm O_2) gives a 16 sites/cm^2. [294]. Another group has yielded ~2 sites/cm^2 for a shorter period while claiming that the increase of CH_4 flow rate from 7 to 75 sccm would significantly rise in nucleation density up to 770 sites/cm^2. [295] It would, however, be desirable to reduce the nucleation density further, perhaps to <10 sites/cm^2.

Hence, we examine and report on the possibility of limiting the surface defects by electropolishing the Cu foil while utilizing Cu enclosures to limit the nucleation density and reduce growth rates. [286, 292] Using such a strategy, single-crystal graphene was grown on electropolished, oxidized copper foil. The Cu foil and the resulting graphene were studied for structural changes induced by foil preparation and the growth process using scanning electron microscopy, atomic force microscopy, and optical microscopy. The results of such a study are reported below.

4.2 Experimental Methods

4.2.1 Electropolishing and graphene growth

These studies were carried out on industrial-grade 25 µm-thick Cu foils, cut to a rectangular shape with 7 cm x 5 cm dimensions. Initially, oxidized Cu foils showed an uneven color due to a pre-existing thin oil/grease layer on the Cu foil produced by the cold-roll-press method. Thus, the Cu foils were pre-cleaned in a 10% Acetic acid (CH_3COOH) solution for 1 min. (See Figure 4.1). After further cleaning of the Cu foil with Acetone, Methanol, and Deionized water, the foils were electro-polished using an electrolyte containing Phosphoric Acid (H3PO4), Ethanol (CH_3CH_2OH), iso-propanol ($CH_3CHOHCH_3$), Urea ($CO(NH_2)_2$), and a small amount of liquid Soap ($RCOO^-Na^+$). Here, the soap serves to ease the removal of the electrolyte residue from the surface after the electropolishing.

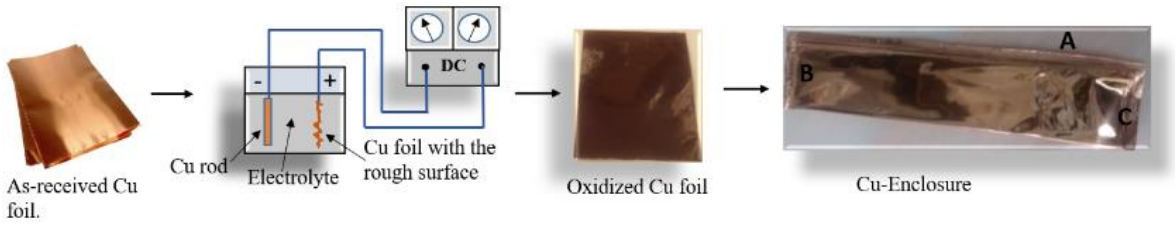

Figure 4.1 A cm x 5 cm, 25 µm thick industrial Cu foil is dipped in a 10% Acetic Acid solution (CH3COOH) for 1 min, rinsed with distilled water, dried with a flow of N_2, and oxidized by heating up to $350\ ^0C$ in open-air for 40 min. The foil is folded into Cu-Enclosure, with side A closed and B, C pressed.

In the electropolishing phase, a rapid etching procedure at the maximum current value was applied for 20 seconds to remove the surface layer of the foil. Then, a prolonged and steady etching process at a low current was utilized for 90 seconds to realize a smooth surface. After the electropolishing, the foil was rinsed with Acetone, Methanol and then with deionized water up to 5 times. Then, the foil was dried with Nitrogen and was placed on a hot plate, and oxidized (the

average thickness of the oxide was ~68 nm) for 40 min at 350 ^{0}C in the open air. Since we wanted to cover the metal surface entirely with oxides to limit nucleation, we have used a longer oxidation time. (Because we have noticed the metal surface was not fully covered with CuO when using a shorter heating time of less than 40 min). Choudhary et al. (2018) have reported that the formation of Cu_2O when using temperatures below 330 ^{0}C instead of CuO. After passing 330 ^{0}C, the CuO amount starts to increase, and with a longer annealing time (heated at 350 ^{0}C for 3 hrs.), they have been able to achieve CuO entirely. [296] Having a high concentration of CuO is beneficial than Cu_2O since the Cu: O ratio for CuO (1:1) is higher than Cu_2O (1:0.5). Lee et al. (2016) have reported a result similar to the above group. Additionally, they have discussed the increase of penetration depth of O into Cu at 300 ^{0}C with increasing oxidization times up to 4 hrs. [297]

The electropolished- and oxidized- foil were used to create an enclosure by completely folding side A and tightly pressing sides B and C (see Figure 4.1). Here, the Cu enclosure creates a stable environment, limiting the Cu and Oxygen atom evaporation during the annealing and growth process. The inner surface of the foil enclosure, which is the area of interest, was characterized by microscopy, as reported below. It has been reported that the effect of oxidized Cu enclosures to obtain large single crystals using a cold-wall CVD reactor [298], but here we describe a method that can be applied to a commonly used quartz CVD system with a furnace. Also, the previous technique has a size limitation with a CVD chamber of 4 inches, but in this work, we present a method that can be applied to many available CVD systems without a size limitation. With our method, we have obtained a nucleation density (ND) of <10 sites/cm^{2,} while the previous work was achieving an ND of 7000 sites/cm^2. The folded copper foil enclosure was also used for CVD growth. In this case, the folded copper foil was placed inside the quartz tube of the CVD

system, and the tube was evacuated to a base pressure of 22 mTorr. Argon gas was fed into the quartz tube at a rate of 50 sccm, see Figure 4.2, as the foil was heated to 1000 ^{0}C.

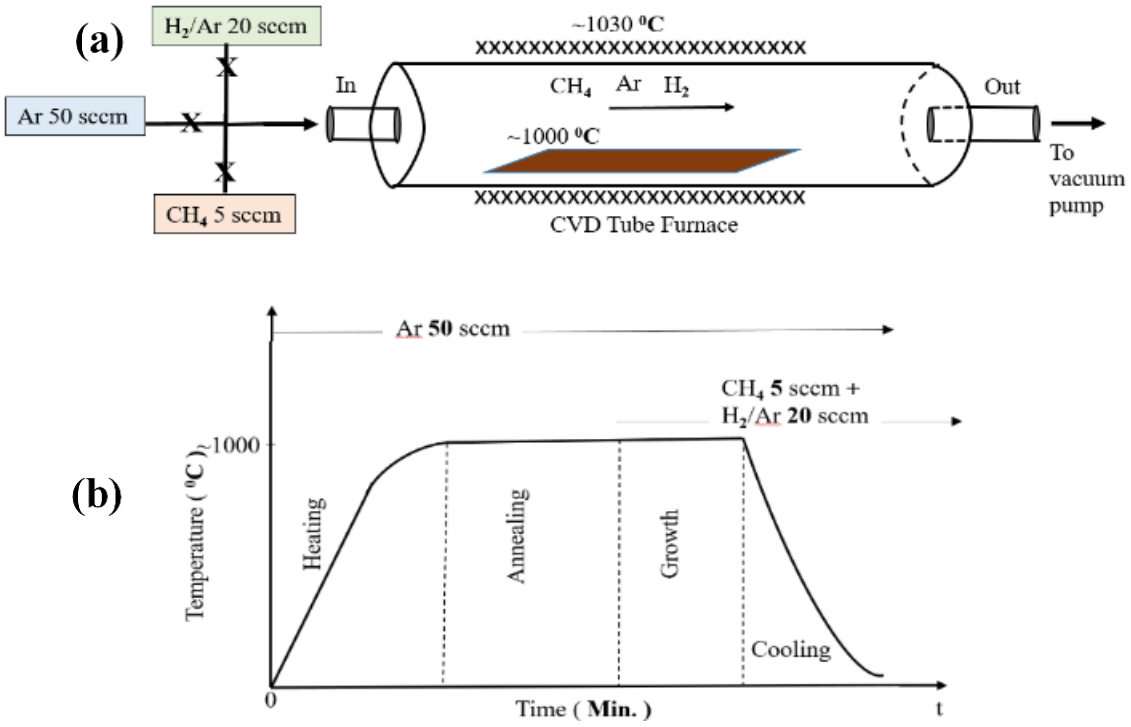

Figure 4.2 a) A schematic of the CVD tube furnace growth system. b) The graphene growth curve. The system base pressure was 22 mTorr, and the total pressure during growth was ~1 Torr.

The foil was then annealed at 1000 ^{0}C for one hour. It has been reported that Cu foils were subjected to a pre-annealing procedure providing better conditions for graphene growth. [299] In the next step, a 20 sccm flow of H_2/Ar was introduced into the growth chamber, and after two minutes, a five sccm flow of CH_4 was introduced into the system to commence graphene growth. After one hour, the growth phase was stopped, leaving the system cool down while keeping the mentioned flow rates unchanged.

4.2.2 Sample preparation and characterization

The CVD-grown graphene was transferred to SiO_2/p-Si (p-type doped Si) by using a modified wet-transfer process. A drop of PMMA (Poly (methyl methacrylate)/ PMMA 495 A4) was placed on the copper foil surface for 20 seconds before spinning. Then the PMMA was spin-coated onto the foil using a low rpm (1500 rpm) to obtain a slightly thicker PMMA layer. Next, the spin-coated sample was baked for 10 min at 100^0C. In the following step, the backside of the spin-coated sample was etched in an oxygen plasma to remove the backside graphene. The resulting PMMA/Graphene/Cu foil was immersed in a 1M $FeCl_3$ solution to etch out the Cu, leaving behind the graphene on the PMMA. The graphene/PMMA samples were rinsed a few times with deionized water to wash out the remaining $FeCl_3$ and left to float on a 10% HCl solution to remove excess metallic and other impurities. Then the graphene/PMMA in 10% HCL solution was placed on a pre-heated hot plate at 80 ^{0}C to accelerate the cleaning process. Then the samples were rinsed with deionized water ten times before transferring on to SiO_2/p-Si, where they were left to air-dry for 24 hrs., and then inside a pre-heated oven at 100 ^{0}C for 30 min. In the next step, the PMMA/Graphene film was rinsed in Acetone and then cleaned with Methanol and deionized water. The resulting graphene samples were dried with dry nitrogen gas. The surface-structural analysis of the Cu foils, Graphene/Cu samples, and Graphene/SiO_2/p-Si was performed using an OLYMPUS BH2-MJL Optical Microscope a Park XE7–AFM, and a Hitachi S-3000N SEM. The surface roughness data were also collected during the AFM scans; these data served to compare the electropolished and unpolished Cu foils.

4.3 Results & Discussion

Our primary aim was to synthesize single/few-layer highly crystalline graphene by LPCVD using a Cu foil as the catalyst substrate. To achieve this goal, it became necessary to minimize the

nucleation site density. As previous works have suggested, the cold-rolling striations and other surface defects on the substrate act as nucleation sites [298, 300], which results in more defects in the graphene film. The AFM scan in Figure 4.3a of a copper foil shows defects like cold-rolling striations, peaks, valleys, or pits, similar to mentioned defects. As they have suggested, surface morphology features can play a role, but only when much Carbon is in play (usually for higher pressure CVD) and, most importantly, when no O_2 is involved during the ramping and annealing. Suppose we anneal under H_2 a bare Cu substrate. In that case, the thermal energy will allow the Carbon contamination/intrinsic species to diffuse and gather around Cu features that decrease the energy barrier for nucleation. In this current approach, there should not be much Carbon remains after the long duration annealing of oxidized Cu under an Ar environment. However, in this current method, the effect has been dramatically reduced, as mentioned above. Moreover, from Figure 4.3f & Figure 4.4 (a & f), we can notice some nucleation in the middle of the domains, which are feature-free but have no nucleation at grain boundaries even though there are particles around, respectively. Besides, these defects add surface area for graphene growth. This feature can be seen in Figure 4.3(b-d), which shows that the additional defects create an extra surface area, and the graphene layers that were grown on them survive even after the transfer process. However, Cu grain boundary groves/ step bunching is impossible to avoid. Their contribution to the excess of the surface area is much more significant than the small features mentioned above. Figure 4.3 (b, c) shows the copper foil after graphene growth, while Figure 4.3 (d & g) shows the images of the Graphene/SiO2/p-Si after the etching of the underlying copper foil and the wet transfer. When the resulting graphene is transferred to a flat surface, the extra graphene creates wrinkles, as in Figure 4.3h.

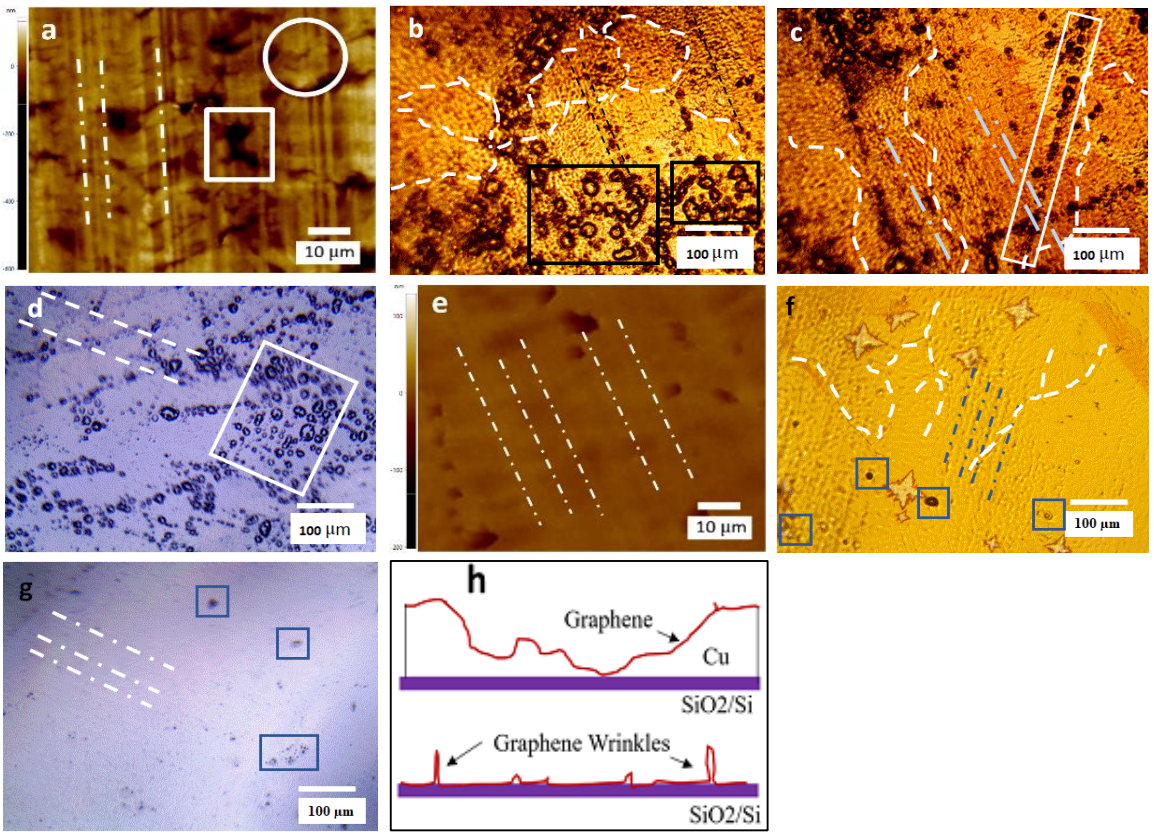

Figure 4.3 (a) An AFM image of an as-received industrial Cu foil. Here, the square and the circle indicate a valley & a pit, respectively, and the parallel dashed lines indicate cold-rolling striations (also for a-g). (b, c) An optical microscope (OM) image of as-received industrial Cu foil after graphene growth. Here, the white dashed curves (also for b, c & f) mark grain boundaries while the rectangles (also for b-d, f & g) cover the valleys which survived through the growth process. (d) OM image of Graphene/SiO2/p-Si (with graphene is grown on received industrial-Cu) after the wet transfer process. (e) AFM image of an electropolished Cu foil. (f) Optical microscope image of graphene on electropolished copper. Notice the star-shaped graphene crystallites. (g) Optical microscope image of Graphene/SiO2/p-Si, where the graphene was grown on electropolished copper. Compare with Figure 4.3d. (h) An illustration of how wrinkles are formed due to an extra graphene area.

Thus, we have implemented a modified electropolishing technique, see Experimental Methods, to reduce the native defects observed on the surface of copper foil. Then we have examined the resulting surface by AFM to characterize the result. Typically, electropolishing reduced cold-rolling striations. This feature can be observed in Figure 4.3e, which shows an AFM topography scan of an electropolished copper foil. Here, the cold-rolling striations run parallel to

the dashed lines included in the figure, and these edges appear much reduced compared to what was seen in the unpolished foil. Attempt to grow single-crystal graphene on such electropolished copper, using the enclosure geometry, leads to a reduced nucleation density, see Figure 4.3f.

We also observed fewer grain boundaries (dashed curves in Figure 4.3f) on the electropolished Cu-surface than on the non-electropolished Cu foils (Figure 4.3b & c). Furthermore, we can see the cold-rolling striations (dashed lines in Figure 4.3d & g) and valley-like structures (look inside the rectangle in Figure 4.3d & g) can survive through the wet transfer process and appear on the surface of Graphene/SiO_2/p-Si. These deformations and extra-surface areas help to create wrinkles, as illustrated in Fig. 3g. It has also been reported that the black points are shown in Figure 4.3b & c could be hydrogen embrittlement features that form due to the fast reduction of CuO. [294] This can be avoided by introducing an intermediate step between the annealing step (in a non-reducing atmosphere like Ar) and the growth step (which uses much hydrogen). To estimate the effectiveness of electropolishing, we have compared roughness data obtained by Atomic Force Microscopy for the unpolished and polished Cu substrates. [301] We have measured the root-mean-square, R_q, and the arithmetic mean deviation for this comparison, R_a.

We found that the average Rq values for as-received and electro-polished Cu foils are 131.738 nm and 79.759 nm, respectively, and the average Ra values are 107.535 nm and 57.616 nm, respectively. Thus, the electropolished surface appears smoother than the unpolished surface, which means reducing the influence of surface defects and fewer nucleation sites, as is observable in Figure 4.3f.

Table 4.1 AFM - Roughness data for as-received (unpolished) and polished Cu foils taken at different regions.

Area = 2500 (50X50) μm^2	Before Electropolishing		After Electropolishing	
Scan #	R_q (nm)	R_a (nm)	R_q (nm)	R_a (nm)
1	116.841	91.238	65.086	45.375
2	132.157	108.261	77.660	54.619
3	147.014	126.483	95.154	78.742
4	135.418	113.564	84.861	64.032
5	127.258	98.127	76.035	45.313
Avg.	131.738	107.535	79.759	57.616

In addition to the effect of surface smoothening, the reduction of the nucleation side density can also result from less surface contamination. It removes the first (or more) atomic layers during the electropolishing, thus strips out any contamination that would get turned into undesired Carbon species upon annealing. While conducting this work, we have observed some surface structures like grain boundaries (Figure 4.4a, d, e & f), ripples (Figure 4.4b & c), and cracks (Figure 4.4a, f, g & h) on graphene, which formed during the LPCVD process that can help to cause wrinkles in graphene after its transfer to a flat substrate. We have performed AFM, OM, and SEM scans on those surface areas to identify the factors that lead to the formation of defects and wrinkles in graphene. Figure 4.4a shows an SEM image that depicts how the graphene layers are affected by the Cu grain boundaries and the crack-like structure on the surface. The yellow arrows indicate the grain boundaries, and the square shows the cracks formed during the growth and cooling down process.

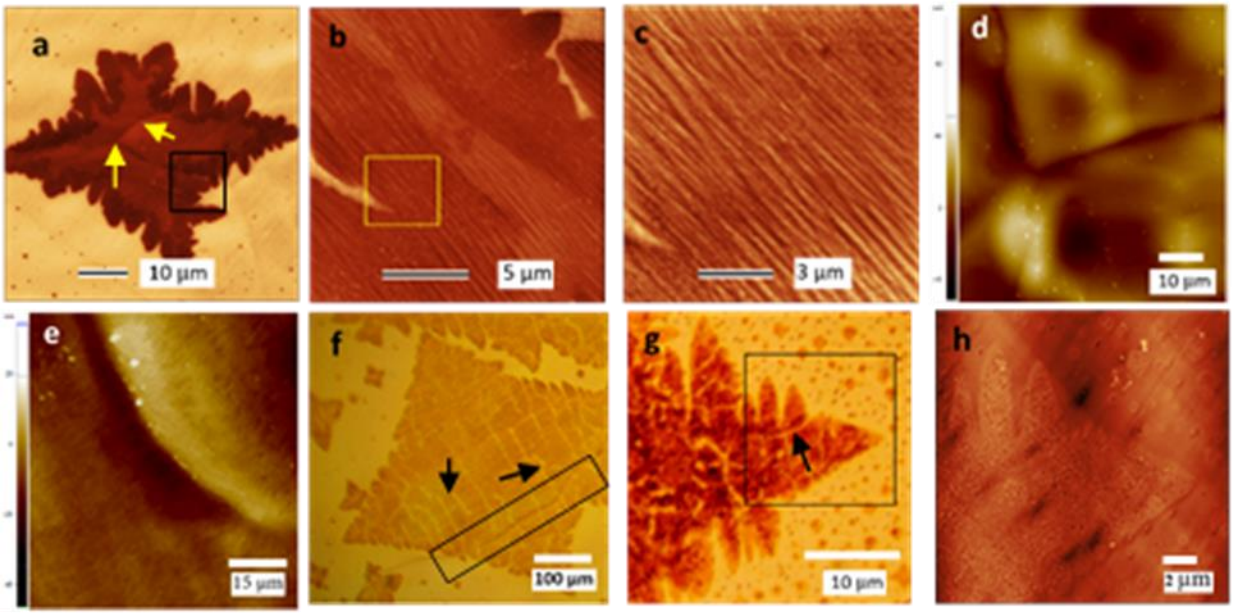

Figure 4.4 (a) An SEM image of a Cu grain boundary. The square shows fissures/cracks formed due to different thermal expansion coefficients. Arrows represent wrinkle formation due to Cu grain boundaries. (b-c) SEM images of Nano-scale wrinkles formed due to different thermal expansion coefficients of Cu and graphene. (d) An AFM image of a Cu grain boundary (before the graphene growth but after the annealing step) and valleys. (e) An AFM image of graphene (on Cu) wrinkle at a grain boundary. (f-g) OM images of graphene flakes ("f" represents a sample that used an electropolished Cu substrate & "g" for a non-electropolished Cu) with cracks and grain boundaries. Arrows show the cracks, and the rectangle shows the grain boundaries. (h) An AFM image of inset in Figure 4.4g. The arrow shows a crack, and this has been scanned using the AFM.

Figure 4.4(d & e) shows an AFM scan of a Cu grain boundary and a Graphene/Cu grain, respectively. This added surface area helps create nano/micro-scale wrinkles when transferring to a flat surface, as shown in Figure 4.3h. Figure 4.4(b & c) exhibit ripple-like structures, which are step edges formed by relaxation mechanisms of the bending energy of graphene. [302] If such wrinkled graphene is transferred onto a flat surface using a polymer transfer method, ripples will remain. Because ripple-valleys first contact the $SiO_2/p-Si$ surface and stick to the substrate due to the high adhesion between graphene and $SiO_2/p-Si$. It has also been reported that water drainage between graphene and the flat surface plays a crucial role in wrinkle formation. [303] We have also observed what looks like fissures or cracks formed due to thermal dilation of graphene

on Cu during the cooling down, which means that when the temperature is reduced under the minimum growth temperature for graphene, it is impossible to grow graphene further to eliminate those cracks. Such features have been observed in graphene grown on electropolished Cu (Figure 4.4f) and non-electropolished Cu (Figure 4.4g & h). In addition to that, we have noticed 4-fold graphene flakes on Cu instead of the most common 6-fold flakes. Esteban et al. (2013), [304] have discussed the reason behind these different shapes in detail. The graphene nucleation, which forms on the Cu (100) surface, exhibits square/rectangular shapes, while the nucleation form on Cu (111) exhibits hexagonal shapes.

4.4 Conclusion

We have aimed to grow single-crystal graphene by LPCVD using oxidized Cu foil enclosures as the catalyst substrate. In the process, we have observed large nucleation densities and surface defects on the unpolished Cu surface. We figured that the uneven Cu surfaces with defects could produce large nucleation densities based on the experimental observations. The graphene grown inside those defects helps create wrinkles when such material is transferred to a flat substrate. Besides, at a large nucleation density, the graphene flakes nucleated at different sites coalesced to produce poly-crystalline graphene. Due to such issues, we have implemented an electropolishing technique to smoothen the native surface of the copper foil.

Further, we have used oxidized Cu foil and enclosures produced from such foil to prevent Cu evaporation, reduce the nucleation density and the growth rate. The surface smoothening process has reduced the nucleation site formation while limiting the surface defects, which lead to wrinkle formation. The annealing process was also helpful to flatten the surface during the growth process further. Still, it has introduced Cu grains and associated boundaries, which are difficult to prevent due to the conditions related to the LPCVD method. We have also observed that graphene

grows across Cu grain boundaries and, in the process, produces an additional surface area for graphene growth, which later helps to create wrinkles. Cracks and ripple-like structures were also observed, which formed during the post-cooling down process due to different thermal expansion coefficients of graphene and Cu. We believe that the introduced electropolishing technique and the growth methods may be potentially helpful to synthesize better quality single-to-few layer graphene.

5 THE EFFECT OF MULTI-STEP CU SURFACE OXIDIZATION ON THE GROWTH OF SINGLE-CRYSTAL GRAPHENE BY LOW-PRESSURE CHEMICAL VAPOR DEPOSITION (LPCVD)

5.1 Introduction

Graphene is known as the 'wonder material,' a monolayer material that consists of sp^2-hybridized carbon atoms fit in a 2D hexagonal (honeycomb) lattice. More importantly, single-crystalline graphene has attracted vast attention due to its unique electrical, chemical, and physical characteristics, proving its potential as a suitable material for high-performance electronic device application, as discussed in chapter 4. Among various production methods of single-crystal graphene, the mechanical exfoliation of graphite layers is known as the best method to produce high-quality single crystals. However, the yield is minimal, and the cost for mass production is high; hence, that method is mainly limited to laboratory research and prototyping. The best way to produce low-cost and high-quality graphene is the LPCVD method. To use graphene in high-performance electronic and optoelectronic applications, it should have a single crystal structure. The single crystalline structure of graphene is highly dependent on the crystalline structure of the underlying copper layer. However, the industrial-grade Cu foils are polycrystalline and consist of carbon impurities and surface defects, leading to high nucleation density (ND). Higher graphene nucleation lead to form polycrystalline graphene layers, and ND should also keep at a minimum level, as discussed in section 4.1. In order to produce Cu foils with a single crystalline structure, Cu surface modifications and annealing in an inert gas environment should be implemented during the growth process. As mentioned in chapter 4, Cu surface oxidization help to suppress the nucleation density, and it was necessary to study the effect of oxidization on graphene nucleation density and graphene monolayer formation. According to Losurdo et al. (2011) [305], the presence

of high H_2 percentage increases the defects density and hence reducing the graphene quality. Because H_2 participates in creating defects such as point defects contains hybridized sp^3 C-H bonds. So, it was necessary to reduce the H_2 concentration without reducing the total pressure. Hence, a flow of N_2 was added to act as an inert gas and CH_4 flow was reduced to keep a high H_2: CH_4 ratio.

Thus, we will discuss the effect of multi-step copper surface oxidization followed by a complete vacuum (base pressure) step on suppressing the nucleation density. The surface-modified copper enclosures were used to create an isolated environment inside the pocket to enable a controlled growth environment. The graphene/copper foil was oxidized for visual enhancement of graphene flakes. The foils and the surrounding area were characterized using optical microscopy. Then a hybrid-transfer technique was developed to transfer graphene flakes onto a pre-determined location without wrinkles, surface residues, or impurities. The mechanism related to graphene growth is also discussed.

5.2 Experimental Methods

The experimental method of growing single-crystal monolayer graphene is consists of few steps such as copper surface modification, enclosure preparation, gas feed control, annealing, graphene growth, as-received graphene/Cu foil characterization just after the post-oxidation, graphene transfer, and the hybrid transfer of microscale 2-D materials (graphene), etc. All of these steps are discussed in detail under this section.

5.2.1 Copper surface modification and enclosure preparation

We have implemented a novel LPCVD method to grow single-crystal graphene monolayers on surface-modified ~25 μm-thick industrial-grade Cu foils and then study nucleation-density suppression by multi-step copper surface oxidization. The foils were cut into rectangular

shapes with dimensions of 7 cm x 5 cm. Initially, the foil surfaces showed an uneven color due to a pre-existing thin oil/grease layer on the Cu foil produced by the cold-roll-press method. Thus, the Cu foils were pre-cleaned in a 10% Acetic acid (CH_3COOH) solution for 1 min. After further cleaning the Cu foils with Acetone, Methanol, and Deionized water (2 min sonication time per step), they were air-dried with N_2. Then, it was placed on a hot plate and oxidized (pre-oxidation) for 40 min at $350 \pm 5\ C^0$ in the open air. An extended oxidization time was used since it was necessary to cover the copper surface with metal oxides uniformly. In the previous study, we discovered that the metal surface was not mainly covered by cupric oxide (CuO) when using an annealing duration of less than 40 min. After a careful study, the initial annealing temperature was determined, increasing the O (oxygen) ratio (Cu:O) of the metal oxides. A detailed explanation has been given in our previous work [1], and the same annealing time and temperature were used in the current study.

As mentioned, this pre-oxidation was performed to form a CuO layer which acts as a self-cleaning substrate and as a slow oxygen donor (as a result of CuO and residual Cu_2O decomposition) during the temperature ramping up step. [306] It is reported that the thermal decomposition of CuO occurs in two stages: Initially, CuO decomposes to Cu_2O and oxygen around $350\ C^0$ under a vacuum. Despite the stability of Cu_2O up to $1230\ C^0$ at atmospheric pressure, which is higher than the melting point of metallic copper, Cu_2O will decompose into O and Cu at high temperatures (below the melting point of Cu, but $\geq 1000\ C^0$) and low oxygen partial pressures. [306-309]

Then an enclosure is created by folding the Cu/oxide foil in half along the long side and then tightly crimping and folding the remaining edges. The inner spacing between two Cu foil layers was around 3 mm, and the inside was fully sealed from the outside due to tight crimping

and folding of three sides. It causes to cut off the external gas flow from directly entering the internal gas environment and will help form an internal static gas equilibrium during high temperatures, limiting the Cu evaporation. This step was adopted from our previous study, and it contains more details about the use of Cu enclosures. [1] In addition, it will act as a barrier between external and internal gas environments resulting in a decreased gas exchange rate with the external gas feed. It causes to have a low carbon presence during the growth process, further limiting the nucleation density.

5.2.2 Gas feed control, annealing, and graphene growth

After that, the enclosure was loaded into the CVD tube furnace (see Figure 5.1a). This LPCVD system (see Figure 5.2a) consists of a quartz tube with an inner diameter of ~3 cm, a heating element that can heat up till 1200^0C, a vacuum pump that can provide a base pressure (BP) value of around 30 mTorr and four gas inlets (see Figure 5.2b) that feed O_2, N_2, $H_2(10\%)/Ar(90\%)$, CH_4 (we have modified this gas inlet by adding a special needle valve which consists of a barrel-thimble micro-gauge as shown in Figure 5.2c. It was necessary to go below the minimum flow rate of the flow controller) into the chamber at different stages of the LPCVD process (See Figure 5.3). The sample was carefully placed in the middle section of the heating element to ensure a uniform temperature gradient across the pocket. Then the chamber was vacuumed and achieved a BP value of ~30 mTorr. After that, the system was pressurized to ~400 mTorr by feeding N_2 and H_2/Ar (80 sccm). Once the total pressure (TP) stabilized, the core temperature was ramped up to 900^0C and then gradually increased to the growth temperature of 1060^0C.

During this period, the TP value kept at nearly constant by slightly adjusting only the N_2 gas flow. After reaching the 1060^0C, the annealing step-I/in-situ oxygen passivation-I was

initiated while feeding a O_2 flow as shown in Figure 5.4 for 15 minutes (min). It increased the system pressure by ~10 mTorr (TP = 410 mTorr), and the temperature was constant during the time. At the end of this process, graphene growth (step I) was begun by turning off the O_2 flow while feeding a CH_4 flow at a rate of 10 sccm for 15 min (TP value increased to ~415 mTorr as shown in Figure 5.4).

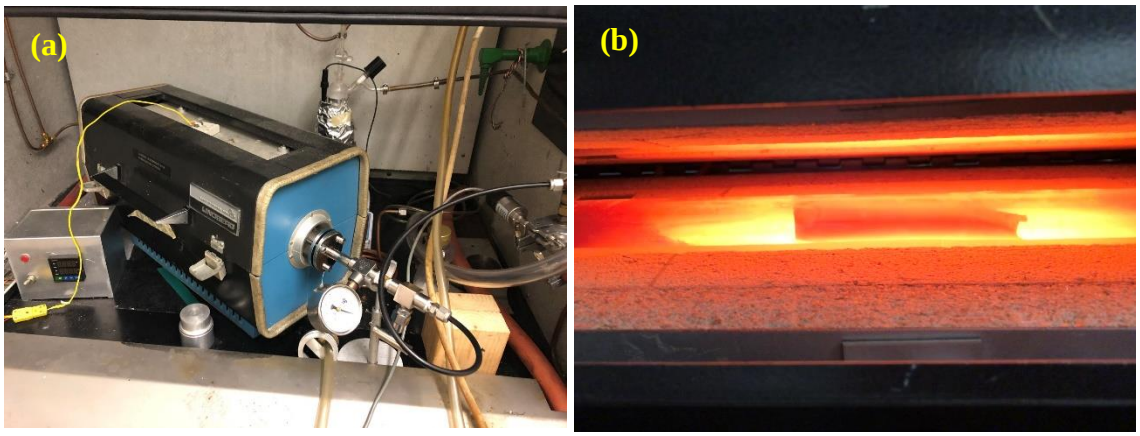

Figure 5.1 The LPCVD furnace. (a) The exterior of the furnace with the temperature controller and the thermocouple. (b) The inside of the furnace during the slow cooling phase.

At the end of the growth cycle-I, the system pressure was reduced and kept at ~30 mTorr (BP) for ~20 min by turning off all needle valves (the gas valves are illustrated as X in Figure 5.3). That removes most of the existing gases, by-products of initial graphene growth such as CH_x compounds, carbon residue, Cu vapor, etc. It will also act as a self-cleaning step that enables a cleaner Cu surface with less residue and carbon atoms, ensuring limited graphene nucleation sites. Later, the TP was brought to ~400 mTorr by feeding N_2 and H_2/Ar (80 sccm) and then initiated the annealing step-II/in-situ oxygen passivation-II by feeding a O_2 flow as previous for 15 min. That increased the TP value by ~10 mTorr, and then the TP value kept constant at ~410 mTorr. The graphene growth step-II was started just after turning off the O_2 flow, by feeding a CH_4 flow similar to the previous graphene growth step.

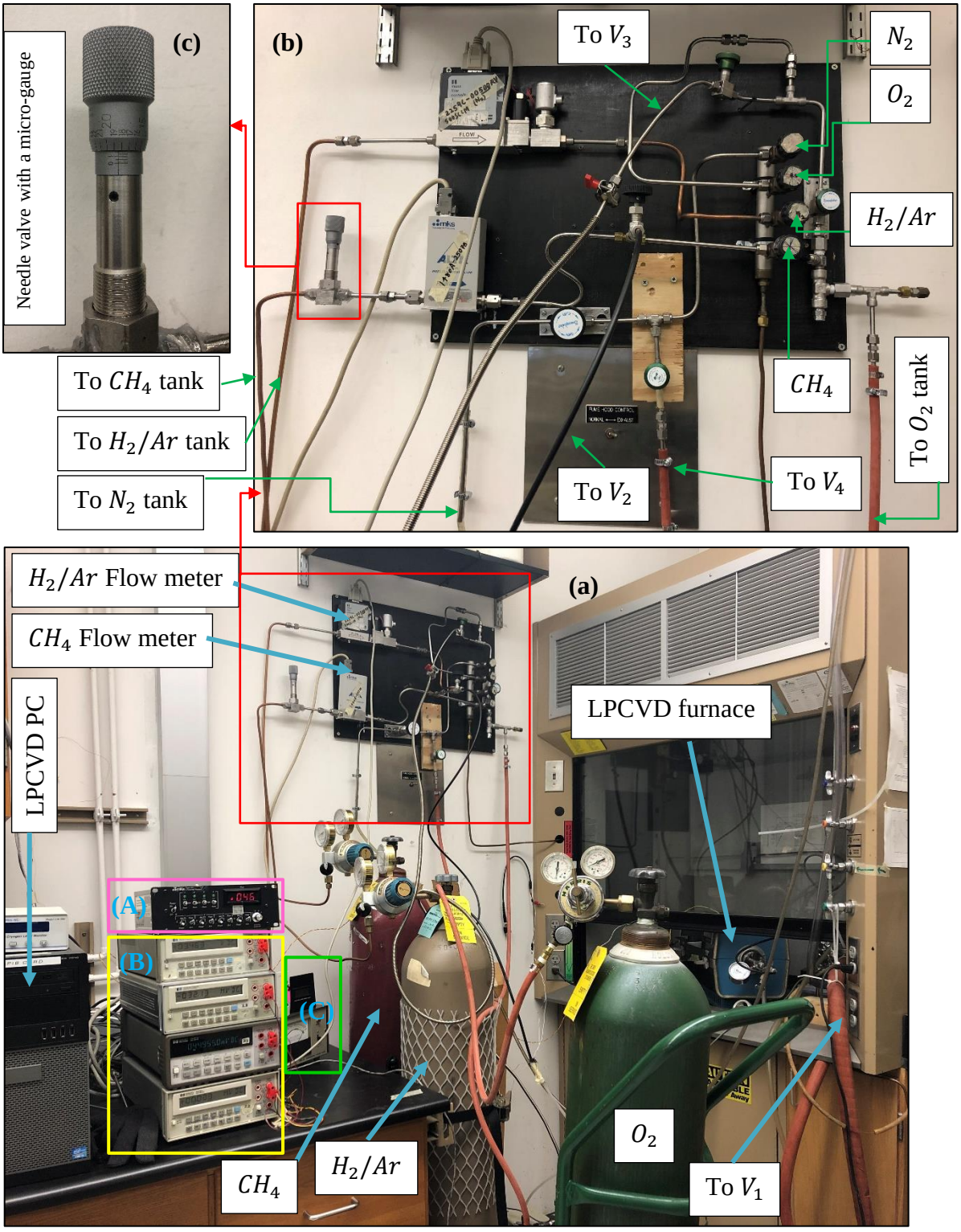

Figure 5.2 The modified LPCVD system. (a) The setup consists of four gas feeds controlled and monitored by two flow meters, few needle valves, and the LPCVD PC. The LPCVD system receives data from four digital multimeters (B), and the flow meters are controlled by a four-channel MKS digital readout (A). Here, V_1, V_2, V_3, and V_4 indicate four vacuum pumps. The pressure values are monitored by a multimeter-digital thermocouple vacuum gauge pair and analog pressure gauges (C). (b) The gas control panel. (c) The needle valve consists of a barrel-thimble micro-gauge. It was crucial to fine-tune the CH_4 gas flow.

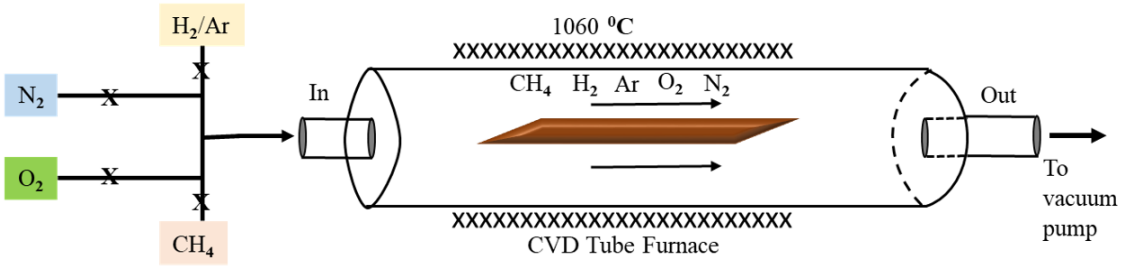

Figure 5.3 A schematic illustration of the LPCVD system. Four gas inlets feed O_2, N_2, $H_2(10\%)/Ar(90\%)$, CH_4 into the CVD tube furnace chamber at different stages of the LPCVD process. The inner diameter of the quartz tube was around 3cm, and the sample was placed in the middle of the heating element (isothermal zone) to ensure a uniform temperature along with the Cu pocket. Moreover, the enclosure was positioned carefully inside the quartz tube by considering the enclosure geometry and gas-phase dynamics to achieve a uniform reactant concentration and temperature. It helps to control the near-surface conditions so that the deposition becomes more homogenous and controllable. The maximum growth temperature of the reactor was 1060^0C and achieved a base pressure value of ~30 mTorr.

The temperature and pressure values were approximately identical to the growth step-I, as shown in Figure 5.4. The growth mechanism and gas-phase dynamics will be discussed in detail in the upcoming paragraphs in section 5.3 under Figure 5.9 and Figure 5.10. At the end of the growth, the temperature set value was immediately adjusted to the initial temperature (30^0C) and then let the system cool down slowly (see Figure 5.1b). Due to the immense difference between lab temperature and the core temperature, the system was rapidly cooled down until $\sim 900^0C$. So it further reduces the potential of more graphene growth and discourages the formation of new nucleation sites due to the stability of thin Cu_2O layer below 1000^0C (see the explanations given in Figure 5.9 and Figure 5.10 for more information). [306]

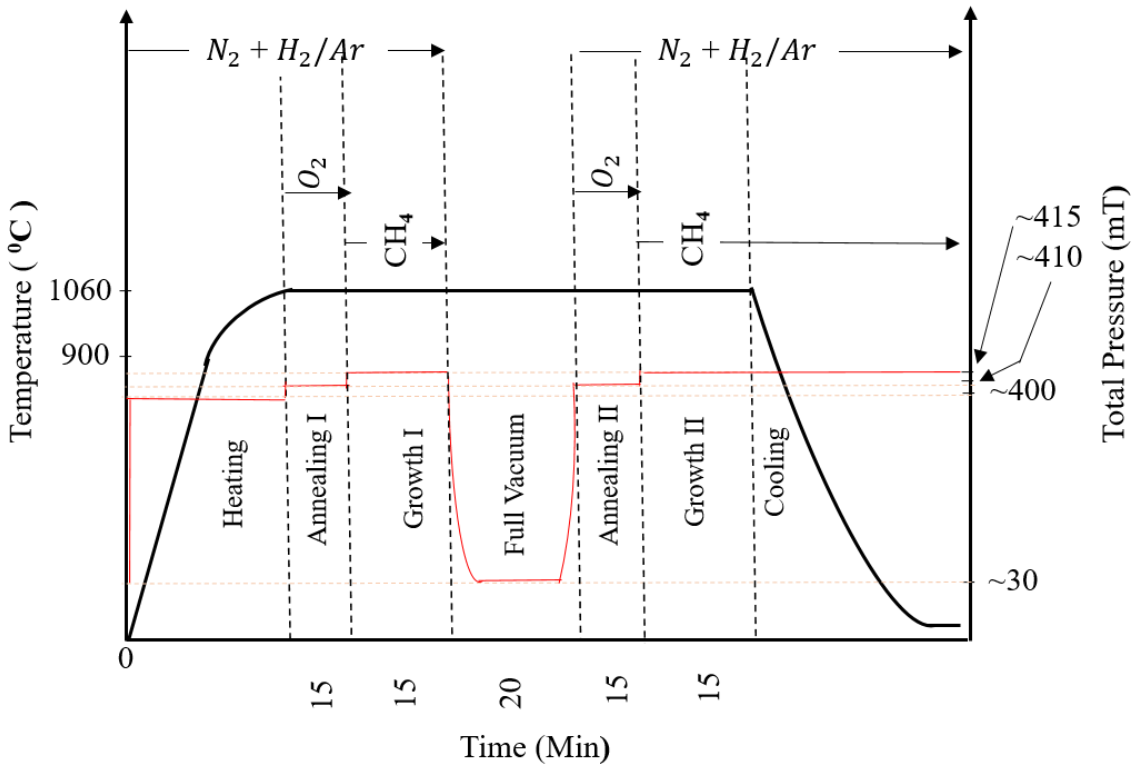

Figure 5.4 A graphical representation of the temperature (left-axis), pressure (right-axis), and the overall growth profile of the LPCVD process. The temperature (black curve) was ramped up to 900^0C *from* 30^0C *and then gradually brought to* 1060^0C*, as shown on the left axis. The red curve and the right axis represent how the pressure values changed during the entire growth process. This growth profile consists of seven stages, including two annealing and growth steps. In addition to the pre-oxidization step, the enclosure was oxidized twice during the LPCVD process by providing a controlled flow of* O_2 *before each growth cycle. It increases the concentration of oxygen atoms which helps to reduce graphene nucleation. At the end of the growth, the temperature set value was immediately adjusted to* 30^0C *and let the system cool down slowly while keeping the gas flow rates unchanged. The presence of oxygen atoms and the stability of* Cu_2O *below* 1000^0C*, discourage further growth of graphene during the cooling cycle.*

5.2.3 Characterization and Graphene Transfer

The graphene/copper enclosure was cut open from three sides and made flat without touching the middle. This precaution is necessary to prevent scratches, dents, and wrinkles on the graphene/Cu surface. The foil was loaded inside of a pre-heated oven to oxidize the foil at $\sim 110^0C$ for five min-per-side for optical visualization of individual graphene flakes (see Figure 5.11 and

Figure 5.12). After that, graphene flakes were visible to the naked eye due to their size (flake diameters/diagonal were between $50 - 800\ \mu m$), wide spacing between flakes, and the color contrast between copper oxide and graphene flakes. Then the Cu foil was placed under the OLYMPUS BH2-MJL optical microscope (OM) (see Figure 5.5a) and used x10 and x50 magnifications to analyze the foil further. The spacing between (edges) source (S) and drain (D) of the gold contact pattern was about $50 \pm 5\ \mu m$ (see Figure 5.7). Hence, to prevent short-circuiting the device, it was essential to choose graphene flakes with diameters/diagonals between 45 and 75 μm. Despite that requirement, the hybrid transfer technique discussed in the forthcoming paragraphs can transfer graphene flakes with diameters/diagonals over 75 μm. However, the photolithography and oxygen plasma etching methods should be applied to etch excess graphene when transferring larger flakes. The dimensions of the graphene flakes were measured using the ToupView software.

5.2.3.1 Hybrid Transfer of Microscale 2-D Materials onto a Predetermined Location (Gold Contact Pattern)

After selecting an area that contains a suitable flake, it was cut off from the rest of the foil. Any particle introduced during the post LPCVD process (this will not affect the inner surface characterizations) or dust particles deposited on the graphene/Cu surface during the post-oxidization step inside the oven should be carefully removed. The presence of such particles dramatically reduces the adhesion forces between PDMS and graphene, and hence the transfer will not be successful. Herein, the Cu/graphene piece was cleaned with a quick blow of N_2 gas.

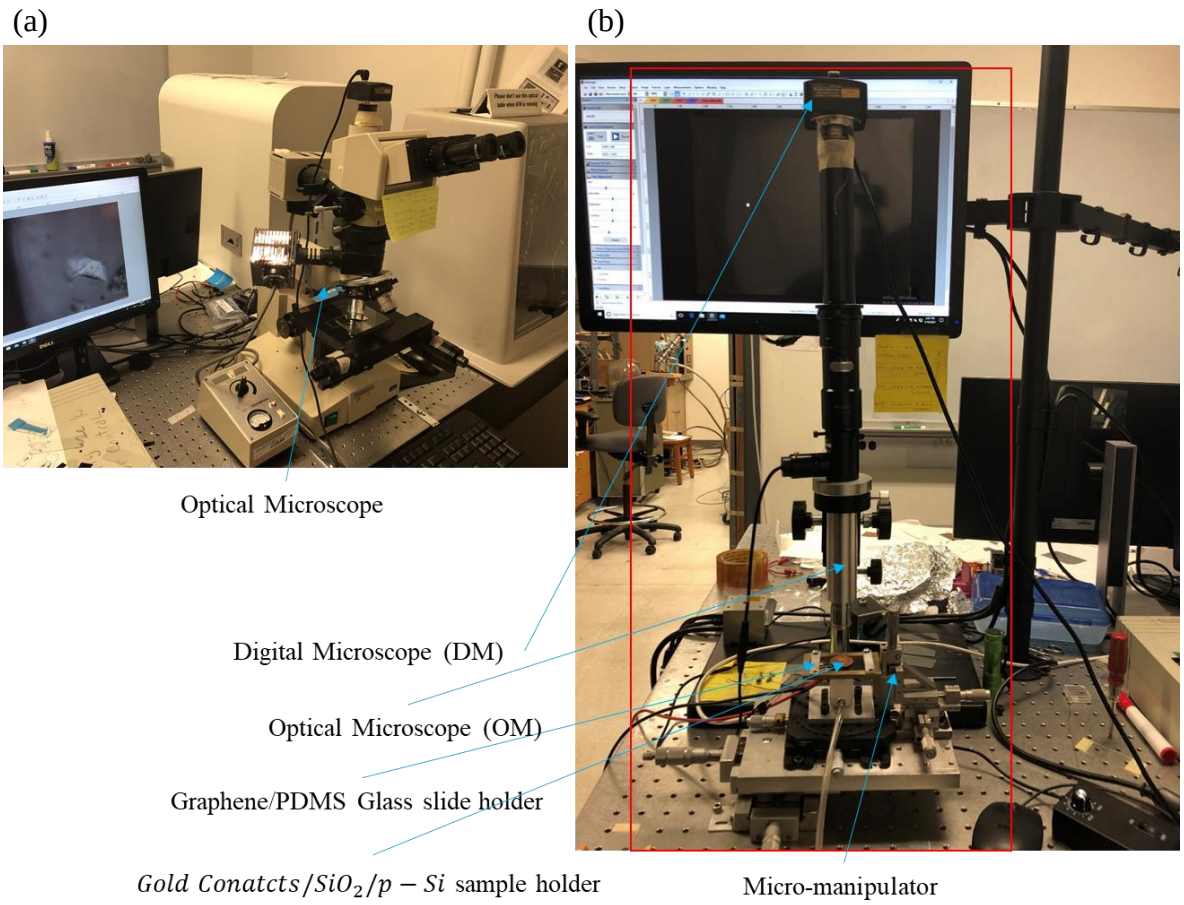

Figure 5.5 (a) An image of the OLYMPUS BH2-MJL Optical Microscope (OM) and this microscope can magnify images up to X100. The raw image is captured by a digital microscope camera (DM) that feeds it into an image viewer software. (b) A picture of the dry transfer system contains an optical microscope, a digital microscope camera, a micromanipulator, a glass slide holder, a heating element, a Si chip holder, and a vacuum pump. The Gold/SiO_2/Si chip holder was heated to $45 \pm 5^0 C$ to favor the van der Waals force between graphene and gold/SiO_2/Si chip as well as to weaken relatively strong adhesion forces between graphene and PDMS. The OM/DM system was used to capture the live image, and then adjustments were made to coincide the graphene sample and the contact pattern. The micromanipulator was used to move the graphene/PDMS/glass slide vertically and horizontally so that the graphene flake and the gold contact pattern touch each other.

Then a dust-free PDMS piece and the Cu/graphene piece were firmly pressed such that no air bubbles (blisters) were left between the layers. These blisters can also weaken the adhesion, and it is necessary to prevent those as much as possible. In addition, we noticed some graphene regions on the backside of the copper foil, and it was required to remove them to prevent defects.

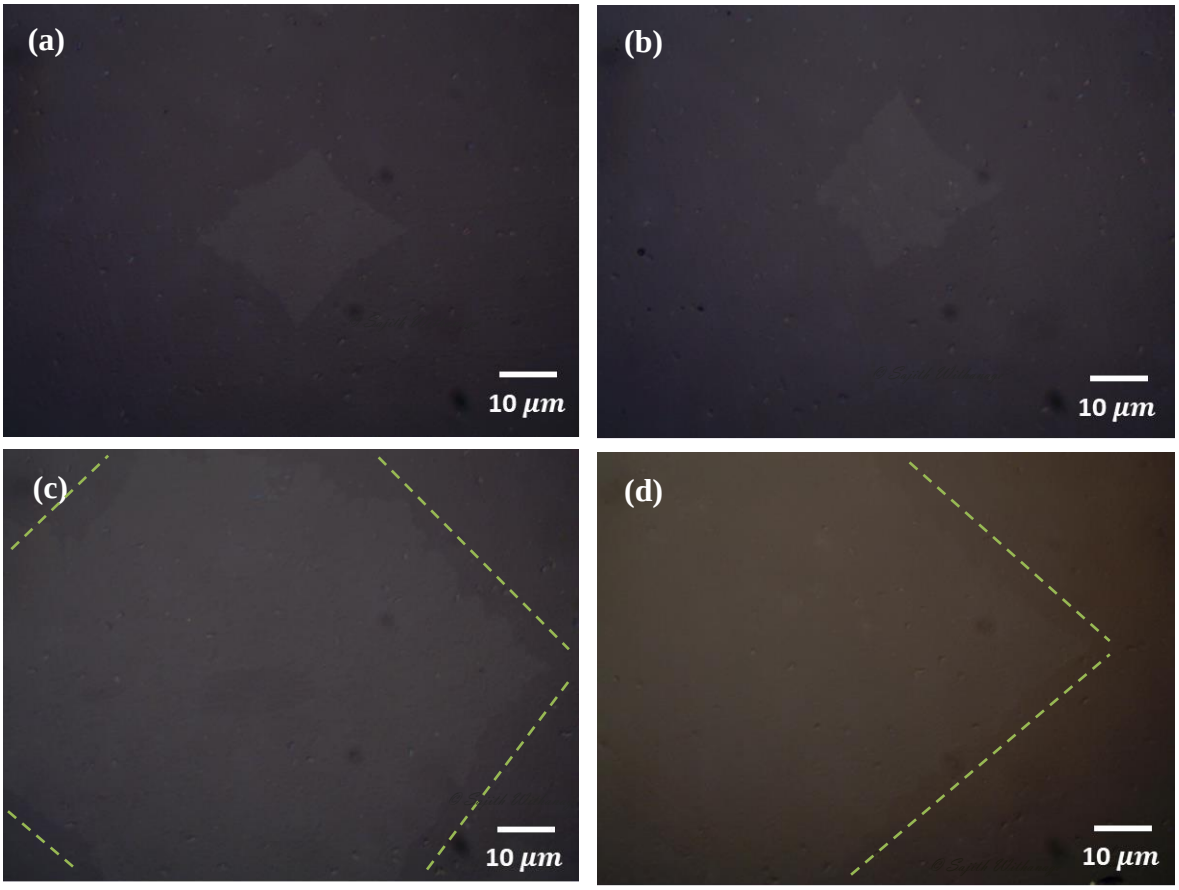

Figure 5.6 Optical images of individual graphene flakes on PDMS at X50 magnification (a & b) flakes with diagonal lengths around 45 ± 5 *μm (c & d) relatively larger graphene flakes with diagonal lengths over* 75 *μm. All of those flakes were clean, and the black dots were air bubbles trapped between glass and PDMS that do not affect the graphene transfer. These films were air-dried and free of water. The existing wet and dry transfer methods introduce polymer residue and impurities such as ions and water, affecting graphene quality negatively. More importantly, when using the PMMA wet transfer method, some water molecules were trapped between graphene and* SiO_2/Si *chip. That considered one of the significant drawbacks of wet transfer methods. However, in this method, the possibility of having such impurities and residue is very minimum. All flakes have a square shape, and green dashed lines mark the edges of graphene flakes.*

Hence, the backside was cleaned using an oxygen-plasma machine for ~180 s at 140 mTorr. Then the PDMS/graphene/Cu stack was let to float on a $FeCl_3$ solution to etch away the metallic copper (see Figure 5.7). At the end of the etching process, a tweezer was used to pick the PDMS/graphene stack carefully and left it to float on deionized water (such that the graphene side facedown) to dissolve remaining $FeCl_3$ without making any disturbances (so that water will not

leak between two layers). Then it was put on a glass slide (by forming a glass/PDMS/graphene stack) to air-dry and removed the excess PDMS using a scalpel blade.

However, before placing it on the dry transfer system (Figure 5.5b), the stack was examined using the OM to identify the areas where flakes are located and to assess the quality of each graphene flake, as shown in Figure 5.6. We tried the ×5 and ×10 magnifications first, but it was impossible to identify flakes due to the low contrast between graphene and PDMS. To solve this, we suggest using different colors as the lighting source or different angles. The only magnification that gave us a visible flake was ×50 and above due to the suitable contrast between the two layers. Here, Figure 5.6a & b shows flakes with diagonal lengths of $45 \pm 5\ \mu m$, and Figure 5.6c & d show relatively larger graphene flakes with diagonal measurements over $75\ \mu m$. Notably, all of those flakes and PDMS surfaces were free of any residue or contaminants. The black dots were air bubbles trapped between glass and PDMS, so it will not affect the graphene transfer. These films were air-dried in ambient laboratory air for longer hours and free of water. The existing wet and dry transfer methods introduce polymer residue such as PMMA, PPC, PVA, etc., and impurities such as ions and water molecules, affecting graphene quality negatively [310] due to the sensitiveness of graphene for the scattering caused by charged impurities. [311] Particularly, when using the PMMA wet transfer method, some water molecules were trapped between graphene and SiO_2/Si chip. The effects of trapped H_2O between graphene and SiO_2/Si interface has been reported elsewhere. [312, 313] Hence, this considers as one of the significant drawbacks of wet transfer methods. However, in the hybrid transfer method, the possibility of having such impurities and residue is very minimum. Typically, this stack is transparent, and it is challenging to locate graphene flakes under the optical microscope of the dry transfer system due to the low contrast between PDMS and graphene.

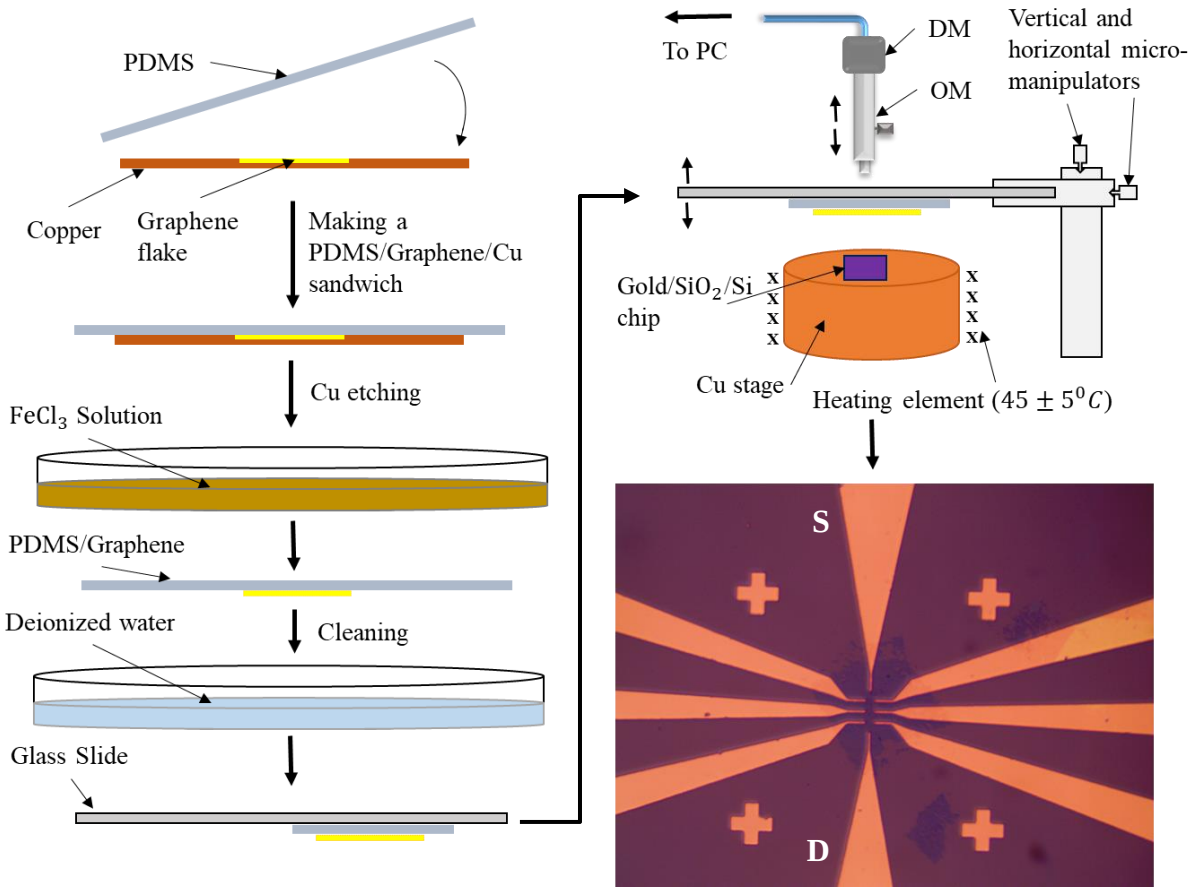

Figure 5.7 A schematic illustration of the hybrid transfer of graphene (2-D materials) onto a specific location on a flat and smooth substrate (here, a Si/SiO_2 chip with a golden contact pattern). It is crucial to pick a graphene flake that fits between the + signs of the gold contact pattern to prevent short-circuiting the device. First, the Cu/Graphene sample was cleaned with a quick blow of N_2 gas to remove any dust particles on the surface. Then a dust-free PDMS piece and the Graphene/Cu foil were firmly pressed such that no air bubbles (blisters) were left between the surfaces. It was let to float on a $FeCl_3$ solution to etch away the metallic copper. The PDMS/graphene stack was left to float on deionized water to dissolve the remaining $FeCl_3$ without making any disturbances so that water will not leak between two layers. Then it was placed on a glass slide (by forming a glass/PDMS/graphene stack) to dry and removed the excess PDMS. After that, it was placed on a micromanipulator such that the graphene side faces down. A cylindrical Cu block was used as the stage to hold the Si chip with a gold contact pattern, and the graphene flake was transferred onto it by using the micromanipulator. A heating element was used to heat (45 ± 5^0C) the Si chip to favor an easy transfer. This novel hybrid transfer method combines wet and dry transfer techniques. It was developed by taking advantage of weak van der Waals forces and relatively strong adhesion forces between graphene/PDMS interface.

Thus, once we picked a suitable flake, the surrounding area of the flake was carefully studied to identify some unique features on the surface so that we can use them to locate the graphene flake during the transfer step. Meanwhile, the cylindrical Cu stage of the dry transfer system was heated to 45 ± 5^0C using a heating element (see Figure 5.7).

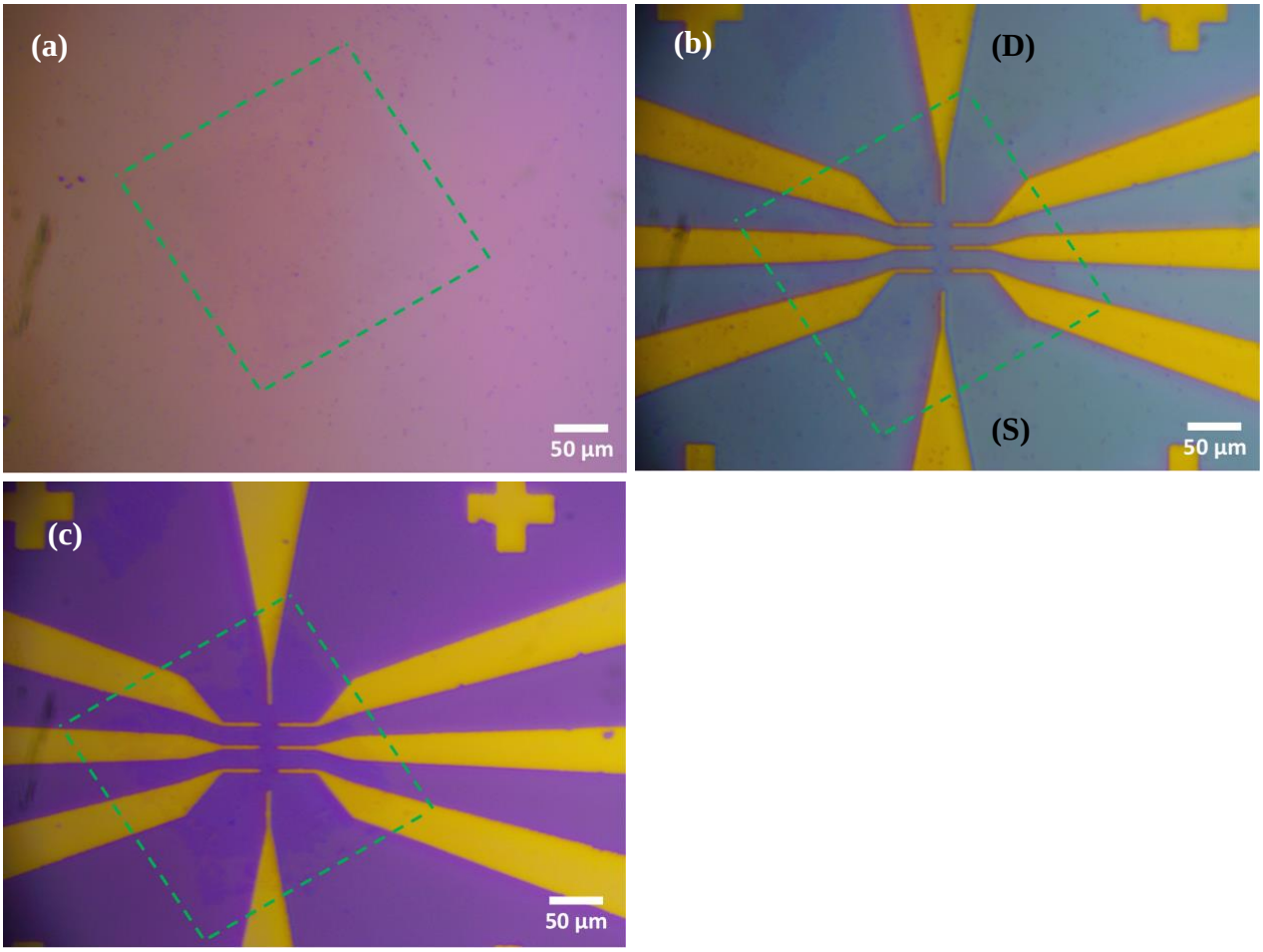

Figure 5.8 Optical microscopy images of the graphene flakes during different stages of the hybrid transfer process. (a) This is the same graphene flake shown in Figure 5.7. Here, the flake is on a PDMS piece/glass slide, and the pinkish purple color of the background came from the SiO_2/Si chip underneath. The surface has a minimal amount of residues which is negligible. Despite the low contrast between transparent graphene and PDMS, the flake is still visible that is enclosed by a dashed line (green). (b) The chip with a gold contact pattern, graphene flake, PDMS, and glass slide are touched together during the transfer of graphene flake from PDMS to Si chip. The bluish color without any bubbles confirms a good contact between the chip and the flake. (c) The graphene/gold/SiO_2/Si chip after the successful transfer of graphene without any residue taken after the PDMS liftoff.

Also, a clean SiO_2/Si chip with a gold contact pattern (see the right side of Figure 5.7) was placed in the oxygen-plasma chamber and treated for ~120 s at 140 mTorr. Then the chip was fixed on the Cu block using a vacuum and left to heat up till $\sim 45 \pm 5^0$C. After that, the graphene/PDMS/glass sandwich was placed on a micromanipulator such that the graphene side faces down (gold contact pattern faces up and graphene flake faces down). The key steps of the micromanipulator-assisted transfer method are as follows. Firstly, the flipped flake was located by looking at the live video feed of the stack and using the mentioned surface features (see Figure 5.8a). Secondly, the gold contact pattern was brought to the middle of the screen, and the stack was brought closer to the chip using the vertical micromanipulator (z-axis). Thirdly, the flake was positioned such that the gold pattern coincides with the middle of the flake using the horizontal micromanipulators (x- & y-axis). Thirdly, by using the z-axis manipulator knob, the graphene flake was moved downward until it firmly touches the gold$/SiO_2/Si$ surface (see Figure 5.8b) and left there for ~10 min to heat the PDMS/graphene interface to the same temperature as the Si-chip. Fourth, the PDMS/glass slide was lifted off such that the graphene flake is left on the gold contact pattern, as shown in the bottom right corner of Figure 5.7 and Figure 5.8c. Finally, the chip was carefully picked and stored in a dust-free environment. This transfer method combines wet and dry transfer techniques. It was developed by taking advantage of the weak van der Waals forces and relatively strong adhesion forces between graphene/PDMS interface. The initial studies of this work were presented and published in 2020. [3]

5.3 Results and Discussion

It has been shown that the effect of multi-step oxygen annealing of clean industrial-grade copper foil enclosures followed by a full-vacuum on nucleation density suppression. Additionally, we introduced N_2 as the main inert gas (additional to Ar) for the LPCVD growth of single-layer

graphene flakes. Here, H_2 act as a reduction gas and CH_4 as the carbonaceous gas. According to Losurdo et al. (2011), the presence of high H_2 percentage increases the defects density and hence reducing the graphene quality. Because H_2 participates in creating defects such as point defects contains hybridized sp^3 C-H bonds. [305] To solve this issue, a lower flow rate of H_2/Ar could be used but it causes to decrease the total pressure (TP) of the system. We have noticed that the very low total pressures reduce the growth rate of graphene flakes and increase the nucleation density. A similar result supporting our observation has already been reported elsewhere [314], and it was crucial to find a way to keep the TP value over 350 mTorr.

Nitrogen is the most abundant gas in the Earth's atmosphere (78%), and due to its chemical structure, it has similar properties to a noble gas. However, the widely used inert gas in the CVD growth of graphene is Ar (0.9%) but N_2 is 88 times more abundant compared to Ar. So, producing a pound of Ar requires 88 times more energy than the energy needs to make the same amount of N_2. Also, the production and distribution of Ar increased the carbon footprint, and Ar is more expensive than nitrogen. But, liquid N_2 is readily available in almost every laboratory and has various uses in many areas, such as cryogenic experiments. Moreno-Bárcenas et al. (2018) has reported the use of N_2 as an inert gas with a combination of C_2H_2 (carbonaceous gas) and N_2 (reduction gas) to grow graphene on Cu foils using the CVD method. [315] Xue et al. (2019) has grown graphene on liquid copper ($1083^0 - 1400^0C$) using the APCVD technique with a gas mixture of CH_4, H_2 and either Ar or N_2 as the carrier gas. [316] Moreover, no nitrogen doping has been reported in either publication since those studies have not involved in steps that ionize N_2 or free of highly reactive radicals. However, Komissarov et al. (2017) has observed N-doping during the APCVD process and produced twisted graphene on copper. They have used n-decane ($CH_3(CH_2)_8CH_3$), H_2 and N_2 as a carbonaceous gas, a reduction gas, and a carrier gas,

respectively. n-Decane is an n-alkane, and it forms highly reactive chains of radicals during the high-temperature thermal decomposition. That stimulates various reactions that promote nitrogen-doping. [317] In this current study, we have used CH_4, H_2/Ar, O_2 (for oxidation of Cu) and N_2 (inert/carrier gas) to grow graphene flakes with the LPCVD method at 1060^0C (below the melting point of Cu).

The graphene growth was initiated, as discussed in section 5.2.2. Once the copper enclosure was inserted into the quartz chamber, the system was vacuumed such that the base pressure reaches ~30 mTorr. Then a flow of N_2 and H_2/Ar was introduced into the chamber so that the total pressure increased to ~400 mTorr. The LPCVD growth mechanism until the end of the growth cycle-I is represented in Figure 5.9, and the process until the growth cycle-II is illustrated in Figure 5.10. Figure 5.9a represents the side view of the copper enclosure made of ~25 μm thick pre-oxidized Cu foil. At this stage, the gaseous system consists of nitrogen, argon, and hydrogen. The light brown blocks represent the Cu foils containing a small percentage of carbon atoms on the surface and inside the foil and are indicated by gray-colored dots.

To increase the surface oxygen percentage, we have pre-annealed/oxidized the copper foil in open-air on a hot plate, and it has formed a thick oxide layer on each side of the foil, which is represented by dark brown color. The thick black arrows on the top and bottom, pointing to the right-hand direction, indicate the gas flow direction (towards the vacuum pump). The tightly folded edges are welded together during the heating phase due to the high temperature (1060^0C) that is closer to the meting point of Cu. It seals the interior of the pocket from the outside and later forms a static equilibrium inside the pocket. Those welded pocket edges are represented by thick black lines on the left and right of Figure 5.9a. The mechanism for top and bottom copper foils are pretty similar, and only the top section was used starting from Figure 5.9b.

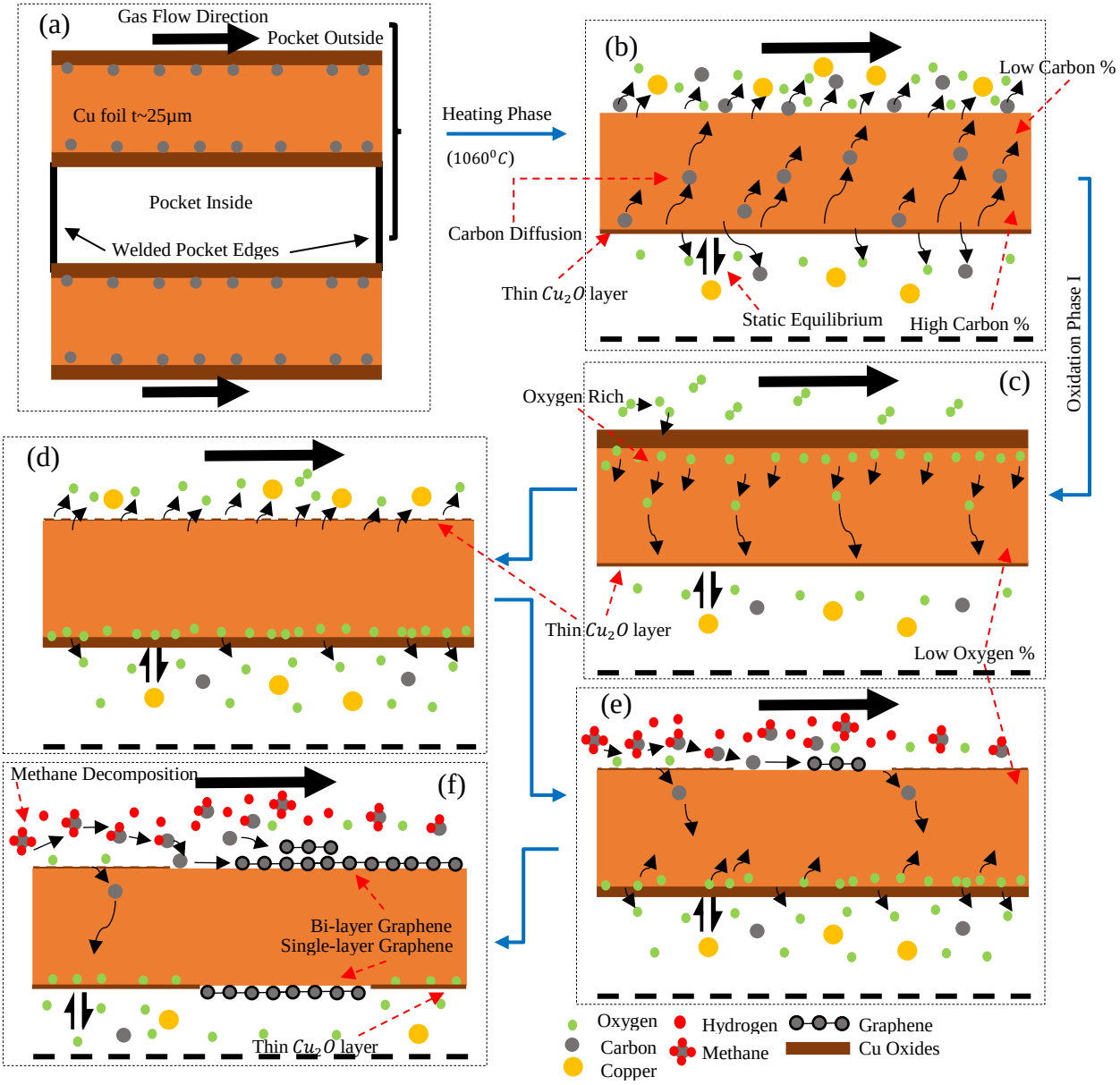

Figure 5.9 A schematic representation of the graphene growth mechanism inside and outside the Cu enclosure during the growth cycle-I. (a) Side view of the copper enclosure that is made of ~25 µm thick pre-oxidized Cu foil. The main gas flow includes N_2 and H_2/Ar. The tightly folded edges are welded together during the heating phase due to the high temperature (1060^0C) closer to the meting point of Cu. It seals the interior of the pocket from the outside and forms a static equilibrium inside the pocket. (b) The evaporation and diffusion mechanisms of carbon atoms in bulk and on the surface of copper foil before the oxidation step-I. The inner oxide layer is decomposed and formed a thin Cu_2O layer. (c) The oxidation step-I of copper and oxygen diffusion into the copper foil. (d) The oxygen evaporation on the outer layer and the oxide formation of a relatively oxygen-rich pocket interior. (e) Growth cycle-I. The mass transport, gas diffusion, surface adsorption, dehydrogenation/decomposition, surface migration & nucleation, growth of graphene islands, bulk diffusion of carbon into the Cu foil, and oxygen diffusion from the interior to the exterior. (f) Monolayer flakes are formed inside the pocket and prevent the formation of bi-layers by acting as a diffusion barrier for carbon. The mechanism of bi-layer graphene formation on the exterior of the enclosure results from free radical deposition on the existing graphene flakes from the exterior gas environment.

The pocket's exterior is exposed to a highly reducing gas environment, and hence the surface evaporation rates increases. So, at high temperatures, the outer oxide layer (mainly CuO) decomposes to Cu_2O and then to oxygen atoms (green dots). Then evaporates from the metal surface, as shown in Figure 5.9b. Also, some of them combine with hydrogen atoms before being moved out from the reactor. The self-cleaning mechanism [306] triggered by the presence of oxygen atoms removes the carbon atoms on the outer layer of the Cu foil, and the high evaporation conditions evaporate Cu atoms on the exterior. It exposes some of the carbon atoms trapped inside the copper foil and encourages more carbon atoms to evaporate with the help of oxygen atoms. That creates a cleaner outer surface with a minimal carbon percentage. Simultaneously, the inner surface oxides of the enclosure start to decompose, and also the carbon and Cu atoms. However, the inside environment is sealed from the outside, and it causes Cu atoms to form a static equilibrium. Also, the carbon evaporation and oxygen decomposition rates decrease, creating oxygen and carbon-rich inner surface relative to the exterior surface. These excess oxygen atoms form a slowly decomposing thin Cu_2O layer (see section 5.2.1). Also, some of the oxygen atoms together with carbon atoms start to diffuse from the interior to the exterior through the copper grain boundaries and surface defects such as cold-rolling striations and valleys or pits. Then the carbon atoms evaporate from the exterior surface (oxygen-assisted self-cleaning), and the carbon percentage of the foil enclosure reduces to a fraction. Additionally, this high temperature, which is closer to the melting point, rearranges the Cu surface and creates a smoother texture. Furthermore, the defects and carbon-free copper surface reduce the chance that these sites act as early nucleation sites.

Then the in situ oxidation phase-I is initiated by introducing a flow of O_2 as shown in Figure 5.9c. That forms a thick layer of CuO on the copper surface and creates an oxygen-rich

exterior. Then oxygen atoms diffuse from the exterior to the interior through surface defects and grain boundaries. Those oxygen atoms increase the metal oxide thickness by forming more oxides. At the end of the oxidation phase-I, the external oxygen supply is turned off. Some oxygen atoms evaporate into the gaseous environment inside the pocket during the decomposition of metal oxides (see Figure 5.9d). However, the inner surface oxides which formed during the oxidation phase-I partially decomposed into a thin Cu_2O layer and oxygen atoms. This saturates the inner surface with oxygen and starts to decompose at a slow rate. On the other hand, the exterior environment stimulates high oxide decomposition (into a thin layer of Cu_2O and oxygen atoms) and copper evaporation rates. This increased Cu evaporation rate prevents Cu_2O from covering the entire outer surface. So it exposes some regions of the Cu foil exterior to carbon precursor, which is CH_4 as shown in Figure 5.9e. The mechanism and equations related to the growth kinetics of graphene on transition metal substrate have already been discussed in section 3.3.2.3. The initial graphene growth starts on the carbon-rich outer surface. And then, some of the carbon atoms diffuse into the Cu foil via grain boundaries and defects, as shown in Figure 5.9e. The inner surface contains a high concentration of oxygen atoms compared to the outer shell, which forms a large area of oxide (Cu_2O) layer. That highly limits the exposure of possible nucleation sites to carbon atoms and actively cleans the formed nucleation with the help of oxygen atoms. However the Cu_2O layer slowly decomposes to oxygen atoms, and some of it diffuses to the exterior surface. That forms some patches on the interior oxide layer and triggers limited graphene nucleation. The graphene flake covers the area which free of Cu_2O and it further grows when the oxide layer decays further. More importantly, these graphene monolayers act as a diffusion barrier to carbon atoms, and it prevents the growth of graphene bi-layers on the interior. [318]

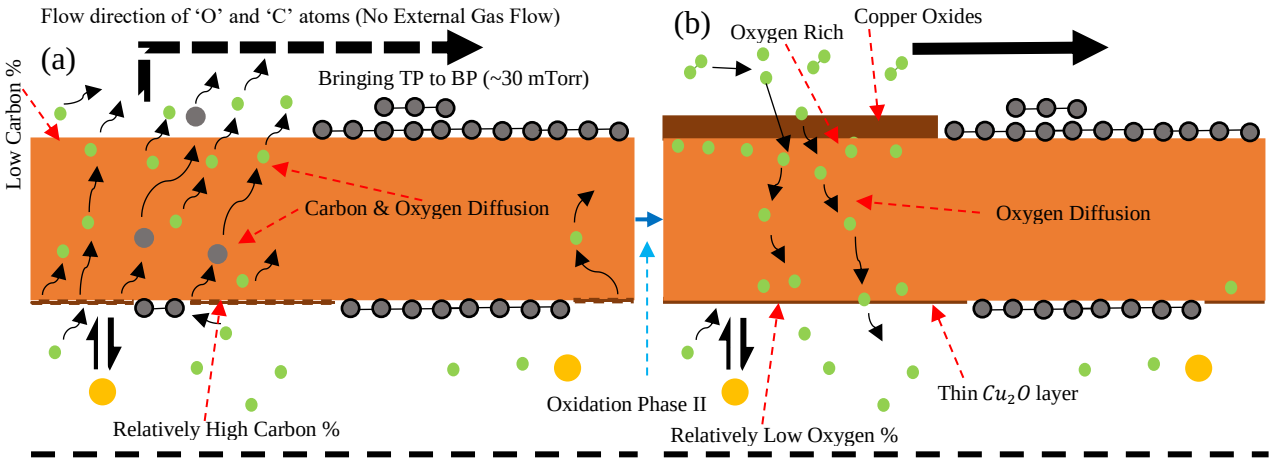

Figure 5.10 A schematic representation of the full vacuum phase and oxidation phase-II before the growth cycle-II. (a) The full vacuum step. After shutting down the gas supplies, the system pressure starts to drop rapidly, and the rate of surface evaporation on the exterior is increased. It causes to decrease in the carbon atom percentage on the outer surface of the Cu foil. The interior is in static equilibrium, which encourages the diffusion of carbon and oxygen towards the exterior. It removes the additional nucleation sites and carbon on the inside surface and helps to suppress the nucleation density as a result. (b) Oxidation phase-II. At the end of the vacuum step, the carbon-free Cu surfaces oxidized by following the same steps as previous. This step is similar to part (c) of Figure 5.9 despite the graphene layers formed during the growth cycle-I. After this, the growth process is identical to the growth cycle-I (see Figure 5.9c-f).

But the exterior environment is rich with free radicals such as carbon and C_xH_y. It encourages graphene bi-layer growth on top of the previously grown graphene layers, as shown in Figure 5.9f. At the end of the growth cycle-I, the system vacuumed thoroughly (~30 mTorr) by shutting down all gas supplies. The purpose of this step was to remove unwanted leftovers that were produced during the growth cycle. The mechanism that undergoes during the vacuum step and the second oxidation phase is illustrated in Figure 5.10. As a consequence of the high temperature and zero external oxygen flow, the residual Cu_2O layer starts to decompose, as shown in Figure 5.10a. It exposes the Cu surface and begins to evaporate Cu atoms and carbon atoms due to the favorable conditions inside the reactor. These remaining atoms and particles, such as residual carbon atoms, active radicals that are lightly attached to the Cu surface, oxygen, and Cu atoms, are

removed from the reactor by the vacuum pump. Meanwhile the inner Cu_2O layer slowly decomposes and releases oxygen atoms into the system. This inner layer is oxygen-rich compared to the exterior surface, and oxygen atoms on the interior surface diffuse towards the outer shell. Also, the free carbon atoms on the inner surface diffuse towards the exterior and are then cleaned out with the help of oxygen atoms on the outer surface, as explained in the previous section (see Figure 5.9b & Figure 5.10a). This mechanism helps to etch out small graphene nucleation on the inner surface. So it further suppresses the nucleation density on the inner surface and prepares the outer surface for the next growth cycle by making the surface free of carbon atoms. The oxidation phase-II is initiated at the end of the vacuum period, as shown in Figure 5.10b. The mechanism related to this step is similar to oxidation phase-I (see Figure 5.9c), and the only noticeable difference is that the surface contains some graphene coverage. The diffused oxygen atoms contribute to the inner Cu_2O layer by increasing the oxide thickness. The mechanism after this step is identical to the explanations given in Figure 5.9d-f.

The optical microscopy images of oxidized (see section 6.2.3) graphene/Cu foils were taken immediately after the post oxidation, which was performed to enhance the graphene flakes visually. All images are shown in Figure 5.11 and Figure 5.12 taken by scanning the interior surface under different magnification values such as ×5, ×10, and ×50. Because of the larger sizes of most flakes, the ×5 were used to capture complete flakes for most scans. Moreover, single graphene flakes with dimensions closer to 1 millimeter were visible to the naked eye. In this chapter, we have included images that belong to three samples. The first two samples were included in Figure 5.11, and the third was included in Figure 5.12. All three samples were grown under the same parameters, which were discussed in the previous sections. Interestingly, all samples show similar characteristics and have a low nucleation density (avg. ~5 nucleations/cm^2)

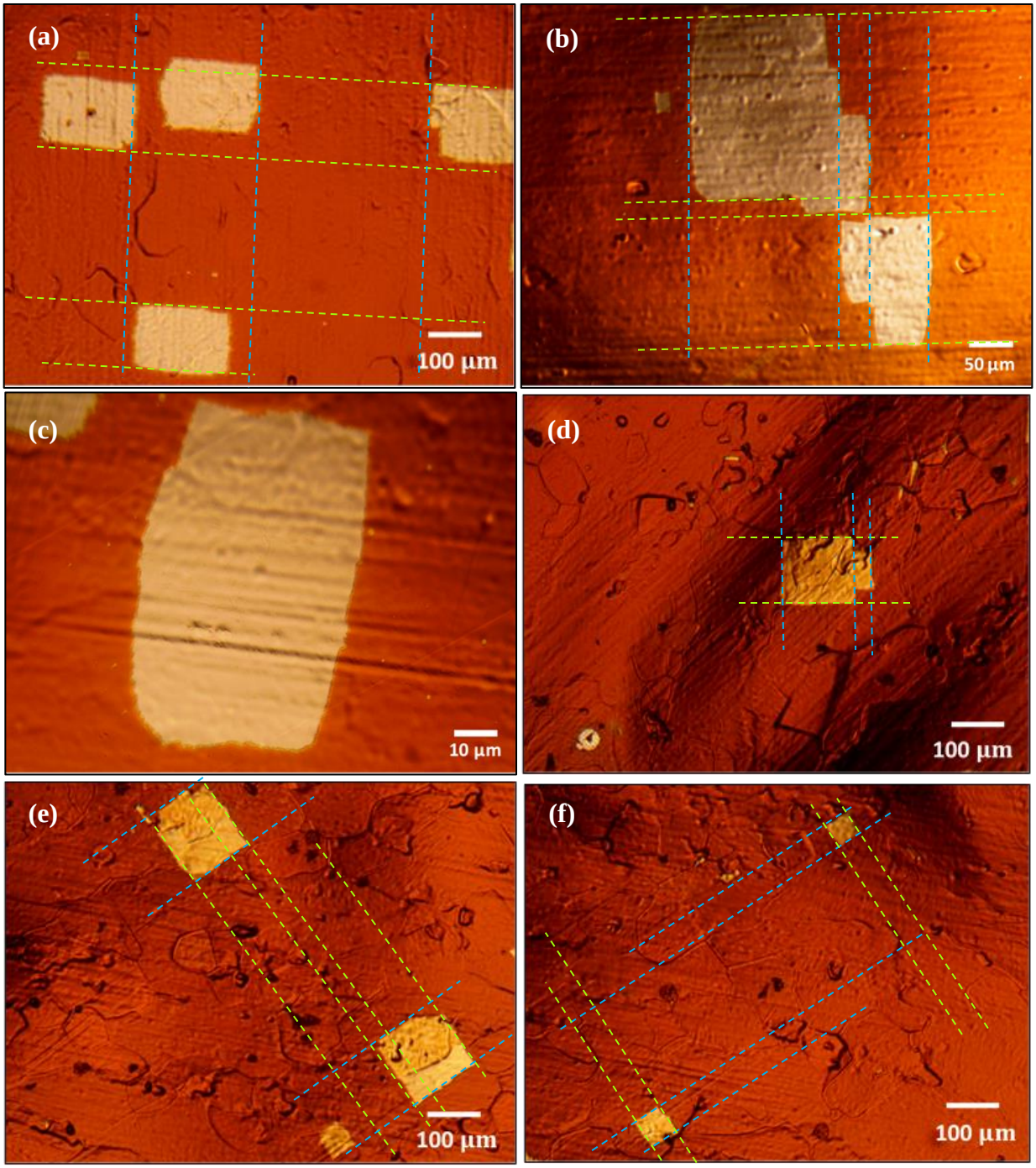

Figure 5.11 The optical microscopy images of graphene flakes grown on Cu. This figure includes images that were taken from two samples. Figure 5.12a-b shows another sample grown under the same conditions. All samples showed similar characteristics. The first sample was scanned under different magnifications to study the surface conditions of graphene and Cu. (a-c) OM images of sample 1, taken under different magnifications (a) ×5 (b) ×10 (c) ×50 (d-f) OM images of sample 2, taken under ×5 magnification at different locations on the interior surface. All sample surfaces were clean of residue and smooth, which was uncommon under different growth methods. More importantly, all samples have a very low nucleation density. The chartreuse & blue lines shows the alignment between flakes, and it will be discussed in Figure 5.12. Such features prove the higher quality of the graphene samples.

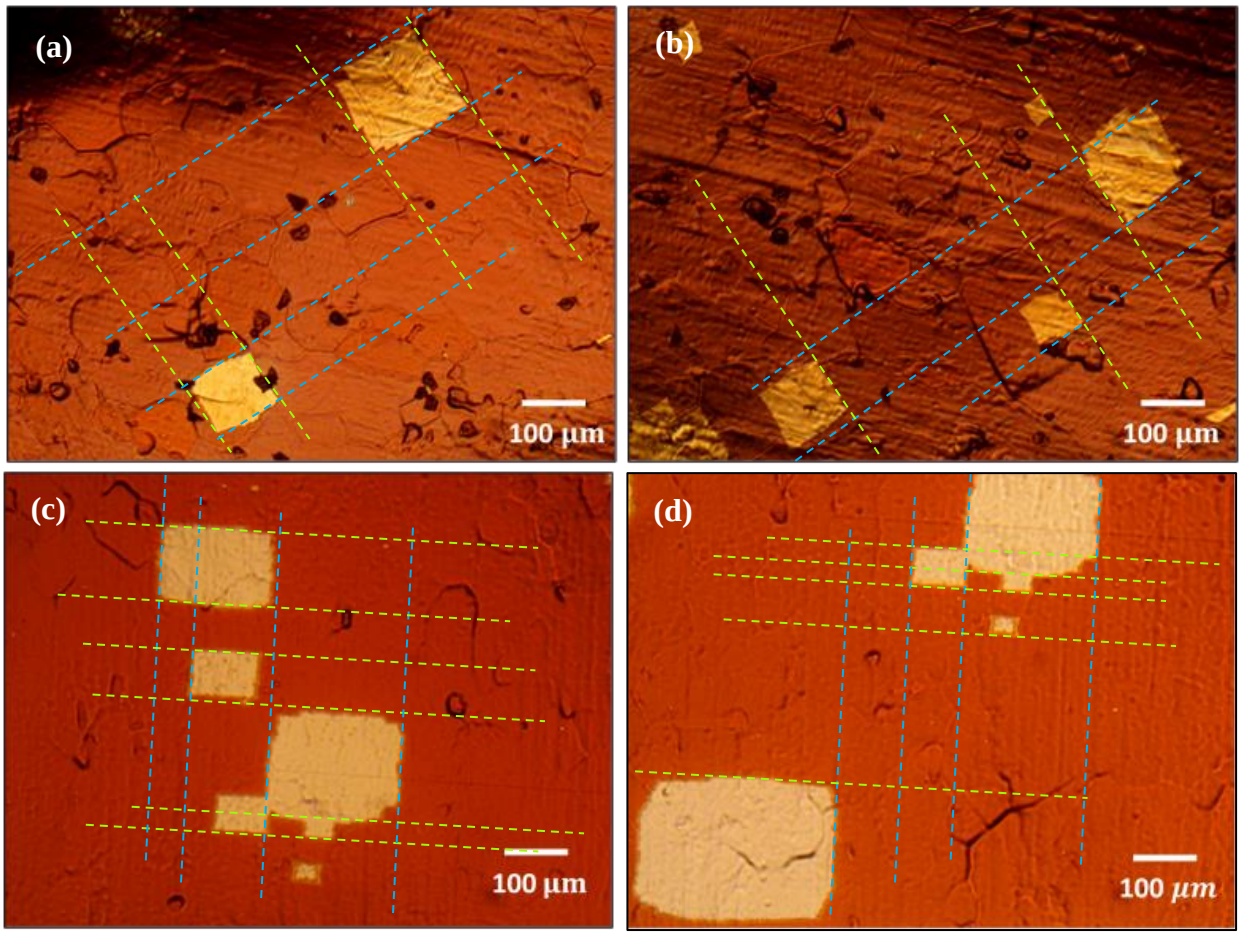

Figure 5.12 (a & b) Optical microscopy images of graphene flakes and the surrounding area of sample 3. The images were taken under ×5 magnification and had a cleaner surface with a highly suppressed nucleation density. (c & d) Surface scans of two adjacent locations on sample 1 (see Figure 5.11a-c). These were also taken under ×5 magnification as Figure 5.11a. Both (c) and (d) show smooth surfaces and low nucleation densities, as shown in Figure 5.11a-c. Additionally, the flakes grown under this method are square-shaped and followed a vertical and horizontal alignment. It also follows this alignment when combining flakes and then creates a big square-shaped graphene flake. The chartreuse & blue lines show such alignments, representing the high crystallinity of the foil, which consists of Cu (100).

-compared to the previously reported minimum value, ten nucleations/cm^2 which was obtained using copper enclosures. [318] Three images (Figure 5.11a-c) were added to discuss the surface quality and nucleation sites captured under magnifications of ×5, ×10, and ×50. All three surfaces are free of micro/nanoscale graphene islands and carbon or metal residue, as shown in Figure

5.11a-c. Here, achieving such clean surfaces with such a low ND was possible due to the self-cleaning mechanism explained in the paragraphs belongs to Figure 5.9 and Figure 5.10.

Another attractive characteristic of these graphene samples is the square shape of the flakes. We have observed this unique shape in all graphene samples grown with these growth parameters. Jacobberger and Arnold (2013) have reported that the square-shaped graphene morphology is influenced by the crystallographic orientation of Cu (100). [319] So, the graphene flake orientation, dendrite growth directions, and flake morphology are heavily based on the Cu lattice underneath. Hence, the observed square shapes, which resulted by Cu (100), emphasize the symmetry of the Cu lattice underneath the graphene flakes. The flakes of all sizes have this unique shape, and when combining, they create larger squares by giving evidence for their fractal nature. Moreover, all flakes show a vertical and horizontal alignment between multiple graphene flakes, as shown by blue & chartreuse-colored lines, respectively in Figure 5.11 and Figure 5.12. It confirms that the dendrites follow a growth direction <100>, concerning the Cu lattice on the bottom. Since we observed these characteristics everywhere on each sample, as shown in Figure 5.11 and Figure 5.12, we can conclude that these Cu samples (graphene/Cu) are highly symmetric and have a uniform crystalline structure. Hence, graphene flakes grown by this method have a single crystal nature which is grown by following the underlying Cu lattice. Additionally, the flakes have smoother and planar edges, as shown in Figure 5.11 and Figure 5.12, which is resulted from the high $H_2 : CH_4$ ratio. [319] The initial studies of this work were presented and published in 2019. [2]

5.4 Conclusion

In this work, we have studied two areas. Firstly, we focused on the effect of multi-step copper surface oxidation followed by a complete vacuum stage (during the LPCVD growth of single graphene crystals on surface-modified copper enclosures) on suppressing the nucleation density (ND). The impact of such surface modification was explored in our previous works. Secondly, we have developed a hybrid transfer technique to transfer grown graphene flakes without wrinkles and residue or impurities. The graphene growth consisted of two growth cycles, and the focus was given to the self-cleaning mechanism during the pre- and post- oxidation and the complete vacuum phase. We found that the tightly folded edges weld together after the temperature ramp, creating an isolated environment inside the pocket. It formed a static equilibrium inside the enclosure, and that was helpful to suppress the ND and obtain monolayers. The pre- and in situ oxidization were helpful to achieve carbon-free (fractional carbon percentage) copper foil surfaces that further reduces the nucleation density due to the "self-cleaning" nature of oxygen. The complete vacuum phase also contributed to the surface cleaning mechanism triggered by the surface atom evaporation under high temperatures and high vacuum. The clean copper surfaces reduce the number of impurities which can act as nucleation sites. So, cleaner catalyst surfaces lower the ND further. These multi-step oxygen annealing and vacuum phases have restructured the Cu lattice to create Cu (100) and enhanced the symmetry. Additionally, the surfaces have become smoother than the previous studies and hence contributed to the ND limitation. The CuO initially dissociate into a Cu_2O layer. We have observed four critical roles associated with cuprous oxide, which later contribute to the ND suppression: acting as a slow oxygen releasing agent, helping to clean and restructure the Cu foil, form a static equilibrium inside the pocket, and act as a carbon diffusion barrier at the inner copper surface. The graphene flakes that grew on the interior surface act as a

carbon diffusion barrier, preventing any double-layer formation. On the other hand, the exterior environment contains free radicals, and those can be deposited on existing graphene layers, forming a bi-layer. The graphene flakes were square-shaped and aligned in directions perpendicular to each other, reflecting the copper lattice/Cu (100) symmetry underneath the graphene layers. Such characteristics were observed in every sample. So, that confirms the usefulness of this method to obtain a single-crystal copper orientation Cu (100). Based on that and the symmetric properties, the graphene flakes can be recognized as highly symmetric and single-crystal. The ND was heavily suppressed (avg. ~5 nucleations/cm^2) by this process and also free of small graphene islands. The graphene flakes and the Cu/copper-oxide layers show a smoother texture, reflecting the higher quality of graphene samples. The graphene flakes have smoother and planar edges, and that was resulted by the high H_2/CH_4 ratio. When considering the transfer method, it has proven to be highly effective in high-quality graphene transfer applications without surface residues, impurities, and wrinkles. That helps to enhance and preserve the electrical characteristics of single-crystal graphene. More importantly, this method makes the graphene transfer much convenient and faster than previous methods. Unlike dry transfer methods involving exfoliated graphene, wet transfer methods are highly random and arduous to perform when transferring graphene flakes onto a specific location such as a gold contact pattern. That led to a waste of resources and time. Even the transferred flakes have low quality so that the devices have weak performance. However, in this method, we have avoided those disadvantages by combining wet and dry transfer methods. We believe that the introduced graphene growth method may be potentially helpful to synthesize better quality single crystalline and monolayer graphene.

6 High crystalline cm-scale CVD graphene flakes grown on copper using a Ni-foam enclosure (Ni/Cu/Ni sandwich)

6.1 Introduction

As discussed in previous chapters, having a minimal nucleation density (ND) is the key to synthesize better-quality single-crystalline graphene layers on large areas. In previous methods, we were able to suppress the ND values lower than ten. However, a further reduction of NDs would be beneficial to improve the graphene quality. Also, a shorter and simpler growth technique would be more helpful in some situations instead of a long-duration growth process. Moreover, we developed a keen interest in high-performance battery and supercapacitor research due to the high demand for better power storage. One of the primary materials used in battery and supercapacitor making is 3-D graphene nickel foams. This fantastic material can be used as a high-efficiency 3-D electrode due to its unique properties such as rapid electron and ion transport, large electroactive surface area, and excellent structural stability. [320-322] These 3-D graphene layers on nickel foam were grown by the CVD method and wanted to start battery/capacitor research by growing 3-D graphene as a start. However, we wanted to combine 3-D graphene growth with our main requirement of growing single-crystalline graphene on Cu to minimize the cost and save time. Hence, we decided to use the gettering carbon diffusion effect of Ni (nickel foam) to capture carbon from copper foils.

Irfan et al. (2017) [323] have used multiple support substrates on the bottom, such as quartz/Ni plate/Ni-foam, to grow graphene using the CVD technique in an Ar environment. However, the only purpose of the Ni-foam-support in their work was to act as a getter substrate that cutting off the bottom carbon supply. However, it does not prevent bi-layer formation due to the potential of direct deposit of active radicals on existing graphene layers and has a

considerable/high nucleation density. Gao et al. (2019) [324] have followed a similar approach to grow graphene as Irfan et al. (2017). In Gao's method, they have used a vertical-type CVD furnace and put a piece of nickel foam above the Cu foil. Both methods are different from the method we introduce in this study except for the gettering carbon diffusion concept. Here, we introduce a new 3-D and 2-D graphene synthesizing method, which reduces the ND to less than one nucleation/cm^2 (which is around 0.57).

6.2 Experimental Methods

6.2.1 Cu foil and Ni-foam surface modification and nickel enclosure preparation (Nickel/Cu/Nickel sandwich)

We have used ~25 µm-thick industrial-grade Cu foils from the same sample as discussed in sections 4.2.1 and 5.2.1. The foils were cut into rectangular-shaped strips with dimensions of 7 cm×1.5 cm. The strip surfaces were cleaned and then oxidized by following the exact steps as mentioned in section 4.2.1. The reasons behind this oxidization step are similar to the explanation given in section 4.2.1. A piece of battery-grade nickel foam was (dimensions: 9 cm×7 cm) oxidized (pre-oxidation) on the hotplate in the open air for 40 minutes at $350 \pm 5\ C^0$. This oxidation was performed due to two reasons: (1) to create an uniform oxide layer (NiO/Ni_2O_3) on growth substrate as much as possible (because some regions of the nickel foam already contain natural nickel oxides, and it was necessary to cover the foam with oxides completely) (2) to help with the self-cleaning process of nickel foam/Cu enclosure. It will be discussed in section 6.3. After the pre-oxidation step, the nickel foam was bent at the middle along the long side (similar to Figure 6.1b) and inserted the Cu strip in between (resembling a Ni/Cu/Ni sandwich). Then the nickel foam enclosure was completed by crimping the free edges and folding them tightly (see Figure 6.1a).

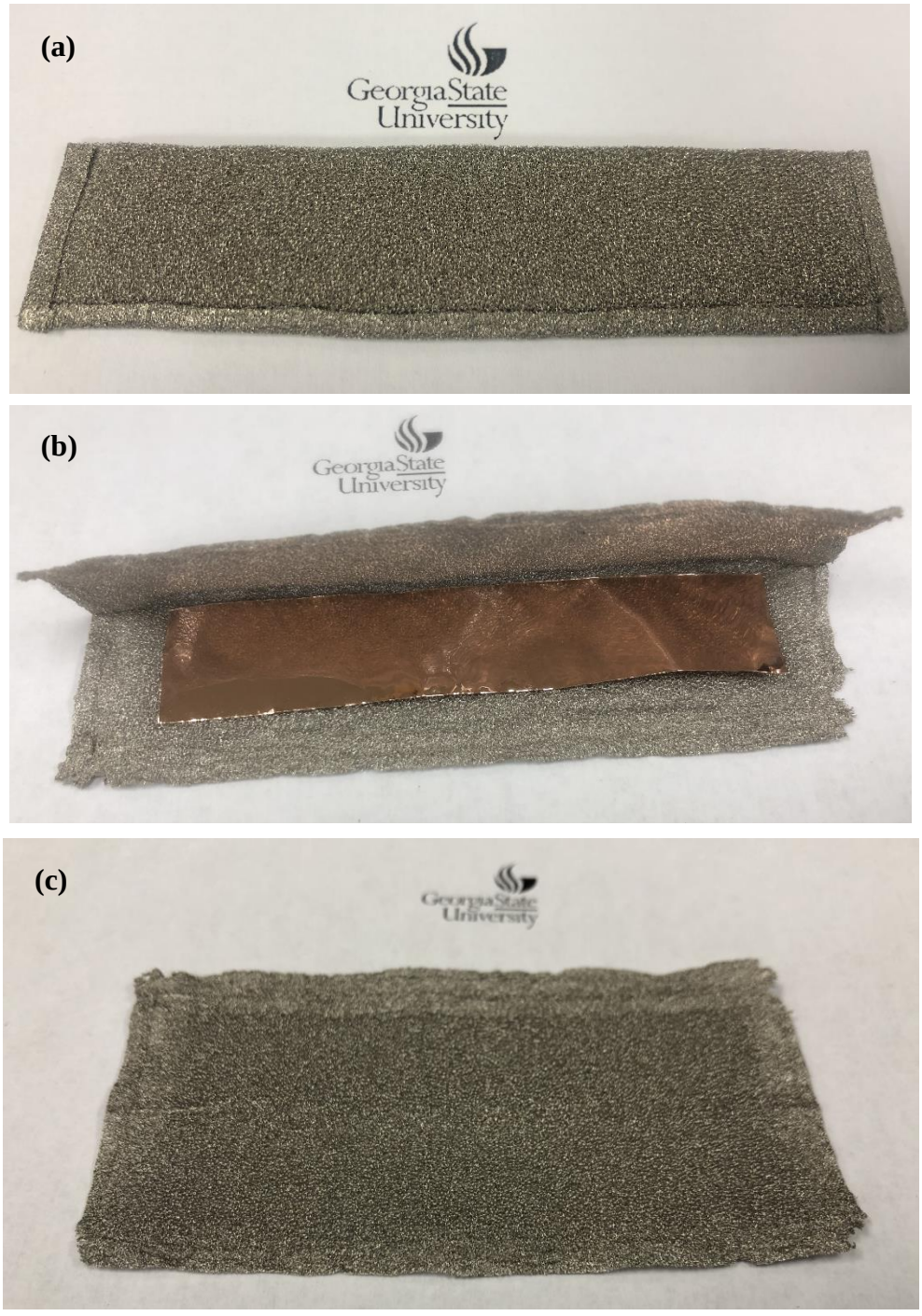

Figure 6.1 The images of Ni-foam and graphene/Cu samples at different stages of the growth process. (a) The oxidized Ni foam enclosure (Ni/Cu/Ni sandwich) just before the growth. (b) The 3D graphene/Ni-foam and the graphene/Cu strip after the growth. (c) The flatten graphene/Ni-foam. This by-product is reusable for another graphene growth cycle. More importantly, this 3D graphene on Ni-foam can be used as a 3-D high-performance electrode.

6.2.2 2-D & 3-D graphene growth on Cu foil strip and Ni-foam enclosure

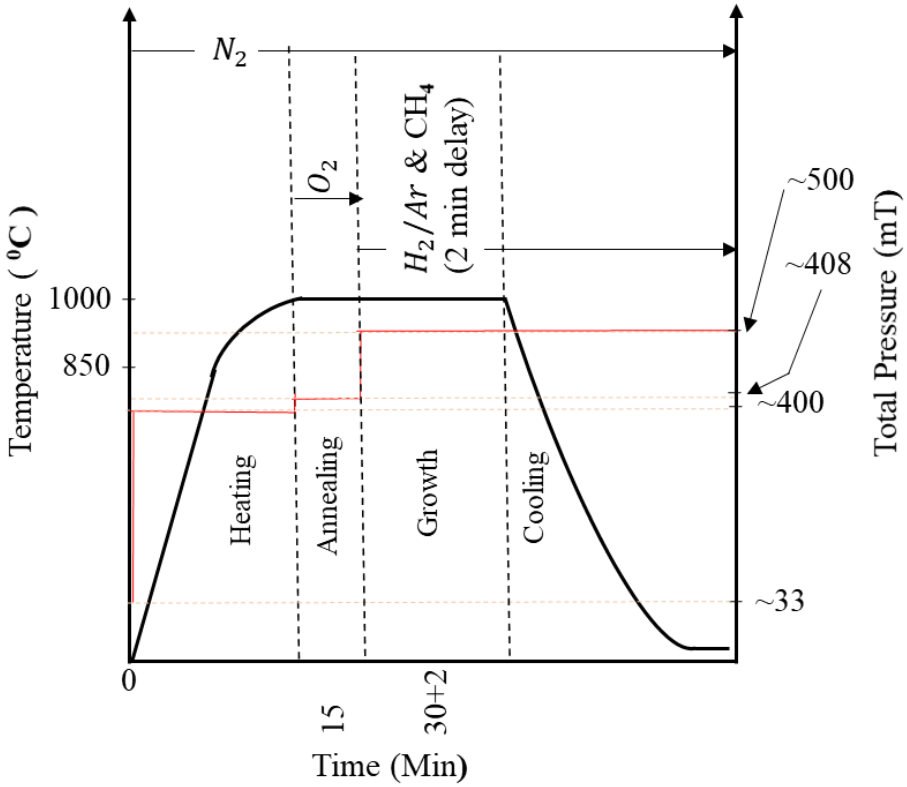

Figure 6.2 A graphical representation of the temperature (left-axis), pressure (right-axis), and the overall growth profile of the LPCVD process. The temperature (black curve) was ramped up to 850^0C from 30^0C and then gradually brought to 1000^0C, as shown on the left axis. The red curve and the right axis represent how the pressure values changed during the entire growth process. The enclosure was oxidized (pre-oxidization) during the LPCVD process by providing a controlled flow of O_2 before the growth cycle for 15 min. At the end of the growth, the temperature set value was immediately adjusted to 30^0C and let the system cool down slowly while keeping the gas flow rates unchanged.

The nickel foam enclosure was loaded into the LPCVD tube furnace (see Figure 6.3), and the primary function of this reactor was discussed in section 5.2.2. In this work, the base pressure value was ~33 mTorr. The sample was carefully placed in the middle section of the heating element (similar to section 5.2.2). It helps to control the near-surface gas flow dynamics so that the deposition becomes more homogenous and controllable. Then the chamber was vacuumed and

brought to a BP value of ~33 mTorr. After that, the system was pressurized to ~400 mTorr by feeding N_2 as shown in Figure 6.2. Once the total pressure (TP) stabilized, the core temperature was ramped up to 850^0C and then gradually increased to the growth temperature of 1000^0C. After reaching the 1000^0C, the enclosure was oxidized by feeding a O_2 flow for 15 minutes. It increased the system pressure by ~8 mTorr (TP = 408 mTorr), and the temperature was constant during the time. At the end of this process, a H_2/Ar flow was introduced while turning off the O_2 flow. After 2 mins, the graphene growth was initiated by feeding a CH_4 flow for 30 min (TP value increased to ~500 mTorr as shown in Figure 6.2). At the end of the growth, the temperature set value was immediately adjusted to the initial temperature (30^0C) and then let the system cool down slowly.

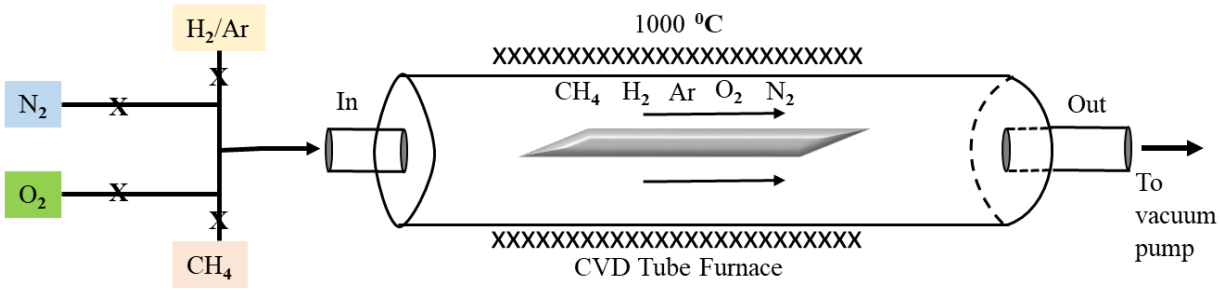

Figure 6.3 A schematic illustration of the LPCVD system. Four gas inlets feed O_2, N_2, $H_2(10\%)/Ar(90\%)$, CH_4 into the CVD tube furnace chamber at different stages of the LPCVD process. The inner diameter of the quartz tube was around 3cm. The Ni-foam enclosure was placed in the middle of the heating element (isothermal zone) to ensure a uniform temperature along the enclosure. Moreover, the enclosure was positioned carefully inside the quartz tube by considering the enclosure geometry and gas-phase dynamics to achieve a uniform reactant concentration and temperature. The maximum growth temperature of the reactor was 1000^0C and achieved a base pressure value of ~33 mTorr.

6.2.3 Characterization

After removing the nickel foam enclosure from the reactor, it was placed on a clean surface, and the edges were unfolded (see Figure 6.1b). The 3-D graphene/nickel foam was made flat using dust-free Si slides (see Figure 6.1c). The graphene/copper foil was loaded inside of a pre-heated oven to oxidize the surface at $\sim 110^0 C$ for 5 min-per-side. It was performed to enhance the optical visualization of individual graphene flakes (see Figure 6.4). After that, graphene regions were visible to the naked eye due to the color contrast between copper oxide and graphene flakes. Then the flat Cu strip was placed on a glass slide, and the images were taken using an iPhone 8+ camera under ambient light conditions. Because the field of view of the OLYMPUS BH2-MJL optical microscope was not enough to capture large graphene layers.

6.3 Results and Discussion

This study was based on two processes: (1) Oxygen-assisted self-cleaning of Cu foil (discussed in chapter 5) and nickel foam (as shown in equations (6.1) to (6.7)). So, the aim was to grow large graphene flakes by limiting the carbon percentage in Cu foil and removing them using the self-cleaning effect and gettering carbon diffusion (hence, suppressing the nucleation density and preventing random nucleation on the Cu surface). Our previous study proved that a very low nucleation density (avg. ~5 nucleations/cm^2) could be achieved by implementing multi-step oxygen passivation of Cu enclosure followed by a complete vacuum step during the growth. Here, we were able to achieve cm-scale graphene flakes with ~1 nucleations/cm^2.

$$O_2(g) + 2(*) \rightarrow 2O_{(ads)} \tag{6.1}$$

$$C_{(ads)} + O_{(ads)} \rightarrow CO_{(ads)} \tag{6.2}$$

$$CO_{ads} + O_{(ads)} \rightarrow CO_2(g) + 2(*) \tag{6.3}$$

$$2CO_{ads} \rightarrow CO_2(g) + C_{(ads)} \quad (6.4)$$

$$CO(g) + (*) \rightarrow CO_{(ads)} \quad (6.5)$$

$$NiO(s) + CH_4(g) \rightarrow Ni(s) + CO_{(ads)} + 2H_2(g) \quad (6.6)$$

$$Ni_2O_3(s) + 3CO_{(ads)} \rightarrow 2Ni(s) + 3CO_2(g) \quad (6.7)$$

The growth mechanism and the concept behind this growth process are as follows. The pre-oxidization in open-air creates CuO/Cu_2O on Cu strip and Ni_2O_3/NiO on nickel foam as shown in equation (6.1). Here (*) stands for a free site on the metal surface, (g) for a gas, (ads) for an adsorbed atom, or a molecule (s) for a solid. [325] Then a Ni-foam/Cu/Ni-foam enclosure was created by putting the Cu strip inside and then tightly crimping and folding the free edges. The Ni-foam has characteristics closer to a Ni mesh. So the tightly crimped and folded edges formed an isolated environment in the interior of the enclosure. Then, during the temperature ramp-up, these oxides were dissociated into Ni(s), Cu(s) and $O_{(ads)}$. Meanwhile, the adsorbed carbon atoms $C_{(ads)}$ in Cu strip start to combine with adsorbed oxygen $O_{(ads)}$. That creates adsorbed carbon monoxide $CO_{(ads)}$ on Cu (see equation (6.2)) and some of the adsorbed carbon monoxide releases as $CO(g)$. Also, $CO_{(ads)}$ combine with $O_{(ads)}$ to form $CO_2(g)$ (see equation (6.3)) and moved away from the Cu foil as shown in Figure 6.5a. That makes the Cu strip free of carbon, as shown in Figure 6.5b, and suppresses the nucleation density by a significant factor, as discussed in chapter 5. Here, the nickel oxides and foam act as a catalyst to oxidize CO and as a gettering substrate for carbon atoms. When $CO(g)$ that released from the Cu surface reaches the Ni-foam, the $CO(g)$ start to adsorb and becomes adsorbed carbon monoxide $CO_{(ads)}$ at the nickel foam surface (see equation (6.5)).

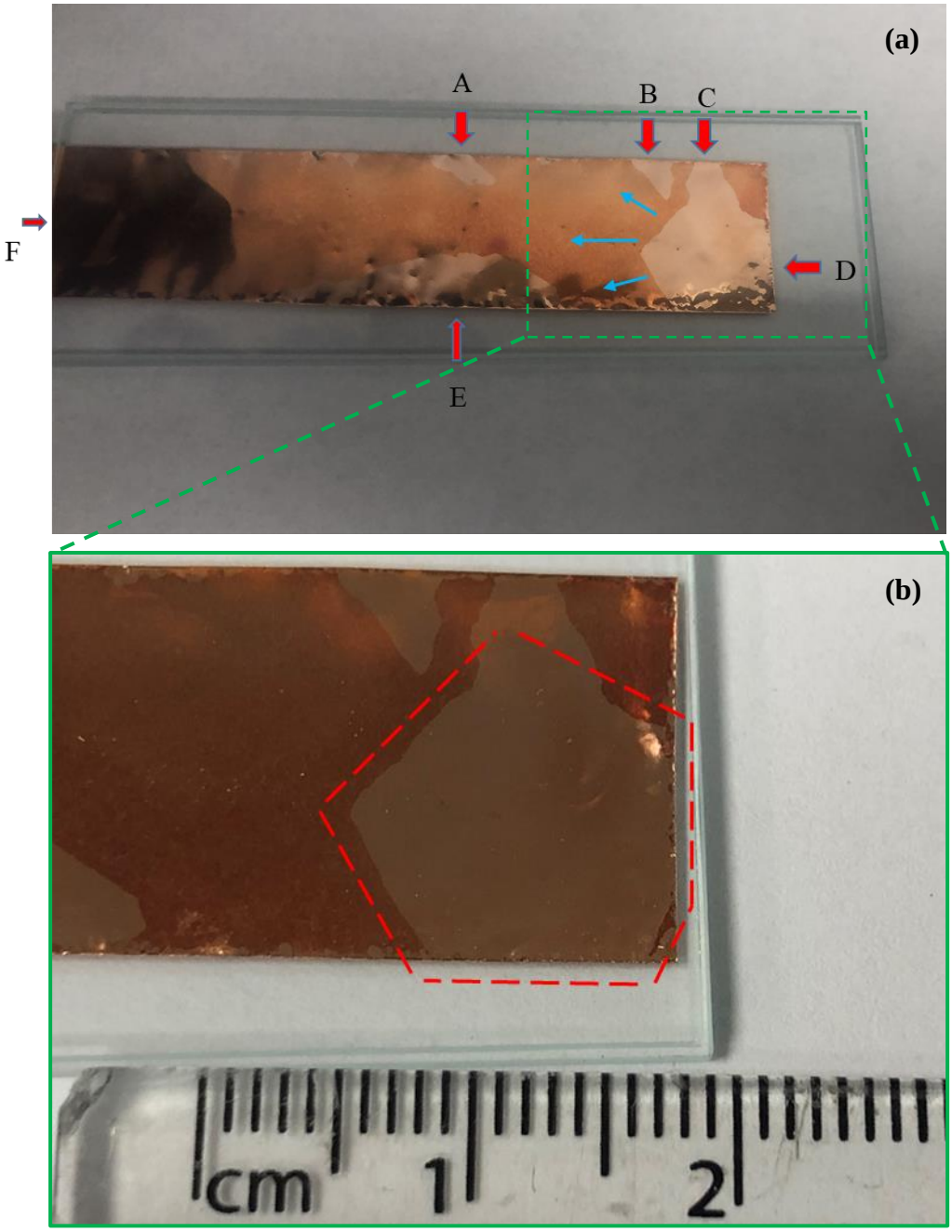

Figure 6.4 The Cu/graphene foil after post-oxidation (optical visual enhancement). (a) The foil contains a cm-scale graphene flake on the right. Red arrows mark the sides which touched the nickel pocket edges. Side D is the main point of interest. The small graphene regions given by B-F can be avoided by preventing those sides from touching the enclosure edges. The blue arrow represents the possible growth directions of the hexagonal graphene flake. (b) The inset of (a) with a measuring scale. The diameter of the flake is larger than 1.3 cm.

Then the in situ oxidation process starts at 1000^0C and the nickel foam start to oxidize by following equation (6.1). That creates more $O_{(ads)}$ and start to combine with adsorbed carbon monoxide $CO_{(ads)}$ (see equation (6.3)) to release more carbon-containing molecules as $CO_2(g)$. Moreover, $Ni_2O_3(s)$ also react with $CO_{(ads)}$ and releases $CO_2(g)$ as shown in equation (6.7). So, at the end of the in situ oxidation, the enclosure carbon percentage becomes low. When the oxygen supply was turned off, the nickel oxides start to dissociate slowly and release adsorbed oxygen by following the same principle as described in the above paragraph.

When the methane gas $CH_4(g)$ was introduced to the system, the $NiO(s)$ start to react with $CH_4(g)$ and produces $CO_{(ads)}$, Ni and $H_2(g)$. That increases the $CO_{(ads)}$ percentage and lowers the nickel oxide percentage. Then the rest of the nickel oxides contribute to the catalysis process. As given in equation (6.4), the adsorbed carbon monoxide $CO_{(ads)}$ start to release from the nickel foam as $CO_2(g)$ (see Figure 6.5a & b) and forms $C_{(ads)}$. These $C_{(ads)}$ can not turn into $CO_{(ads)}$ anymore due to lack of $O_{(ads)}$. Hence, $C_{(ads)}$ start to accumulate in the nickel foam as illustrated in Figure 6.5b. Subsequently, the 3-D graphene growth starts, and the nickel foam becomes carbon saturated. Once the foam becomes carbon saturated, the sharp edge defects on either side A or B (short) attached to the folded nickel foam act as a nucleation site (see Figure 6.5c). Then the carbon saturated shorter Ni-foam edges start to contribute carbon to grow the single flake bigger. More importantly, graphene nucleation is impossible in the middle areas of the Cu strip due to the carbon gettering characteristic of the Ni-foam. Hence the graphene flake, which started at the edge, grows more prominently, as shown in Figure 6.4, and eventually covers a large portion of the Cu strip.

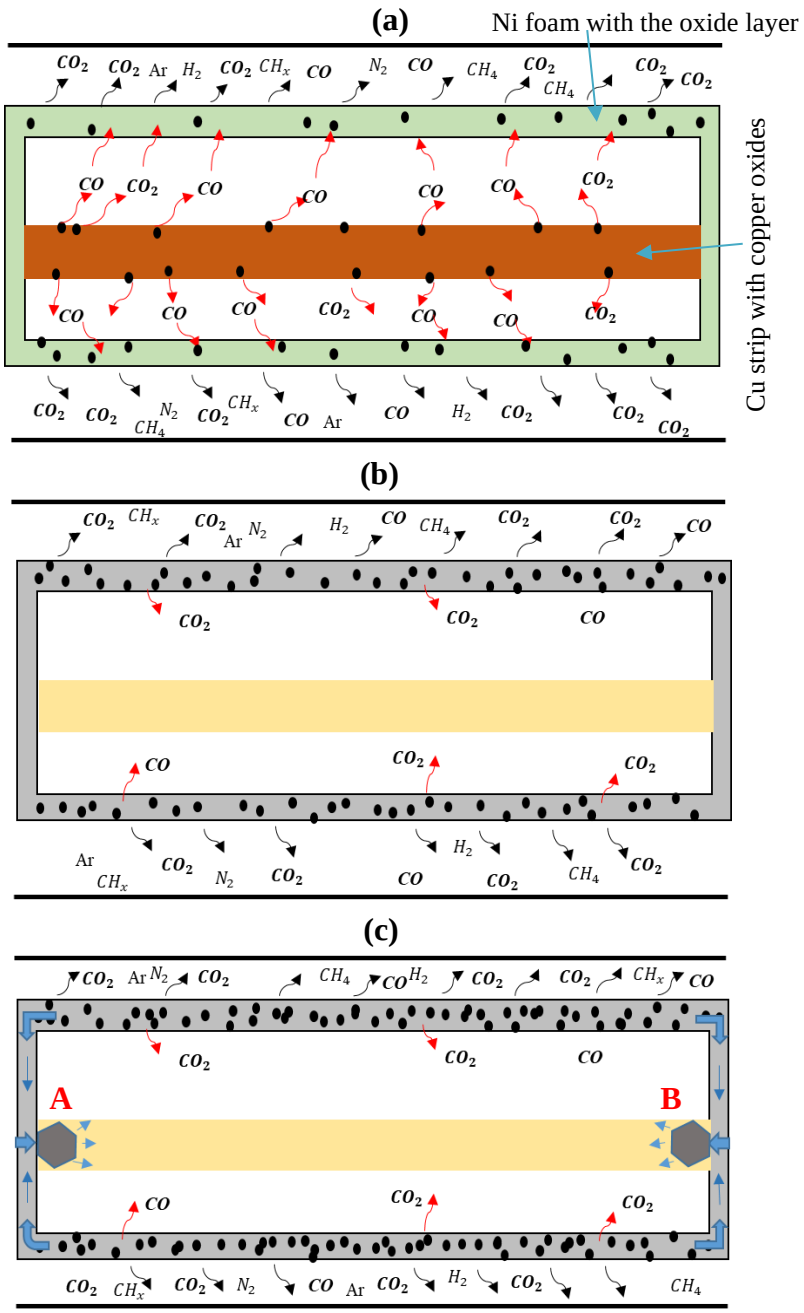

Figure 6.5 A schematic representation of the 3D-graphene growth mechanism on nickel foam and single-crystalline graphene growth on the Cu strip. (a) Phase-I: Self-cleaning process and the initial stage of graphene growth. Here, the green and brown colors are used to represent the nickel and copper oxides, respectively. The carbon atoms are given by black dots. (b) Phase-II: Carbon saturation process. Here the yellow color represents the carbon-free Cu strip. (c) Phase-III: 3-D and 2-D graphene growth process. The thick blue arrows on each side represent the 3-D graphene growth direction on Ni-foam. The thin blue lines represent the saturated carbon flow direction on nickel foam edges and the graphene flake growth direction on the Cu strip.

Also, this graphene growth is different from previous growth mechanisms. Here, graphene growth is only possible by the surface migration of adsorbed carbon atoms from nickel foam enclosure edges. Previously, the exterior of the Cu enclosure had an environment for bi-layer graphene (BLG) growth due to active radicals near the Cu surface. Also, in ideal situations, BLG growth is utterly impossible due to the self-limited growth mechanism. [326] After growing fully on the catalytic surface, there is no space left to decompose CH_4 into carbon or active radicals C_xH_y. So the graphene growth eventually stops and it prevents bi-layer graphene growth. This effect is known as the self-limited growth mechanism, and we have observed a similar effect during the internal graphene growth process in chapter 5. However, the presence of a high number of nucleation sites nullifies this behavior. In the current situation, we have a nucleation density that is lower than 1 nucleation/cm^2 (0.57 to be more precise). Thus, these growth conditions do not lead to BLG growth.

Here we have obtained a hexagonal graphene flake with a diameter larger than 1.3 cm and achieved an ND value as low as ~1 nucleations/cm^2 (0.57). Such a low nucleation density allows this Cu strip to cover with high crystalline single-layer graphene. In this work, the purpose of using nickel foam can be summarized as follows. It acts as an enclosure to create a more controlled environment for graphene growth and an oxygen provider during graphene growth. It also supports the oxygen-assisted copper surface cleaning before the graphene growth and captures carbon before the growth. Moreover, it serves as a controlled carbon feeder during graphene growth and acts as a catalyst during the CVD process.

The flakes A, B, C, and E, which are formed on long edges of the strip (see Figure 6.4a), can be prevented by widening the enclosure's short edges (A and B sides in Figure 6.5c). That will further enhance the quality of the graphene/Cu strip. Such strips are currently in high demand in

areas that make high-performance batteries and supercapacitors additional to their use in high-performance electronics. Moreover, the 3-D graphene Ni-foam (the byproduct) has a high value in nanomaterials markets due to high demand because it uses as a 3-D high-performance electrode for supercapacitors and batteries due to its unique characteristics such as rapid electron and ion transport, large electroactive surface area, and excellent structural stability. [320-322]

6.4 Conclusion

The main focus of this study was to grow large monolayer graphene flakes by suppressing the nucleation density and preventing random nucleation on the Cu surface. Hence, we performed a study to limit the ND by removing carbon atoms from the Cu surface using a getter substrate such as nickel foam. In order to remove the adsorbed carbon atoms from Cu foil and Ni-foam, the oxygen-assisted self-cleaning method was used. In this method, we were able to achieve an ND value (less than one nucleation/cm^2), which is lower than the previous study (avg. ~5 nucleations/cm^2). More importantly, we were able to grow a graphene flake with a diameter of over 1.3 cm. No nucleations were found in the middle of the Cu strip. We suggest that the flakes grown on long edges can prevent by increasing the enclosure width so that the long edges will not touch the enclosure edges. We conclude that the graphene multilayers are impossible to grow in this method due to the growth conditions. The flake that starts to grow from a shorter edge can grow along the strip by preserving the single crystal properties. This method will be advantageous to grow single-crystalline graphene/Cu stripes that can be used in high-performance electronics or as a battery material. The other advantage is the usefulness of 3D-graphene Nickel foam, which is the byproduct of this method. Currently, 3D-graphene Nickel foams have a high demand due to

their use as a 3-D high-performance electrode for supercapacitors and batteries. Thus, we conclude that the method discussed in this work can produce high-quality graphene and is cost-effective.

REFERENCES

1. Withanage, S., et al., *The role of surface morphology on nucleation density limitation during the CVD growth of graphene and the factors influencing graphene wrinkle formation.* MRS Advances, 2019. **4**(61-62): p. 3337-3345.
2. Withanage, S., et al. *The effect of multi-step Cu surface oxidization on growth of single crystal graphene by low pressure chemical vapor deposition*. in *APS March Meeting Abstracts*. 2019.
3. Withanage, S., et al., *Hybrid Transfer of 2D materials: An approach towards a wrinkle and contaminations free transfer of 2D materials grown on metallic substrates for van der Waals heterostructures and large scale industrial applications.* Bulletin of the American Physical Society, 2020. **65**.
4. Tamura, P.H. *A spice of strangeness*. 2020; Available from: https://www2.kek.jp/proffice/archives/feature/2010/images/StrangeHadronTheory2.jpg.
5. J. Haubold, H. and A. Mathai, *Universe, structure of the.* digital Encyclopedia of Applied Physics, 2003.
6. Kitchin, C., *Images of the universe: Edited by Carole Stott. Pp. 237. Cambridge University Press. 1991. Hardback ISBN 0 521 39178 4; paperback ISBN 0 521 42419 4*. 1992, Elsevier Current Trends.
7. universe-review. *Graphene*. 2019 05/07/2020]; Available from: https://universe-review.ca/I13-16-CarbonGen.png.
8. Smith, C.S., *The discovery of carbon in steel.* Technology and culture, 1964. **5**(2): p. 149-175.
9. Lavoisier, A., *Elements of chemistry (R. Kerr, Trans.).* Edinburgh: W. Creech, 1789.
10. Bundy, F., et al., *Man-made diamonds.* nature, 1955. **176**(4471): p. 51-55.
11. Peierls, R. *Quelques propriétés typiques des corps solides*. in *Annales de l'institut Henri Poincaré*. 1935.
12. Landau, L.D., E.M. Lifshitz, and L. Pitaevskii, *Statistical physics (course of theoretical physics)*. 3 ed. Vol. 5. 1980.
13. Mermin, N.D., *Crystalline order in two dimensions.* Physical Review, 1968. **176**(1): p. 250.
14. Landau, L., *Zur Theorie der phasenumwandlungen II.* Phys. Z. Sowjetunion, 1937. **11**(545): p. 26-35.
15. O'Hare, A., F. Kusmartsev, and K. Kugel, *A Stable "Flat "Form of Two-Dimensional Crystals: Could Graphene, Silicene, Germanene Be Minigap Semiconductors?* Nano letters, 2012. **12**(2): p. 1045-1052.
16. Radushkevich, L. and V.á. Lukyanovich, *O strukture ugleroda, obrazujucegosja pri termiceskom razlozenii okisi ugleroda na zeleznom kontakte.* Zurn Fisic Chim, 1952. **26**(1): p. 88-95.
17. Kroto, H.W., et al., *C60: Buckminsterfullerene.* Nature, 1985. **318**(6042): p. 162-163.
18. Zhou, Z., et al., *Fullerene nanomaterials potentiate hair growth.* Nanomedicine: Nanotechnology, Biology and Medicine, 2009. **5**(2): p. 202-207.
19. Mashino, T., et al., *Antibacterial and antiproliferative activity of cationic fullerene derivatives.* Bioorganic & medicinal chemistry letters, 2003. **13**(24): p. 4395-4397.
20. Mousavi, S.Z., S. Nafisi, and H.I. Maibach, *Fullerene nanoparticle in dermatological and cosmetic applications.* Nanomedicine: Nanotechnology, Biology and Medicine, 2017. **13**(3): p. 1071-1087.

21. Cooper, D., J. Gerratt, and M. Raimondi, *Modern valence bond theory.* Adv. Chem. Phys, 1987. **69**: p. 319-397.
22. Yau, D. *sp, sp2, sp3 hybrid orbitals*. CHEM 121 2015 Spring 2015; Available from: http://faculty.ccbcmd.edu/~cyau/121%2009%20Fig21.jpg.
23. Silberberg, M., *Chemistry: The Molecular Nature of Matter and Change With Advanced Topics*. 2018: McGraw-Hill.
24. Chung, D., *Review graphite.* Journal of materials science, 2002. **37**(8): p. 1475-1489.
25. Harlow, G.E., *The nature of diamonds*. 1998: Cambridge University Press.
26. Costello, K. *HYBRIDIZATON: Flexibility at its best*. 2011 05/08/2020]; Available from: http://www.chemistryland.com/CHM151S/09-CovalentBonds/Covalent.html.
27. Rode, A.V., et al., *Unconventional magnetism in all-carbon nanofoam.* Physical Review B, 2004. **70**(5): p. 054407.
28. Rode, A.V., et al., *Strong paramagnetism and possible ferromagnetism in pure carbon nanofoam produced by laser ablation.* Journal of magnetism and magnetic materials, 2005. **290**: p. 298-301.
29. Mattis, D.C., *Theory of ferromagnetism in carbon foam.* Physical Review B, 2005. **71**(14): p. 144424.
30. Saucedo-Jimenez, D., I. Medina-Sanchez, and C. Couder Castañeda, *Carbon Nanofoam by Pulsed Electric Arc Discharges.* Advances in Materials Science and Engineering, 2018. **2018**.
31. Novoselov, K.S., et al., *Electric field effect in atomically thin carbon films.* science, 2004. **306**(5696): p. 666-669.
32. Wallace, P.R., *The Band Theory of Graphite.* Physical Review, 1947. **71**(9): p. 622-634.
33. Boehm, H.-P., et al., *Das adsorptionsverhalten sehr dünner kohlenstoff-folien.* Zeitschrift für anorganische und allgemeine Chemie, 1962. **316**(3-4): p. 119-127.
34. Ohashi, Y., et al., *Size Effect inthe In-plane Electrical Resistivity of Very Thin Graphite Crystals.* Tanso, 1997. **1997**(180): p. 235-238.
35. Motlagh, S.A.O., et al., *Ultrafast optical currents in gapped graphene.* Journal of Physics: Condensed Matter, 2019. **32**(6): p. 065305.
36. Akbar, F., et al., *Graphene synthesis, characterization and its applications in nanophotonics, nanoelectronics, and nanosensing.* Journal of Materials Science: Materials in Electronics, 2015. **26**(7): p. 4347-4379.
37. de Abajo, F.J.G., *Graphene nanophotonics.* Science, 2013. **339**(6122): p. 917-918.
38. Wijewardena, U.K., et al., *Effects of Long-Time Current Annealing to the Hysteresis in CVD Graphene on SiO 2.* MRS Advances, 2019. **4**(61-62): p. 3319-3326.
39. Raza, H., *Graphene nanoelectronics: Metrology, synthesis, properties and applications*. 2012: Springer Science & Business Media.
40. Ho, K.-I., et al., *Fluorinated graphene as high performance dielectric materials and the applications for graphene nanoelectronics.* Scientific reports, 2014. **4**: p. 5893.
41. El-Kady, M.F., et al., *Laser scribing of high-performance and flexible graphene-based electrochemical capacitors.* Science, 2012. **335**(6074): p. 1326-1330.
42. Lin, Y.-M., et al., *100-GHz transistors from wafer-scale epitaxial graphene.* Science, 2010. **327**(5966): p. 662-662.
43. Schedin, F., et al., *Detection of individual gas molecules adsorbed on graphene.* Nature materials, 2007. **6**(9): p. 652-655.

44. Kim, K.S., et al., *Large-scale pattern growth of graphene films for stretchable transparent electrodes.* nature, 2009. **457**(7230): p. 706-710.
45. Avouris, P., et al. *Graphene-based fast electronics and optoelectronics*. in *68th Device Research Conference*. 2010. IEEE.
46. Bonaccorso, F., et al., *Graphene photonics and optoelectronics.* Nature photonics, 2010. **4**(9): p. 611.
47. Aghigh, A., et al., *Recent advances in utilization of graphene for filtration and desalination of water: a review.* Desalination, 2015. **365**: p. 389-397.
48. Mishra, A.K. and S. Ramaprabhu, *Functionalized graphene sheets for arsenic removal and desalination of sea water.* Desalination, 2011. **282**: p. 39-45.
49. Cohen-Tanugi, D. and J.C. Grossman, *Water desalination across nanoporous graphene.* Nano letters, 2012. **12**(7): p. 3602-3608.
50. Surwade, S.P., et al., *Water desalination using nanoporous single-layer graphene.* Nature nanotechnology, 2015. **10**(5): p. 459-464.
51. Mueller, T., F. Xia, and P. Avouris, *Graphene photodetectors for high-speed optical communications.* Nature photonics, 2010. **4**(5): p. 297.
52. Nair, R.R., et al., *Fine structure constant defines visual transparency of graphene.* Science, 2008. **320**(5881): p. 1308-1308.
53. Sheehy, D.E. and J. Schmalian, *Optical transparency of graphene as determined by the fine-structure constant.* Physical Review B, 2009. **80**(19): p. 193411.
54. Bolotin, K.I., et al., *Ultrahigh electron mobility in suspended graphene.* Solid state communications, 2008. **146**(9-10): p. 351-355.
55. Stoller, M.D., et al., *Graphene-based ultracapacitors.* Nano letters, 2008. **8**(10): p. 3498-3502.
56. Lee, C., et al., *Measurement of the elastic properties and intrinsic strength of monolayer graphene.* science, 2008. **321**(5887): p. 385-388.
57. Jiang, Z., et al., *Quantum Hall states near the charge-neutral Dirac point in graphene.* Physical review letters, 2007. **99**(10): p. 106802.
58. Novoselov, K.S., et al., *Unconventional quantum Hall effect and Berry's phase of 2π in bilayer graphene.* Nature physics, 2006. **2**(3): p. 177-180.
59. Du, X., et al., *Fractional quantum Hall effect and insulating phase of Dirac electrons in graphene.* Nature, 2009. **462**(7270): p. 192-195.
60. Papageorgiou, D.G., I.A. Kinloch, and R.J. Young, *Mechanical properties of graphene and graphene-based nanocomposites.* Progress in Materials Science, 2017. **90**: p. 75-127.
61. Moore, G.E., *Cramming more components onto integrated circuits*. 1965, McGraw-Hill New York, NY, USA:.
62. Jayasena, B. and S. Subbiah, *A novel mechanical cleavage method for synthesizing few-layer graphenes.* Nanoscale research letters, 2011. **6**(1): p. 95.
63. Times, G., *Boehm's 1961 isolation of graphene.* Acessed June, 2016.
64. Eigler, S., et al., *Wet chemical synthesis of graphene.* Advanced Materials, 2013. **25**(26): p. 3583-3587.
65. Paton, K.R., et al., *Scalable production of large quantities of defect-free few-layer graphene by shear exfoliation in liquids.* Nature materials, 2014. **13**(6): p. 624.
66. Hernandez, Y., et al., *High-yield production of graphene by liquid-phase exfoliation of graphite.* Nature nanotechnology, 2008. **3**(9): p. 563.

67. Nuvoli, D., et al., *High concentration few-layer graphene sheets obtained by liquid phase exfoliation of graphite in ionic liquid.* Journal of Materials Chemistry, 2011. **21**(10): p. 3428-3431.
68. Woltornist, S.J., et al., *Conductive thin films of pristine graphene by solvent interface trapping.* ACS nano, 2013. **7**(8): p. 7062-7066.
69. Hofmann, M., et al., *Controlling the properties of graphene produced by electrochemical exfoliation.* Nanotechnology, 2015. **26**(33): p. 335607.
70. Tang, L., et al., *Bottom-up synthesis of large-scale graphene oxide nanosheets.* Journal of Materials Chemistry, 2012. **22**(12): p. 5676-5683.
71. Coraux, J., et al., *Structural coherency of graphene on Ir (111).* Nano letters, 2008. **8**(2): p. 565-570.
72. Ramón, M.E., et al., *CMOS-compatible synthesis of large-area, high-mobility graphene by chemical vapor deposition of acetylene on cobalt thin films.* Acs Nano, 2011. **5**(9): p. 7198-7204.
73. Reina, A., et al., *Layer area, few-layer graphene films on arbitrary substrates by chemical vapor deposition.* Nano letters, 2009. **9**(8): p. 3087-3087.
74. Li, X., et al., *Large-area synthesis of high-quality and uniform graphene films on copper foils.* science, 2009. **324**(5932): p. 1312-1314.
75. Sutter, P.W., J.-I. Flege, and E.A. Sutter, *Epitaxial graphene on ruthenium.* Nature materials, 2008. **7**(5): p. 406-411.
76. Coraux, J., et al., *Growth of graphene on Ir (111).* New Journal of Physics, 2009. **11**(2): p. 023006.
77. Varykhalov, A. and O. Rader, *Graphene grown on Co (0001) films and islands: Electronic structure and its precise magnetization dependence.* Physical Review B, 2009. **80**(3): p. 035437.
78. Emtsev, K., et al., *Interaction, growth, and ordering of epitaxial graphene on SiC {0001} surfaces: A comparative photoelectron spectroscopy study.* Physical Review B, 2008. **77**(15): p. 155303.
79. Kim, S., et al., *Origin of anomalous electronic structures of epitaxial graphene on silicon carbide.* Physical review letters, 2008. **100**(17): p. 176802.
80. Juang, Z.-Y., et al., *Synthesis of graphene on silicon carbide substrates at low temperature.* Carbon, 2009. **47**(8): p. 2026-2031.
81. Emtsev, K.V., et al., *Towards wafer-size graphene layers by atmospheric pressure graphitization of silicon carbide.* Nature materials, 2009. **8**(3): p. 203-207.
82. Choucair, M., P. Thordarson, and J.A. Stride, *Gram-scale production of graphene based on solvothermal synthesis and sonication.* Nature nanotechnology, 2009. **4**(1): p. 30.
83. Kosynkin, D.V., et al., *Longitudinal unzipping of carbon nanotubes to form graphene nanoribbons.* Nature, 2009. **458**(7240): p. 872-876.
84. Jiao, L., et al., *Narrow graphene nanoribbons from carbon nanotubes.* Nature, 2009. **458**(7240): p. 877-880.
85. Zheng, Q., et al., *Transparent conductive films consisting of ultralarge graphene sheets produced by Langmuir–Blodgett assembly.* Acs Nano, 2011. **5**(7): p. 6039-6051.
86. Cote, L.J., F. Kim, and J. Huang, *Langmuir− Blodgett assembly of graphite oxide single layers.* Journal of the American Chemical Society, 2009. **131**(3): p. 1043-1049.
87. Li, X., et al., *Highly conducting graphene sheets and Langmuir–Blodgett films.* Nature nanotechnology, 2008. **3**(9): p. 538-542.

88. Chakrabarti, A., et al., *Conversion of carbon dioxide to few-layer graphene.* Journal of Materials Chemistry, 2011. **21**(26): p. 9491-9493.
89. Yan, Z., et al., *Rebar graphene.* ACS nano, 2014. **8**(5): p. 5061-5068.
90. Kim, D.Y., et al., *Self-healing reduced graphene oxide films by supersonic kinetic spraying.* Advanced Functional Materials, 2014. **24**(31): p. 4986-4995.
91. Kovtyukhova, N.I., et al., *Non-oxidative intercalation and exfoliation of graphite by Brønsted acids.* Nature chemistry, 2014. **6**(11): p. 957.
92. Hwang, J., et al., *Ultrapure multilayer graphene in bromine-intercalated graphite.* Physical Review B, 2011. **84**(4): p. 041410.
93. Hong, Y., Z. Wang, and X. Jin, *Sulfuric acid intercalated graphite oxide for graphene preparation.* Scientific reports, 2013. **3**: p. 3439.
94. Lin, J., et al., *Laser-induced porous graphene films from commercial polymers.* Nature communications, 2014. **5**(1): p. 1-8.
95. Chiu, P.L., et al., *Microwave-and nitronium ion-enabled rapid and direct production of highly conductive low-oxygen graphene.* Journal of the American Chemical Society, 2012. **134**(13): p. 5850-5856.
96. Patel, M.A., et al., *Direct production of graphene nanosheets for near infrared photoacoustic imaging.* ACS nano, 2013. **7**(9): p. 8147-8157.
97. Savaram, K., et al., *Synergy of oxygen and a piranha solution for eco-friendly production of highly conductive graphene dispersions.* Green Chemistry, 2015. **17**(2): p. 869-881.
98. Patel, M., et al., *Microwave Enabled One-Pot, One-Step Fabrication and Nitrogen Doping of Holey Graphene Oxide for Catalytic Applications.* Small, 2015. **11**(27): p. 3358-3368.
99. Garaj, S., W. Hubbard, and J.A. Golovchenko, *Graphene synthesis by ion implantation.* Applied physics letters, 2010. **97**(18): p. 183103.
100. Kim, J., G. Lee, and J. Kim, *Wafer-scale synthesis of multi-layer graphene by high-temperature carbon ion implantation.* Applied Physics Letters, 2015. **107**(3): p. 033104.
101. Lee, H.C., et al., *Facet-Mediated Growth of High-Quality Monolayer Graphene on Arbitrarily Rough Copper Surfaces.* Advanced Materials, 2016. **28**(10): p. 2010-2017.
102. Zhao, L., et al., *Influence of copper crystal surface on the CVD growth of large area monolayer graphene.* Solid State Communications, 2011. **151**(7): p. 509-513.
103. Deokar, G., et al., *Towards high quality CVD graphene growth and transfer.* Carbon, 2015. **89**: p. 82-92.
104. Kobayashi, T., et al., *Production of a 100-m-long high-quality graphene transparent conductive film by roll-to-roll chemical vapor deposition and transfer process.* Applied Physics Letters, 2013. **102**(2): p. 023112.
105. Polsen, E.S., et al., *High-speed roll-to-roll manufacturing of graphene using a concentric tube CVD reactor.* Scientific reports, 2015. **5**: p. 10257.
106. Vlassiouk, I., et al., *Large scale atmospheric pressure chemical vapor deposition of graphene.* Carbon, 2013. **54**: p. 58-67.
107. Zhong, G., et al., *Growth of continuous graphene by open roll-to-roll chemical vapor deposition.* Applied Physics Letters, 2016. **109**(19): p. 193103.
108. Faggio, G., et al., *High-temperature growth of graphene films on copper foils by ethanol chemical vapor deposition.* The Journal of Physical Chemistry C, 2013. **117**(41): p. 21569-21576.
109. Zhou, H., et al., *Chemical vapour deposition growth of large single crystals of monolayer and bilayer graphene.* Nature communications, 2013. **4**(1): p. 1-8.

110. Hofmann, S., P. Braeuninger-Weimer, and R.S. Weatherup, *CVD-enabled graphene manufacture and technology.* The journal of physical chemistry letters, 2015. **6**(14): p. 2714-2721.
111. Banszerus, L., et al., *Ultrahigh-mobility graphene devices from chemical vapor deposition on reusable copper.* Science advances, 2015. **1**(6): p. e1500222.
112. Boyd, D., et al., *Single-step deposition of high-mobility graphene at reduced temperatures.* Nature communications, 2015. **6**(1): p. 1-8.
113. Schmitz, M., et al., *High mobility dry-transferred CVD bilayer graphene.* Applied Physics Letters, 2017. **110**(26): p. 263110.
114. Li, X., et al., *Graphene films with large domain size by a two-step chemical vapor deposition process.* Nano letters, 2010. **10**(11): p. 4328-4334.
115. Roth, S., et al., *Chemical vapor deposition and characterization of aligned and incommensurate graphene/hexagonal boron nitride heterostack on Cu (111).* Nano letters, 2013. **13**(6): p. 2668-2675.
116. Geng, D., et al., *Self-Aligned Single-Crystal Graphene Grains.* Advanced Functional Materials, 2014. **24**(12): p. 1664-1670.
117. Xu, X., et al., *Ultrafast growth of single-crystal graphene assisted by a continuous oxygen supply.* Nature nanotechnology, 2016. **11**(11): p. 930.
118. Liu, W., et al., *Synthesis of high-quality monolayer and bilayer graphene on copper using chemical vapor deposition.* Carbon, 2011. **49**(13): p. 4122-4130.
119. Hao, Y., et al., *The role of surface oxygen in the growth of large single-crystal graphene on copper.* Science, 2013. **342**(6159): p. 720-723.
120. Vlassiouk, I., et al., *Graphene nucleation density on copper: fundamental role of background pressure.* The Journal of Physical Chemistry C, 2013. **117**(37): p. 18919-18926.
121. Ajayan, P.M. and B.I. Yakobson, *Pushing the boundaries.* Nature Materials, 2011. **10**(6): p. 415-417.
122. Huang, P.Y., et al., *Grains and grain boundaries in single-layer graphene atomic patchwork quilts.* Nature, 2011. **469**(7330): p. 389-392.
123. Yu, Q., et al., *Control and characterization of individual grains and grain boundaries in graphene grown by chemical vapour deposition.* Nature Materials, 2011. **10**(6): p. 443-449.
124. Allain, P.E. and J.-N. Fuchs, *Klein tunneling in graphene: optics with massless electrons.* The European Physical Journal B, 2011. **83**(3): p. 301.
125. Stander, N., B. Huard, and D. Goldhaber-Gordon, *Evidence for Klein tunneling in graphene p− n junctions.* Physical review letters, 2009. **102**(2): p. 026807.
126. Beenakker, C., *Colloquium: Andreev reflection and Klein tunneling in graphene.* Reviews of Modern Physics, 2008. **80**(4): p. 1337.
127. Katsnelson, M.I., K.S. Novoselov, and A.K. Geim, *Chiral tunnelling and the Klein paradox in graphene.* Nature Physics, 2006. **2**(9): p. 620-625.
128. Dresselhaus, G. and S. Riichiro, *Physical properties of carbon nanotubes*. 1998: World scientific.
129. Gogotsi, Y. and V. Presser, *Carbon nanomaterials*. 2013: CRC press.
130. Constantin, C. *Thermoelectric Properties of PEDOTPSS/Semiconductor substrates*. Harvesting Heat through Seebeck Spin Tunneling Effect 2012 05/2012 [cited 2020 05/12];

Available from: https://commons.lib.jmu.edu/cgi/viewcontent.cgi?article=1007&context=photon.
131. Manini, N., *Introduction to the Physics of Matter: Basic atomic, molecular, and solid-state physics*. 2015: Springer.
132. McCann, E. and M. Koshino, *The electronic properties of bilayer graphene.* Reports on Progress in Physics, 2013. **76**(5): p. 056503.
133. Ishioka, S., *Proceedings of the 9th International Symposium on Foundations of Quantum Mechanics in the Light of New Technology: IS? M--Tokyo'08*. 2009: World Scientific.
134. Zhang, Q., *Carbon nanotubes and their applications*. 2012: CRC Press.
135. Blakemore, J.S., *Semiconductor statistics*. 2002: Courier Corporation.
136. Jensen, F., *Introduction to computational chemistry*. 2017: John wiley & sons.
137. Stauber, T., *Handbook of Graphene, Volume 2: Physics, Chemistry, and Biology*. 2019: John Wiley & Sons.
138. Neto, A.C., et al., *The electronic properties of graphene*. Reviews of modern physics, 2009. **81**(1): p. 109.
139. Ihn, T., *Semiconductor Nanostructures: Quantum states and electronic transport*. 2010: Oxford University Press.
140. Koshino, M. and T. Ando, *Orbital diamagnetism in multilayer graphenes: Systematic study with the effective mass approximation.* Physical Review B, 2007. **76**(8): p. 085425.
141. Enoki, T., S. Fujii, and K. Takai, *Zigzag and armchair edges in graphene.* Carbon, 2012. **50**(9): p. 3141-3145.
142. Yang, S.A. *Dirac and Weyl materials: fundamental aspects and some spintronics applications*. in *Spin*. 2016. World Scientific.
143. Cayssol, J., *Introduction to Dirac materials and topological insulators.* Comptes Rendus Physique, 2013. **14**(9-10): p. 760-778.
144. Flouris, K., et al., *Confining massless Dirac particles in two-dimensional curved space.* Physical Review B, 2018. **98**(15): p. 155419.
145. Lan, Z., et al., *Dirac-Weyl fermions with arbitrary spin in two-dimensional optical superlattices.* Physical Review B, 2011. **84**(16): p. 165115.
146. Williams, J.R., *Electron Optics with Graphene p–n Junctions*, in *2D Materials: Properties and Devices*, P. Avouris, T. Low, and T.F. Heinz, Editors. 2017, Cambridge University Press: Cambridge. p. 141-158.
147. Ang, Y.S., Z. Ma, and C. Zhang, *Chiral-like tunneling of electrons in two-dimensional semiconductors with Rashba spin-orbit coupling.* Scientific reports, 2014. **4**(1): p. 1-7.
148. Shlimak, I., et al., *Irradiation-induced metal-insulator transition in monolayer graphene*. 2019.
149. Dargys, A., *Spin and pseudospin in monolayer graphene: Part I. Representation by geometric algebra and simple cases.* Physica Scripta, 2015. **90**(2): p. 025807.
150. Bernal, J.D., *The structure of graphite.* Proceedings of the Royal Society of London. Series A, Containing Papers of a Mathematical and Physical Character, 1924. **106**(740): p. 749-773.
151. Chadi, D., *Si (100) surfaces: Atomic and electronic structures.* Journal of Vacuum Science and Technology, 1979. **16**(5): p. 1290-1296.
152. Mak, K.F., et al., *The evolution of electronic structure in few-layer graphene revealed by optical spectroscopy.* Proceedings of the National Academy of Sciences, 2010. **107**(34): p. 14999-15004.

153. Oostinga, J.B., et al., *Gate-induced insulating state in bilayer graphene devices.* Nature materials, 2008. **7**(2): p. 151-157.
154. Yu, W.J. and X. Duan, *Tunable transport gap in narrow bilayer graphene nanoribbons.* Scientific reports, 2013. **3**: p. 1248.
155. Castro, E.V., et al., *Biased bilayer graphene: semiconductor with a gap tunable by the electric field effect.* Physical review letters, 2007. **99**(21): p. 216802.
156. Kuzmenko, A., et al., *Determination of the gate-tunable band gap and tight-binding parameters in bilayer graphene using infrared spectroscopy.* Physical Review B, 2009. **80**(16): p. 165406.
157. Bhuyan, M.S.A., et al., *Synthesis of graphene.* International Nano Letters, 2016. **6**(2): p. 65-83.
158. Patil, U., et al., *Nanostructured pseudocapacitive materials decorated 3D graphene foam electrodes for next generation supercapacitors.* Nanoscale, 2015. **7**(16): p. 6999-7021.
159. Xu, Y., et al., *Liquid-Phase exfoliation of graphene: An overview on exfoliation media, techniques, and challenges.* Nanomaterials, 2018. **8**(11): p. 942.
160. Lotya, M., et al., *Liquid phase production of graphene by exfoliation of graphite in surfactant/water solutions.* Journal of the American Chemical Society, 2009. **131**(10): p. 3611-3620.
161. Narayan, R. and S.O. Kim, *Surfactant mediated liquid phase exfoliation of graphene.* Nano Convergence, 2015. **2**(1): p. 20.
162. Cui, X., et al., *Liquid-phase exfoliation, functionalization and applications of graphene.* Nanoscale, 2011. **3**(5): p. 2118-2126.
163. Boehm, H.P., R. Setton, and E. Stumpp, *Nomenclature and terminology of graphite intercalation compounds (IUPAC Recommendations 1994).* Pure and Applied Chemistry, 1994. **66**(9): p. 1893-1901.
164. Chacón-Torres, J.C., L. Wirtz, and T. Pichler, *Raman spectroscopy of graphite intercalation compounds: Charge transfer, strain, and electron–phonon coupling in graphene layers.* physica status solidi (b), 2014. **251**(12): p. 2337-2355.
165. Weller, T.E., et al., *Superconductivity in the intercalated graphite compounds C 6 Yb and C 6 Ca.* Nature Physics, 2005. **1**(1): p. 39-41.
166. Dimiev, A.M., et al., *Direct real-time monitoring of stage transitions in graphite intercalation compounds.* ACS nano, 2013. **7**(3): p. 2773-2780.
167. Zhao, W., et al., *Intercalation of few-layer graphite flakes with FeCl3: Raman determination of Fermi level, layer by layer decoupling, and stability.* Journal of the American Chemical Society, 2011. **133**(15): p. 5941-5946.
168. Doll, G., M. Yang, and P. Eklund, *Comparative optical study of the two-dimensional donor-type intercalation compounds graphite-KH x and their binary counterparts C 8 K and C 24 K.* Physical Review B, 1987. **35**(18): p. 9790.
169. Yang, M. and P. Eklund, *Optical dielectric function of high-stage potassium graphite intercalation compounds: Experiment and theory.* Physical Review B, 1988. **38**(5): p. 3505.
170. Howard, C., M. Dean, and F. Withers, *Phonons in potassium-doped graphene: The effects of electron-phonon interactions, dimensionality, and adatom ordering.* Physical Review B, 2011. **84**(24): p. 241404.
171. Emery, N., et al., *Superconductivity of bulk CaC 6.* Physical review letters, 2005. **95**(8): p. 087003.

172. Chakraborty, S., et al., *Functionalization of potassium graphite.* Angewandte Chemie International Edition, 2007. **46**(24): p. 4486-4488.
173. Emery, N., et al., *Synthesis and superconducting properties of CaC6.* Science and technology of advanced materials, 2009. **9**(4): p. 044102.
174. Yoon, G., et al., *Factors affecting the exfoliation of graphite intercalation compounds for graphene synthesis.* Chemistry of Materials, 2015. **27**(6): p. 2067-2073.
175. Li, Y., et al., *Intercalation chemistry of graphite: alkali metal ions and beyond.* Chemical Society Reviews, 2019. **48**(17): p. 4655-4687.
176. Guo, Y., et al., *Intercalation polymerization approach for preparing graphene/polymer composites.* Polymers, 2018. **10**(1): p. 61.
177. Bonaccorso, F., et al., *Production and processing of graphene and 2d crystals.* Materials today, 2012. **15**(12): p. 564-589.
178. Dresselhaus, M., *Intercalation in layered materials.* MRS Bulletin, 1987. **12**(3): p. 24-28.
179. Phillips, C., et al., *The effect of graphite and carbon black ratios on conductive ink performance.* Journal of Materials Science, 2017. **52**(16): p. 9520-9530.
180. Enoki, T., M. Suzuki, and M. Endo, *Graphite intercalation compounds and applications*. 2003: Oxford University Press.
181. Kaschak, D.M., et al., *Graphite intercalation and exfoliation process*. 2006, Google Patents.
182. Khan, U., et al., *Solvent-exfoliated graphene at extremely high concentration.* Langmuir, 2011. **27**(15): p. 9077-9082.
183. Wang, J., et al., *Solvent exfoliated graphene for reinforcement of PMMA composites prepared by in situ polymerization.* Materials Chemistry and Physics, 2012. **136**(1): p. 43-50.
184. Ciesielski, A. and P. Samorì, *Graphene via sonication assisted liquid-phase exfoliation.* Chemical Society Reviews, 2014. **43**(1): p. 381-398.
185. Coleman, J.N., *Liquid exfoliation of defect-free graphene.* Accounts of chemical research, 2013. **46**(1): p. 14-22.
186. Feicht, P., et al., *Facile and scalable one-step production of organically modified graphene oxide by a two-phase extraction.* Carbon, 2014. **80**: p. 229-234.
187. Kumar, H.V., S.J. Woltornist, and D.H. Adamson, *Fractionation and characterization of graphene oxide by oxidation extent through emulsion stabilization.* Carbon, 2016. **98**: p. 491-495.
188. Feicht, P., et al., *Systematic evaluation of different types of graphene oxide in respect to variations in their in-plane modulus.* Carbon, 2017. **114**: p. 700-705.
189. Lerf, A., et al., *Structure of graphite oxide revisited.* The Journal of Physical Chemistry B, 1998. **102**(23): p. 4477-4482.
190. Szabó, T., et al., *Evolution of surface functional groups in a series of progressively oxidized graphite oxides.* Chemistry of materials, 2006. **18**(11): p. 2740-2749.
191. Hummers Jr, W.S. and R.E. Offeman, *Preparation of graphitic oxide.* Journal of the american chemical society, 1958. **80**(6): p. 1339-1339.
192. Bai, H., C. Li, and G. Shi, *Functional composite materials based on chemically converted graphene.* Advanced Materials, 2011. **23**(9): p. 1089-1115.
193. Interface, B.-E., *Material Matters™*. 2019.
194. Ferrari, A.C., et al., *Science and technology roadmap for graphene, related two-dimensional crystals, and hybrid systems.* Nanoscale, 2015. **7**(11): p. 4598-4810.

195. Sreeprasad, T. and V. Berry, *How do the electrical properties of graphene change with its functionalization?* Small, 2013. **9**(3): p. 341-350.
196. Marquez, C., et al., *Electrical characterization and conductivity optimization of laser reduced graphene oxide on insulator using point-contact methods.* Rsc Advances, 2016. **6**(52): p. 46231-46237.
197. Pei, S. and H.-M. Cheng, *The reduction of graphene oxide.* Carbon, 2012. **50**(9): p. 3210-3228.
198. Moon, I.K., et al., *Reduced graphene oxide by chemical graphitization.* Nature communications, 2010. **1**(1): p. 1-6.
199. Park, S., et al., *Hydrazine-reduction of graphite-and graphene oxide.* Carbon, 2011. **49**(9): p. 3019-3023.
200. Robinson, J.T., et al., *Reduced graphene oxide molecular sensors.* Nano letters, 2008. **8**(10): p. 3137-3140.
201. Chua, C.K. and M. Pumera, *Chemical reduction of graphene oxide: a synthetic chemistry viewpoint.* Chemical Society Reviews, 2014. **43**(1): p. 291-312.
202. Park, S., et al., *Aqueous suspension and characterization of chemically modified graphene sheets.* Chemistry of materials, 2008. **20**(21): p. 6592-6594.
203. Liu, J., J. Tang, and J.J. Gooding, *Strategies for chemical modification of graphene and applications of chemically modified graphene.* Journal of Materials Chemistry, 2012. **22**(25): p. 12435-12452.
204. Xu, Y. and G. Shi, *Assembly of chemically modified graphene: methods and applications.* Journal of Materials Chemistry, 2011. **21**(10): p. 3311-3323.
205. Yang, M.H., et al., *Development of a glucose biosensor using advanced electrode modified by nanohybrid composing chemically modified graphene and ionic liquid.* Electroanalysis: An International Journal Devoted to Fundamental and Practical Aspects of Electroanalysis, 2010. **22**(11): p. 1223-1228.
206. Zhang, Y., et al., *Fabrication and electric-field-dependent transport measurements of mesoscopic graphite devices.* Applied Physics Letters, 2005. **86**(7): p. 073104.
207. Geim, A.K. and K.S. Novoselov, *The rise of graphene.* Nature Materials, 2007. **6**(3): p. 183-191.
208. Lu, X., et al., *Tailoring graphite with the goal of achieving single sheets.* Nanotechnology, 1999. **10**(3): p. 269.
209. Lu, X., et al., *Patterning of highly oriented pyrolytic graphite by oxygen plasma etching.* Applied Physics Letters, 1999. **75**(2): p. 193-195.
210. Chang, K. *Thin Carbon Is In: Graphene Steals Nanotubes' Allure*. 2017 April 10, 2007; Available from: https://www.nytimes.com/2007/04/10/science/10grap.html.
211. Ruoff, R.S. *Micromechanical Exfoliation and Graphene: 1999 papers and brief discussion of them*. 2007 Sat, 2007-03-03 09:38 [cited 2020 05/28]; Available from: https://imechanica.org/node/963.
212. Yi, M. and Z. Shen, *A review on mechanical exfoliation for the scalable production of graphene.* Journal of Materials Chemistry A, 2015. **3**(22): p. 11700-11715.
213. Chelnokov, V., A. Syrkin, and V. Dmitriev, *Overview of SiC power electronics.* Diamond and related materials, 1997. **6**(10): p. 1480-1484.
214. Hornberger, J., et al. *Silicon-carbide (SiC) semiconductor power electronics for extreme high-temperature environments*. in *2004 IEEE Aerospace Conference Proceedings (IEEE Cat. No. 04TH8720)*. 2004. IEEE.

215. Wondrak, W., et al., *SiC devices for advanced power and high-temperature applications.* IEEE Transactions on Industrial Electronics, 2001. **48**(2): p. 307-308.
216. Tolbert, L.M., et al., *Impact of SiC power electronic devices for hybrid electric vehicles.* SAE Transactions, 2002: p. 765-771.
217. Picraux, S.T., *Epitaxy*, in *Epitaxy CRYSTALLOGRAPHY*. 1998, ENCYCLOPÆDIA BRITANNICA.
218. Norimatsu, W. and M. Kusunoki, *Epitaxial graphene on SiC {0001}: advances and perspectives.* Physical Chemistry Chemical Physics, 2014. **16**(8): p. 3501-3511.
219. Forbeaux, I., J.-M. Themlin, and J.-M. Debever, *Heteroepitaxial graphite on 6 H− SiC (0001): Interface formation through conduction-band electronic structure.* Physical Review B, 1998. **58**(24): p. 16396.
220. Berger, C., et al., *Ultrathin epitaxial graphite: 2D electron gas properties and a route toward graphene-based nanoelectronics.* The Journal of Physical Chemistry B, 2004. **108**(52): p. 19912-19916.
221. Choi, W. and J.-w. Lee, *Graphene: synthesis and applications*. 2016: CRC press.
222. Warner, J.H., et al., *Graphene: fundamentals and emergent applications*. 2012: Newnes.
223. Speck, F., et al., *Growth and Intercalation of Graphene on Silicon Carbide Studied by Low-Energy Electron Microscopy.* Annalen der Physik, 2017. **529**(11): p. 1700046.
224. Yazdi, G.R., T. Iakimov, and R. Yakimova, *Epitaxial graphene on SiC: a review of growth and characterization.* Crystals, 2016. **6**(5): p. 53.
225. Wang, C., K. Vinodgopal, and G.-P. Dai, *Large-Area Synthesis and Growth Mechanism of Graphene by Chemical Vapor Deposition*, in *Chemical Vapor Deposition for Nanotechnology*. 2018, IntechOpen. p. 18.
226. Ouerghi, A., et al., *Large-area and high-quality epitaxial graphene on off-axis SiC wafers.* Acs Nano, 2012. **6**(7): p. 6075-6082.
227. Miettinen, A., M.S. Nevius, and E.H. Conrad, *The growth and structure of epitaxial graphene nanoribbons*, in *Graphene Nanoribbons*. 2019, IOP Publishing. p. 1-1-1-29.
228. Giannazzo, F., et al., *Electronic properties of epitaxial graphene residing on SiC facets probed by conductive atomic force microscopy.* Applied surface science, 2014. **291**: p. 53-57.
229. Giannazzo, F., et al., *High resolution study of structural and electronic properties of epitaxial graphene grown on off-axis 4H–SiC (0001).* Journal of crystal growth, 2014. **393**: p. 150-155.
230. De Heer, W.A., et al., *Epitaxial graphene electronic structure and transport.* Journal of Physics D: Applied Physics, 2010. **43**(37): p. 374007.
231. Bouhafs, C., et al., *Decoupling and ordering of multilayer graphene on C-face 3C-SiC (111).* Applied Physics Letters, 2016. **109**(20): p. 203102.
232. Tiberj, A., et al., *Micro-Raman and micro-transmission imaging of epitaxial graphene grown on the Si and C faces of 6H-SiC.* Nanoscale research letters, 2011. **6**(1): p. 478.
233. Srivastava, N., et al., *Comparison of graphene formation on C-face and Si-face SiC {0001} surfaces.* Physical Review B, 2010. **82**(23): p. 235406.
234. Srivastava, N., et al., *Graphene formed on SiC under various environments: comparison of Si-face and C-face.* Journal of Physics D: Applied Physics, 2012. **45**(15): p. 154001.
235. Jernigan, G.G., et al., *Comparison of epitaxial graphene on Si-face and C-face 4H SiC formed by ultrahigh vacuum and RF furnace production.* Nano letters, 2009. **9**(7): p. 2605-2609.

236. Johansson, L.I., et al., *Is the registry between adjacent graphene layers grown on C-face SiC different compared to that on Si-face SiC.* Crystals, 2013. **3**(1): p. 1-13.
237. Johansson, L.I. and C. Virojanadara, *Properties of epitaxial graphene grown on C-face SiC compared to Si-face.* Journal of Materials Research, 2014. **29**(3): p. 426-438.
238. Robinson, J., et al., *Nucleation of epitaxial graphene on SiC (0001).* Acs Nano, 2010. **4**(1): p. 153-158.
239. Macedo, L.J., et al., *Bioelectronics and interfaces using monolayer graphene.* ChemElectroChem, 2019. **6**(1): p. 31-59.
240. Wu, Y., et al., *State-of-the-art graphene high-frequency electronics.* Nano letters, 2012. **12**(6): p. 3062-3067.
241. Beshkova, M., L. Hultman, and R. Yakimova, *Device applications of epitaxial graphene on silicon carbide.* Vacuum, 2016. **128**: p. 186-197.
242. Lin, Y.-M., et al., *Wafer-scale graphene integrated circuit.* Science, 2011. **332**(6035): p. 1294-1297.
243. Hanna, T., et al., *2.5 GHz integrated graphene RF power amplifier on SiC substrate.* Solid-State Electronics, 2017. **127**: p. 26-31.
244. Kedzierski, J., et al., *Epitaxial graphene transistors on SiC substrates.* IEEE Transactions on Electron Devices, 2008. **55**(8): p. 2078-2085.
245. Wu, Y., et al. *Record high RF performance for epitaxial graphene transistors*. in *2011 International Electron Devices Meeting*. 2011. IEEE.
246. Lara-Avila, S., et al., *SiC graphene suitable for quantum hall resistance metrology.* arXiv preprint arXiv:0909.1193, 2009.
247. Schumann, T., et al., *Anisotropic quantum Hall effect in epitaxial graphene on stepped SiC surfaces.* Physical Review B, 2012. **85**(23): p. 235402.
248. Tzalenchuk, A., et al., *Towards a quantum resistance standard based on epitaxial graphene.* Nature nanotechnology, 2010. **5**(3): p. 186.
249. Shen, T., et al., *Observation of quantum-Hall effect in gated epitaxial graphene grown on SiC (0001).* Applied Physics Letters, 2009. **95**(17): p. 172105.
250. Jobst, J., et al., *Quantum oscillations and quantum Hall effect in epitaxial graphene.* Physical Review B, 2010. **81**(19): p. 195434.
251. Wu, X., et al., *Half integer quantum Hall effect in high mobility single layer epitaxial graphene.* Applied Physics Letters, 2009. **95**(22): p. 223108.
252. Miao, C., et al., *Chemical vapor deposition of graphene.* Physics and applications of graphene-experiments, 2011: p. 2011.
253. Mikhailov, S., *Physics and Applications of Graphene: Experiments*. 2011: BoD–Books on Demand.
254. Pierson, H.O., *Handbook of chemical vapor deposition: principles, technology and applications*. 1999: William Andrew.
255. Juang, Z.-Y., et al., *Graphene synthesis by chemical vapor deposition and transfer by a roll-to-roll process.* Carbon, 2010. **48**(11): p. 3169-3174.
256. Mattevi, C., H. Kim, and M. Chhowalla, *A review of chemical vapour deposition of graphene on copper.* Journal of Materials Chemistry, 2011. **21**(10): p. 3324-3334.
257. Wang, H., et al., *Primary Nucleation-Dominated Chemical Vapor Deposition Growth for Uniform Graphene Monolayers on Dielectric Substrate.* Journal of the American Chemical Society, 2019. **141**(28): p. 11004-11008.

258. Yu, Q., et al., *Graphene segregated on Ni surfaces and transferred to insulators.* Applied Physics Letters, 2008. **93**(11): p. 113103.
259. Zhang, Y., et al., *Comparison of graphene growth on single-crystalline and polycrystalline Ni by chemical vapor deposition.* The Journal of Physical Chemistry Letters, 2010. **1**(20): p. 3101-3107.
260. Fang, W., et al., *A review of large-area bilayer graphene synthesis by chemical vapor deposition.* Nanoscale, 2015. **7**(48): p. 20335-20351.
261. Elnashaie, S.S., F. Danafar, and H.H. Rafsanjani, *Learning Synergism in Nanotechnology and Chemical Engineering by Case Study*, in *Nanotechnology for Chemical Engineers*. 2015, Springer. p. 179-272.
262. Li, X., et al., *Evolution of graphene growth on Ni and Cu by carbon isotope labeling.* Nano letters, 2009. **9**(12): p. 4268-4272.
263. Clark, J.C. *Bond Enthalpies*. Molecules 2020 May 18, 2020 06/08/2020]; Available from: https://chem.libretexts.org/Bookshelves/Physical_and_Theoretical_Chemistry_Textbook_Maps/Supplemental_Modules_(Physical_and_Theoretical_Chemistry)/Thermodynamics/Energies_and_Potentials/Enthalpy/Bond_Enthalpies#:~:text=In%20the%20methane%20case%2C%20you,kJ%20per%20mole%20of%20bonds.
264. Avouris, P. and C. Dimitrakopoulos, *Graphene: synthesis and applications.* Materials today, 2012. **15**(3): p. 86-97.
265. Bipasha, A. and S.S. Hossain, *Md. Sajibul Alam Bhuyan, Md. Nizam Uddin, Md. Maksudul Islam, Ferdaushi.*
266. Somekh, M., E. Shawat, and G.D. Nessim, *Fully reproducible, low-temperature synthesis of high-quality, few-layer graphene on nickel via preheating of gas precursors using atmospheric pressure chemical vapor deposition.* Journal of Materials Chemistry A, 2014. **2**(46): p. 19750-19758.
267. Azam, M.A., et al., *critical considerations of high quality graphene synthesized by plasma-enhanced chemical vapor deposition for electronic and energy storage devices.* ECS Journal of Solid State Science and Technology, 2017. **6**(6): p. M3035-M3048.
268. Kalita, G. and M. Tanemura, *Fundamentals of Chemical Vapor Deposited Graphene and Emerging Applications.* Graphene Materials-Advanced Applications, 2017.
269. Kim, H., et al., *Modeling of the self-limited growth in catalytic chemical vapor deposition of graphene.* New Journal of Physics, 2013. **15**(5): p. 053012.
270. Argyle, M.D. and C.H. Bartholomew, *Heterogeneous catalyst deactivation and regeneration: a review.* Catalysts, 2015. **5**(1): p. 145-269.
271. Dossot, M., *Handbook of Carbon Nano Materials Volume 7, Synthetic Developments of Graphene and Nanotubes. Edited by Francis D'Souza and Karl M. Kadish. World Scientific Press, 2016. Pp. 240. Price GBP 195.00, USD 295.00 (for the Volume 7 and 8 set). ISBN 9789814689175.* Journal of Applied Crystallography, 2016. **49**(2): p. 718-719.
272. Rashid, S.A., R.N.I.R. Othman, and M.Z. Hussein, *Synthesis, Technology and Applications of Carbon Nanomaterials*. 2018: Elsevier.
273. Hernández, S.C., et al., *Controlling the local chemical reactivity of graphene through spatial functionalization.* Carbon, 2013. **60**: p. 84-93.
274. Chen, S., et al., *Oxidation resistance of graphene-coated Cu and Cu/Ni alloy.* ACS nano, 2011. **5**(2): p. 1321-1327.
275. De Heer, W.A., et al., *Epitaxial graphene.* Solid State Communications, 2007. **143**(1-2): p. 92-100.

276. Mani, R.G., *Method for determining the residual electron-and hole-densities about the neutrality point over the gate-controlled n↔ p transition in graphene.* Applied Physics Letters, 2016. **108**(3): p. 033507.
277. Wijewardena, U.K., S.E. Brown, and X.-Q. Wang, *Epoxy-carbonyl conformation of graphene oxides.* The Journal of Physical Chemistry C, 2016. **120**(39): p. 22739-22743.
278. Mani, R.G., et al., *Observation of resistively detected hole spin resonance and zero-field pseudo-spin splitting in epitaxial graphene.* Nature communications, 2012. **3**(1): p. 1-6.
279. Ghimire, R., et al., *Topological nanospaser.* Nanophotonics, 2020. **9**(4): p. 865-874.
280. Motlagh, S.A.O., et al., *Topological resonance and single-optical-cycle valley polarization in gapped graphene.* Physical Review B, 2019. **100**(11): p. 115431.
281. Hass, J., et al., *Highly ordered graphene for two dimensional electronics.* Applied Physics Letters, 2006. **89**(14): p. 143106.
282. Bae, S., et al., *Roll-to-roll production of 30-inch graphene films for transparent electrodes.* Nature nanotechnology, 2010. **5**(8): p. 574.
283. Kraus, J., M. Böbel, and S. Günther, *Suppressing graphene nucleation during CVD on polycrystalline Cu by controlling the carbon content of the support foils.* Carbon, 2016. **96**: p. 153-165.
284. Li, Q., et al., *Controllable seeding of single crystal graphene islands from graphene oxide flakes.* Carbon, 2014. **79**: p. 406-412.
285. Chuang, M.-C. and W.-Y. Woon, *Nucleation and growth dynamics of graphene on oxygen exposed copper substrate.* Carbon, 2016. **103**: p. 384-390.
286. Li, X., et al., *Large-area graphene single crystals grown by low-pressure chemical vapor deposition of methane on copper.* Journal of the American Chemical Society, 2011. **133**(9): p. 2816-2819.
287. Gan, L. and Z. Luo, *Turning off hydrogen to realize seeded growth of subcentimeter single-crystal graphene grains on copper.* Acs Nano, 2013. **7**(10): p. 9480-9488.
288. Gulotty, R., et al., *Effect of hydrogen flow during cooling phase to achieve uniform and repeatable growth of bilayer graphene on copper foils over large area.* Carbon, 2014. **77**: p. 341-350.
289. Hao, Y., et al., *Oxygen-activated growth and bandgap tunability of large single-crystal bilayer graphene.* Nature nanotechnology, 2016. **11**(5): p. 426.
290. Li, J., et al., *Facile growth of centimeter-sized single-crystal graphene on copper foil at atmospheric pressure.* Journal of Materials Chemistry C, 2015. **3**(15): p. 3530-3535.
291. Suzuki, S., et al., *Low density growth of graphene by air introduction in atmospheric pressure chemical vapor deposition.* e-Journal of Surface Science and Nanotechnology, 2015. **13**: p. 404-409.
292. Fang, W., et al., *Asymmetric growth of bilayer graphene on copper enclosures using low-pressure chemical vapor deposition.* ACS nano, 2014. **8**(6): p. 6491-6499.
293. Chen, X., et al., *Chemical vapor deposition growth of 5 mm hexagonal single-crystal graphene from ethanol.* Carbon, 2015. **94**: p. 810-815.
294. Huet, B. and J.-P. Raskin, *Role of Cu foil in-situ annealing in controlling the size and thickness of CVD graphene domains.* Carbon, 2018. **129**: p. 270-280.
295. Braeuninger-Weimer, P., et al., *Understanding and controlling Cu-catalyzed graphene nucleation: the role of impurities, roughness, and oxygen scavenging.* Chemistry of Materials, 2016. **28**(24): p. 8905-8915.

296. Choudhary, S., et al., *Oxidation mechanism of thin Cu films: A gateway towards the formation of single oxide phase.* AIP Advances, 2018. **8**(5): p. 055114.
297. Lee, S.-K., H.-C. Hsu, and W.-H. Tuan, *Oxidation Behavior of Copper at a Temperature below 300 C and the Methodology for Passivation.* Materials Research, 2016. **19**(1): p. 51-56.
298. Miseikis, V., et al., *Rapid CVD growth of millimetre-sized single crystal graphene using a cold-wall reactor.* 2D Materials, 2015. **2**(1): p. 014006.
299. Sarajlic, O.I. and R.G. Mani, *Mesoscale scanning electron and tunneling microscopy study of the surface morphology of thermally annealed copper foils for graphene growth.* Chemistry of Materials, 2013. **25**(9): p. 1643-1648.
300. Eres, G., et al., *Cooperative island growth of large-area single-crystal graphene on copper using chemical vapor deposition.* ACS nano, 2014. **8**(6): p. 5657-5669.
301. Bellitto, V., *Atomic force microscopy: imaging, measuring and manipulating surfaces at the atomic scale*. 2012: BoD–Books on Demand.
302. Yi, D., et al., *What drives metal-surface step bunching in graphene chemical vapor deposition?* Physical review letters, 2018. **120**(24): p. 246101.
303. Koenig, S.P., et al., *Ultrastrong adhesion of graphene membranes.* Nature nanotechnology, 2011. **6**(9): p. 543.
304. Meca, E., et al., *Epitaxial graphene growth and shape dynamics on copper: phase-field modeling and experiments.* Nano letters, 2013. **13**(11): p. 5692-5697.
305. Losurdo, M., et al., *Graphene CVD growth on copper and nickel: role of hydrogen in kinetics and structure.* Physical Chemistry Chemical Physics, 2011. **13**(46): p. 20836-20843.
306. Magnuson, C.W., et al., *Copper oxide as a" self-cleaning" substrate for graphene growth.* Journal of Materials Research, 2014. **29**(3): p. 403.
307. Li, J., et al., *Oxygen-diffusion-induced phase boundary migration in copper oxide thin films.* Physical Review B, 1989. **39**(16): p. 12367.
308. Li, J. and J. Mayer, *Oxidation and reduction of copper oxide thin films.* Materials chemistry and physics, 1992. **32**(1): p. 1-24.
309. Goswami, A. and Y. Trehan, *The thermal decomposition of cupric oxide in vacuo.* Proceedings of the Physical Society. Section B, 1957. **70**(10): p. 1005.
310. Pirkle, A., et al., *The effect of chemical residues on the physical and electrical properties of chemical vapor deposited graphene transferred to SiO2.* Applied Physics Letters, 2011. **99**(12): p. 122108.
311. Adam, S., et al., *A self-consistent theory for graphene transport.* Proceedings of the National Academy of Sciences, 2007. **104**(47): p. 18392-18397.
312. Lee, Y.G., et al., *Fast transient charging at the graphene/SiO 2 interface causing hysteretic device characteristics.* Applied Physics Letters, 2011. **98**(18): p. 183508.
313. Lafkioti, M., et al., *Graphene on a hydrophobic substrate: doping reduction and hysteresis suppression under ambient conditions.* Nano letters, 2010. **10**(4): p. 1149-1153.
314. Chaitoglou, S. and E. Bertran, *Effect of pressure and hydrogen flow in nucleation density and morphology of graphene bidimensional crystals.* Materials Research Express, 2016. **3**(7): p. 075603.
315. Moreno-Bárcenas, A., et al., *Graphene synthesis using a CVD reactor and a discontinuous feed of gas precursor at atmospheric pressure.* Journal of Nanomaterials, 2018. **2018**.

316. Xue, X., et al., *Gas-flow-driven aligned growth of graphene on liquid copper.* Chemistry of Materials, 2019. **31**(4): p. 1231-1236.
317. Komissarov, I.V., et al., *Nitrogen-doped twisted graphene grown on copper by atmospheric pressure CVD from a decane precursor.* Beilstein journal of nanotechnology, 2017. **8**(1): p. 145-158.
318. Luo, B., et al., *Sputtering an exterior metal coating on copper enclosure for large-scale growth of single-crystalline graphene.* 2D Materials, 2017. **4**(4): p. 045017.
319. Jacobberger, R.M. and M.S. Arnold, *Graphene growth dynamics on epitaxial copper thin films.* Chemistry of Materials, 2013. **25**(6): p. 871-877.
320. Lee, K., et al., *3D graphene–Ni foam as an advanced electrode for high-performance nonaqueous redox flow batteries.* ACS applied materials & interfaces, 2017. **9**(27): p. 22502-22508.
321. Wang, Y., et al., *Electrodeposited nickel cobalt sulfide nanosheet arrays on 3D-graphene/Ni foam for high-performance supercapacitors.* RSC advances, 2015. **5**(121): p. 100106-100113.
322. Jinlong, L., et al., *Fabrication of 3D graphene foam for a highly conducting electrode.* Materials Letters, 2017. **196**: p. 369-372.
323. Abidi, I.H., et al., *Regulating Top-Surface Multilayer/Single-Crystal Graphene Growth by "Gettering" Carbon Diffusion at Backside of the Copper Foil.* Advanced Functional Materials, 2017. **27**(23): p. 1700121.
324. Gao, X., et al., *Growth of graphene with large single-crystal domains by Ni foam-assisted structure and its high-gain field-effect transistors.* Nanoscale Advances, 2019. **1**(3): p. 1130-1135.
325. Dey, S. and N. Mehta, *Oxidation of carbon monoxide over various nickel oxide catalysts in different conditions: A review.* Chemical Engineering Journal Advances, 2020: p. 100008.
326. Reckinger, N., et al., *Restoring self-limited growth of single-layer graphene on copper foil via backside coating.* Nanoscale, 2019. **11**(11): p. 5094-5101.